U.S. Department
of Transportation
Federal Railroad
Administration

THERMAL BOUNDARY CONDITIONS FROM ENGULFING FIRES

Office of Research and
Development
Washington D.C. 20590

DOT/FRA/ORD-94/23

September 1994
Final Report

Technical Report Documentation Page

1. Report No. FRA/ORD-94/23

2. Government Accession No.

3. Recipient's Catalog No.

4. Title and Subtitle
Thermal Boundary Conditions From Engulfing Fires

5. Report Date
3 September 94

6. Performing Organization Code
Sandia National Laboratories

7. Author(s) Koski, Brown, Gianoulakis, Nicolette,
Bainbridge, Keltner, Nakos, Sobolik

8. Performing Organization Report No.
SAND89-2432
TTC-0945

9. Performing Organization Name and Address
Sandia National Laboratories
P.O. Box 5800
Albuquerque, NM 87185

10. Work Unit No. (TRAIS)

11. Contract or Grant No.
DTFR-88-X-00028

12. Sponsoring Agency Name and Address
U.S. Department of Transportation
Federal Railroad Admin. Off. of Research & Devel.
400 Seventh Street SW
Washington, DC 20590

13. Type of Report and Period Covered
Test Report
(9/8/88)

14. Sponsoring Agency Code
RDV-32

15. Supplementary Notes

16. Abstract

Determination of a realistic fire boundary condition provides cask designers with a tool to predict accurately the response of a cask in a fire. In one approach to determining this thermal input, data were analyzed from previous engulfing fire experiments on casklike objects. In another approach an analytical model was developed to investigate the influence of test objects on the fire. As has long been suspected, the cask and the fire environment strongly interact. The response of a cask in a fire is highly dependent on the physical and thermal characteristics of the cask; in fact, a very massive cask can alter the early fire environment. Therefore, it appears unlikely that a simple fire boundary condition can be derived that will accurately describe the response of a cask in a fire.

17. Key Words
heat flux, fire, thermal boundary
conditions, large pool fire

18. Distribution Statement
Document available through the National
Technical Information Service
5285 Port Royal Road
Springfield, VA 22161

19. Security Classif. (of this report)
Unclassified

20. Security Classif. (of this page)
Unclassified

21. No. of Pages
116

22. Price

Form DOT F 1700.7 (8-72)

Reproduction of completed page authorized

METRIC CONVERSION FACTORS

Approximate Conversions to Metric Measures

Symbol	When You Know	Multiply by	To Find	Symbol
		LENGTH		
in	inches	*2.50	centimeters	cm
ft	feet	30.00	centimeters	cm
yd	yards	0.90	meters	m
mi	miles	1.60	kilometers	km
		AREA		
in²	square inches	6.50	square centimeters	cm²
ft²	square feet	0.09	square meters	m²
yd²	square yards	0.80	square meters	m²
mi²	square miles	2.60	square kilometers	km²
	acres	0.40	hectares	ha
		MASS (weight)		
oz	ounces	28.00	grams	g
lb	pounds	0.45	kilograms	kg
	short tons (2000 lb)	0.90	tonnes	t
		VOLUME		
tsp	teaspoons	5.00	milliliters	ml
Tbsp	tablespoons	15.00	milliliters	ml
fl oz	fluid ounces	30.00	milliliters	ml
c	cups	0.24	liters	l
pt	pints	0.47	liters	l
qt	quarts	0.95	liters	l
gal	gallons	3.80	liters	l
ft³	cubic feet	0.03	cubic meters	m³
yd³	cubic yards	0.76	cubic meters	m³
		TEMPERATURE (exact)		
°F	Fahrenheit temperature	5/9 (after subtracting 32)	Celsius temperature	°C

---

* 1 in. = 2.54 cm (exactly)

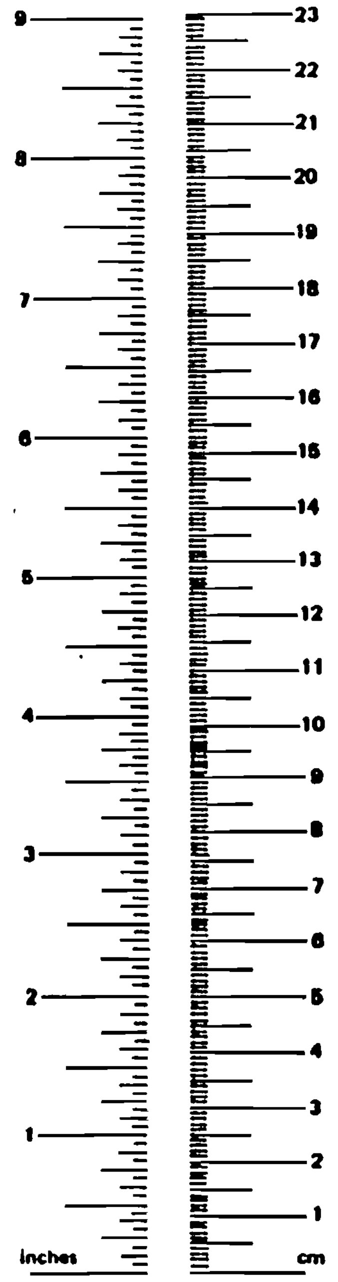

Approximate Conversions from Metric Measures

Symbol	When You Know	Multiply by	To Find	Symbol
		LENGTH		
mm	millimeters	0.04	inches	in
cm	centimeters	0.40	inches	in
m	meters	3.30	feet	ft
m	meters	1.10	yards	yd
km	kilometers	0.60	miles	mi
		AREA		
cm²	square centim.	0.16	square inches	in²
m²	square meters	1.20	square yards	yd²
km²	square kilom.	0.40	square miles	mi²
ha	hectares (10,000 m²)	2.50	acres	
		MASS (weight)		
g	grams	0.035	ounces	oz
kg	kilograms	2.2	pounds	lb
t	tonnes (1000 kg)	1.1	short tons	
		VOLUME		
ml	milliliters	0.03	fluid ounces	fl oz
l	liters	2.10	pints	pt
l	liters	1.06	quarts	qt
l	liters	0.26	gallons	gal
m³	cubic meters	36.00	cubic feet	ft³
m³	cubic meters	1.30	cubic yards	yd³
		TEMPERATURE (exact)		
°C	Celsius temperature	9/5 (then add 32	Fahrenheit temperature	°F

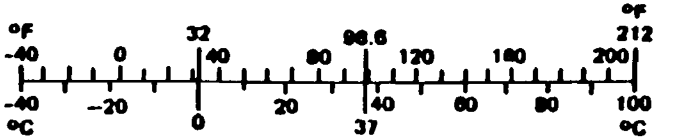

DOT/FRA/ORD-94/23
SAND89-2432
TTC-0945
Unlimited Release

Distribution
Category UC-722

THERMAL BOUNDARY CONDITIONS FROM ENGULFING FIRES*

J. A. Koski[1], Editor
B. L. Bainbridge[2], N. N. Brown[3], S. E. Gianoulakis[3], N. R. Keltner[4], J. T. Nakos[4],
V. F. Nicolette[2], K. B. Sobolik[4]

[1]Transportation Systems Technology Department (6642)
[2]Thermal and Fluid Engineering Department (1513)
[3]Transportation Systems Development Department (6643)
[4]Thermal Test and Analysis Department (2761)

Sandia National Laboratories**
Albuquerque, NM 87185

ABSTRACT

Determination of a realistic fire boundary condition provides cask designers with a tool to predict accurately the response of a cask in a fire. In one approach to determining this thermal input, data were analyzed from previous engulfing fire experiments on casklike objects. In another approach an analytical model was developed to investigate the influence of test objects on the fire. As has long been suspected, the cask and the fire environment strongly interact. The response of a cask in a fire is highly dependent on the physical and thermal characteristics of the cask; in fact, a very massive cask can alter the early fire environment. Therefore, it appears unlikely that a simple fire boundary condition can be derived that will accurately describe the response of a cask in a fire.

---

*This work was performed at Sandia National Laboratories, Albuquerque, New Mexico, supported by the U.S. Department of Energy under Contracts DE-AC04-76DP00789 and 94AL85000.

**A U.S. Department of Energy facility.

ACKNOWLEDGMENT

The authors would like to thank Jose Pena and Claire Orth from the U.S. Department of Transportation (DOT) for supporting the Sandia National Laboratories (SNL) Thermal Boundary Conditions work. Special thanks go to Bob Luna who thoroughly reviewed the final drafts and made several constructive suggestions that enhanced the report. Also, thanks to J. L. Moya of SNL and the staff of Creative Computer Services (CCS) for their review effort and assistance in preparing this manuscript.

CONTENTS

Section Page

CONTENTS (Concluded)

LIST OF FIGURES

LIST OF FIGURES (Concluded)

LIST OF TABLES

NOMENCLATURE

c = specific heat
c_p = specific heat at constant pressure
E = activation energy of fuel
h_s = convective heat transfer coefficient
k = optical path length
k' = integration variable
k_D = optical path length at far field boundary
k_{tc} = thermal conductivity
L = flame thickness
q_c = convective flux
q_{er} = emitted radiative flux
q_{ir} = local incident radiative flux
q_{net} = net absorbed heat flux
q_r = local radiative heat flux
q_{refl} = reflected radiative flux
q_t = total (radiative and convective) flux
R = universal gas constant
s = surface conditions
S''' = local volumetric combustion heat source
S_0''' = constant (reference) volumetric combustion heat source
t = time
T = local combustion gas temperature
T_b = back face temperature
T_f; T_{flame} = flame temperature
T_{fs} = free stream temperature
T_0 = reference temperature at which $S''' = S_0'''$
T_{rad} = temperature of the radiation source
T_s = surface temperature
T_1 = surface temperature of object in flames
T_2 = far field combustion gas temperature
U_∞ = uniform free stream velocity
x = coordinate along plate from leading edge
y = coordinate normal to plate from plate surface
α = absorption coefficient of combustion gases

NOMENCLATURE (Concluded)

α_s = surface absorption coefficient
ε_f = flame emissivity
ε_s = surface emissivity
κ = extinction coefficient
ρ = density of combustion gases
σ = Stefan-Boltzmann constant

ACRONYMS

DOT/FRA	U.S. Department of Transportation/Federal Railroad Administration
NRC	U.S. Nuclear Regulatory Commission
PDF	probability density function
RAM	radioactive materials
SNL	Sandia National Laboratories
SODDIT	Sandia One-Dimensional Direct and Inverse Thermal code
SWISH	Small Wind Shielded facility
TRUPACT	transuranic packaging transporter

1.0 INTRODUCTION

1.1 Background

Fire characterization and an understanding of the response of large objects in a fire are critical to the transportation industry, which moves radioactive materials (RAM) and other hazardous materials daily by truck and rail in certified packages. For spent nuclear fuel and other large quantity RAM these packages are typically large, heavy casks weighing up to 125 tons. For hazardous materials such as the highly flammable liquid hydrocarbons, relatively thin-shelled tank cars are often used for transportation. Radioactive material packages are designed and built to such that the contents remain inside the package in the event of an accident. If an accident occurs that involves severe impact, puncture, and/or fire, it is required by U.S. Nuclear Regulatory Commission (NRC) and U.S. Department of Transportation (DOT) regulations that the package not release its contents. For RAM casks in fires possible consequences of high heat loads are degradation of cask seals, melting of neutron or gamma shield materials, structural failures, or high fuel rod temperatures (in spent-fuel casks), which can cause rupture of the rods and release of radioactive material into the cask. Intense heat in a tank car carrying a flammable hydrocarbon can pressurize the contents and cause an explosion or leakage of additional fuel into the fire. Thus, in order to protect transportation personnel and the public, casks and tank cars are required by regulations to be capable of withstanding adverse thermal environments.

In order to demonstrate compliance with the regulations, packages or their components are sometimes tested in experimental pool fires, furnaces, or radiant heat facilities that simulate an accident-related fire. For analysis, thermal boundary conditions are important inputs for estimating the response of objects to fires. The actual damage to containers in fires is caused by temperatures that exceed material limits or by temperature gradients that cause excessive thermal stresses. Thus, the need is for thermal boundary conditions that lead to realistic estimates of temperatures and temperature gradients in designs.

1.2 Applicable Regulations

Before use in transporting material, RAM packages must meet the performance specifications outlined in Title 10, Code of Federal Regulations, Part 71 (10 CFR 71) (1984) and tank cars the specifications outlined in 49 CFR 179 (1986). Both regulations contain specific thermal tests or requirements that must be passed or met before the package or tank car can be used.

The RAM package regulations outlined in 10 CFR 71 were developed to ensure that the integrity of a transportation container is not compromised in the event of an accident. The cask must undergo sequential damage scenarios, including impact, puncture, and thermal loads. The thermal accident condition defined in the regulations states that the entire surface of a package must be exposed for not less than 30 min to a heat flux not less than that of a radiation environment of 800°C with an emissivity coefficient of at least 0.9. For calculation purposes the surface absorptivity is assumed to be either 0.8 or that value the package may be expected to possess if exposed to a fire, whichever is greater. In addition, convective heat input, when significant, must be included on the basis of still, ambient air at 800°C (i.e., free convection). This does not actually specify a fire temperature but specifies a minimum heat flux level that the package must be capable of withstanding in an accident. Adherence to the regulations also can be demonstrated by direct test in a fully engulfing hydrocarbon fuel fire for 30 min.

Section 179.105-4 of the Code of Federal Regulations (49 CFR 179.105-4) is a test specification for evaluating thermal protection systems used on tank cars. This thermal protection system, that usually consists of insulating materials and weather resistant surfaces, reduces heat flux to the liquid contents in the tank car, allowing more time for the contents of the car to vent through a safety release valve. This regulation defines a complete experimental simulation. A torch is used to simulate a pool fire. The source of the simulated pool fire must be a hydrocarbon fuel with a flame temperature of 870°C ± 38°C for the duration of a 100-min test. The regulations outline the calibration sequence. In this specification, the heat flux is defined with a calibrated specimen. This requirement is based on actual tank car tests conducted in the 1970s. These tests were conducted on nominal 33,000-gallon capacity tank cars filled with a flammable liquid that were exposed to open pool fires. These tank cars were tested both with and without thermal protection systems.

These two sets of regulations differ greatly, and a direct comparison between them of the total heat input and thermal response of typical packagings cannot easily be made (Moya and Brown, 1989). Neither set of regulations is necessarily realistic in modeling the thermal load that a package receives if it is engulfed in an actual fire of the same duration. Both regulations are thought to be conservative, i.e., encompassing most severe fire conditions; that fact is also not easily demonstrated.

1.3 Objectives of Present Work

This work was supported by the DOT's Federal Railroad Administration (DOT/FRA) as part of an ongoing program aimed at understanding the response of rail casks transporting radioactive materials in a fire during a hypothetical accident.

In light of the present regulations, the objective of this work was to develop a boundary condition that rail cask designers can use to realistically model the response of a package in an actual fire. To perform a thermal analysis, an initial condition is required, usually the initial temperature distribution of the package, as well as thermal boundary conditions. These boundary conditions are usually in the form of local environment temperatures, such as flame temperatures, or incident heat fluxes, which may include convection and radiation. Not all RAM packages will have identical physical and therefore thermal characteristics. As a result, the boundary condition determined should be applicable to a variety of packages: thermally thick or thin walled, and physically large or small.

1.4 Thermal Boundary Condition Considerations

Determination of an appropriate thermal boundary condition for a package in a fire is not straightforward for many reasons. Fire environments are highly complex and difficult to model. Flame temperatures, gas velocities, soot concentrations, and energy release rates are all fluctuating functions of position, oxidizing agent, and time. In the fires of interest—large and unconfined—the flames are highly turbulent and are greatly influenced by wind.

In addition, the heat fluxes in fires are both radiative and convective. The fraction of each depends on several factors, such as size of the fire, fuel type, size of the object, surface temperature of the object, and duration in the fire, and neither is easily quantified. This complicates determination of appropriate thermal boundary conditions more than in a situation where only one mode of heat transfer is important.

For a given incident heat flux, objects in fires also respond differently corresponding to their physical and thermal characteristics. For example, for the same incident heat flux, thick-walled objects heat up less quickly than thin-walled objects. This makes the development of a single, all-encompassing thermal boundary condition difficult.

Finally, the large size and mass of RAM transport casks can provide a significant heat sink capacity. Some fire tests have shown that in the same fire, large, thermally massive objects receive lower incident heat fluxes than small objects. Gregory et al. (1987a) have postulated that large, thermally massive objects can significantly influence the surrounding fire environment. If such an influence exists, it would further complicate the determination of appropriate thermal boundary conditions for a package in a fire because any interaction between an object and the local fire environment would be strongly dependent on the size and mass of the object.

1.5 Related Work

There have been many attempts at modeling heat transfer to objects in fires. The Birk and Oosthuizen (1982) model calculates radiative heat fluxes from two-dimensional flames to a horizontal cylinder. In this model it is assumed that the flame is a participating medium with a uniform temperature and extinction coefficient. Probably as a result of this assumption, the model predicts that the highest heat fluxes will occur at the top of a cylinder engulfed in a fire and the lowest heat fluxes at the bottom. This is in direct contrast to what is actually seen in pool fires, where the highest heat fluxes are measured at the bottom of a large cylinder and the lowest heat fluxes at the top (Gregory et al., 1987a,b). These outcomes clearly illustrate some of the problems with current fire models.

The work of Tunc and Karakas (1985) and Wong and Steward (1988) is similar to that of Birk and Oosthuizen (1982) in that flame volume is assumed to be at a uniform temperature and is treated as a participating medium. However, the two more recent studies calculate radiative heat fluxes from a three-dimensional, rather than a two-dimensional flame to a surface. Tunc and Karakas (1985) calculate heat fluxes to a flat plate; Wong and Steward (1988) calculate heat fluxes to a horizontal cylinder.

Fry (1985) presents two models for calculating heat fluxes from a fire to a planar surface. In one model the radiative heat transfer is assumed to occur between black surfaces at the flame temperature and the test object temperature. In the second model the flame volume is treated as a participating medium at a uniform temperature. The results show how radiative heat transfer in a sooty fire is affected by flame thickness and that the presence of a cold wall can influence temperature measurements near it.

All of these models have two limitations. First, the flames are assumed to be at a uniform temperature. Actual fires have a substantial vertical temperature gradient, on the order of several hundred degrees (Gregory et al., 1987a,b). This becomes very significant, since radiative heat transfer is proportional to the fourth power of absolute temperature and is probably the main reason for the models' predictions that the largest heat fluxes will occur at the top of the cylinder instead of at the bottom, as experimentally observed.

The second limitation in these models is the assumption that the flames and test object do not interact. The thermal massiveness, and hence thermal capacitance, of the object does not enter into the calculations other than as a reradiation term from the object surface. Therefore, these models cannot be used to investigate whether a thermally massive object influences the surrounding flames.

1.6 Present Approach

Determining appropriate thermal boundary conditions for a large object in a fire can be attempted in many ways. Because it is unclear what the best approach is, this study took two different approaches to the problem, discussed below. In them some of the questions that had not previously been considered in detail were addressed, namely (1) the partitioning of radiative and convective heat transfer in a fire and (2) the interaction between a large, thermally massive object and the fire itself.

In the first approach experimental data were analyzed to extract a thermal boundary condition and partitioning of the convective and radiative components of the total heat flux from a fire to an object was considered. In many models convective heat transfer is neglected, since radiative heat transfer usually dominates in a fire. This assumption may be appropriate once a fairly uniform fire is established or for a thin-walled object, but is inappropriate early in a fire, when convection plays a much more significant role. In order to model accurately the response of an object to a fire, these two components of heat transfer may have to be separated. One relatively new method of resolving this problem is use of transpiration radiometers, which can measure radiative heat flux in a fire. Sandia National Laboratories (SNL) has recently done fire tests using these instruments. Total heat flux can be calculated with calorimeters or other methods. The difference between the total heat flux and the radiative heat flux is the heat flux from convection. This approach and results obtained with it are discussed in Section 2.0.

The second approach involved an analytic investigation of the effects of a large, thermally massive structure on the fire itself. As discussed above, experiments show that in the same fire, the cold wall heat flux to a large, massive structure is different from the cold wall heat flux to a small calorimeter. The reason for this difference may be that the massive object is capable of absorbing so much energy that it can actually alter the local fire environment. However, this hypothesis had never been investigated analytically to determine its validity. If it is valid, a thermal boundary condition depends not only on the fire environment but also on certain characteristics of the object itself. Section 3.2.2 provides a discussion of an analytic model developed to illustrate the significance of the thermal mass effect. The results of this model are not intended for use in predicting a thermal boundary condition. Rather, the intent is to (1) demonstrate analytically that such an interaction between fire and test object exists and (2) determine the relative magnitude of significance that various parameters—flame temperature, characteristic length, wall temperature, and so on—can have on thermal transport. This approach and results obtained with it are discussed in Section 3.2.

2.0 DATA PRESENTATION AND ANALYSIS

2.1 Data Compilation and Comparisons

The large pool fire test facility at SNL in Albuquerque, New Mexico, has been the scene of numerous large-scale tests over the past several years. The most recent test involved the transuranic packaging transporter (TRUPACT-II) container, with an extensive array of sophisticated thermal sensors for examining the behavior of the fire environment. This section examines the data obtained from previous tests and compares the results of temperature and heat flux measurements.

Table 2.1 lists large-scale fire tests performed over the past several years. Included in the table are most of the types of instrumentation used to monitor the fire environment: thermocouples mounted on towers; calorimeters, ranging from shrouded and unshrouded cylinders 10.2 cm to 1.42 m in diameter to shrouded and unshrouded plates with walls of different thicknesses; and "flame" thermocouples, mounted near the surface of calorimeters. Other instrumentation types used less frequently are bidirectional velocity sensors, pool surface calorimeters, and transpiration radiometers.

The focus in the comparison of test results will be on the average values obtained from each test for each of the principal instrumentation types. In general, every test did not have exactly the same array of instrumentation, or the data may have been processed differently so that a comparison with each of the large pool fires may not be possible. Also, new measurement techniques and data-processing methods have been developed over the years, and this evolution in test technology is reflected in the results.

2.1.1 Tower Thermocouples

Tower-mounted thermocouples are used to obtain vertical temperature profiles within a pool fire. The variation from one tower to the next shows the distortion of the thermal environment due to such factors as wind, the test unit, and the large turbulent structures of the fire. Tower data can be used to generate a signal that indicates the presence or absence of flame (usually caused by wind) and allow the examination of fire data during "flame present" periods.

Typically the thermocouples are 1.59 mm in diameter, are Inconel sheathed, and have ungrounded junctions. They are mounted on the towers at elevations between 1 and 15 m and extend several centimeters horizontally into the fire. Under typical test conditions the 63.2% first-order response time for the thermocouples is between 1 and 4 s.

Thermocouples mounted on towers are common to all the large pool fire tests shown in Table 2.1. Generally four to eight towers with two to seven thermocouples are placed near the test unit or in the central region of the pool, with thermocouple locations between 1 and 12 m above the pool floor. Readings are recorded every 5 to 10 s for the duration of the fire.

Data from the tower thermocouples can be presented as temperature versus time or as average temperatures for the duration of the fire. Averaged data can also be examined in various ways. The entire data set, including periods of high wind can be averaged, or the data can be "conditioned" by removing portions of the data set that correlate with higher wind velocities. Conditioning can take several forms. The data for the TRUPACT-I(0) and TRUPACT-I(1) were conditioned by using the average temperature as the transition point between "flame present" and "flame absent" states. Data from DOT tests A through C and the Nuclear Winter test were conditioned based on the bimodal shape of the probability density function (PDF) for each data set.

Table 2.1

Summary of Fire Environment Instrumentation for Large Pool Fires

Test	Year	Instrumentation	Type	No.	Location	Description
DOT Fire Test series	1983	Fire thermocouples	Tower	3	2.28, 3.48 m	Height above pool bottom
			Tower	5	2.28, 3.48, 6.35,12.04 m	
		Calorimeters	Cylinder	2	1.83, 3.16 m	10.2-cm diameter, 3.2-cm wall
			Cylinder	2	1.83, 3.16 m	20.3-cm diameter, 3.2-cm wall
			Cylinder	1	1.63 m	1.42-m diameter, 3.2-cm wall
		Flame thermocouples		12	5.08 cm off surface	Mounted off surface of 1.42-m calorimeter
PNC* Truck Fire	1984	Fire thermocouples	Tower	4	2.29, 2.90, 3.51, 6.10 m	Height above pool bottom
		Calorimeters	Cylinder	4		10.2-cm diameter, 3.2-cm wall
TRUPACT-I(0)	1984	Fire thermocouples	Tower	4	1.37, 2.29, 2.90, 3.51, 4.72, 6.10 m	Height above pool bottom
		Calorimeters	Cylinder	2	1.98 m	
TRUPACT-I(1)	1986	Fire thermocouples	Tower	4	1.37, 2.29, 3.51, 4.72, 6.10 m	Height above pool bottom
			Tower	1	1.37, 2.29 m	
			Tower	1	1.50, 2.21, 2.80, 3.40, 4.09, 4.78, 3.43, 6.10 m	
		Calorimeters	Cylinder	2	1.98 m	10.2-cm diameter, 3.2-cm wall
			Plate	1		0.64- and 0.10-cm walls
			Arm	2		Two concentric cylinders, thin outer wall
		Flame thermocouples		9	10.2 cm off surface	Off 0.64-cm side of plate calorimeter
Nuclear Winter	1987	Fire thermocouples	Tower	4	1.37, 2.29, 3.51, 4.72, 6.10 m	Height above pool bottom
			Tower	1	2.21, 3.40, 4.78, 6.10, 9.14, 12.19, 15.24 m	
		Calorimeters	Cylinder	2	2.0 m	10.2-cm diameter, 3.2-cm wall
			Cylinder	1		1.42-m diameter, 3.2-cm wall, shrouded and unshrouded sections
			Plate	1		1.02-, 6.35-, 19-mm walls
		Flame thermocouples		2	10.2 cm off surface	Off 1.02- and 19-mm walls of plate calorimeter
				8	5.08 cm off surface	Off surface of unshrouded 1.42-m calorimeter

---

*PNC =Pacific Nuclear Corporation

Table 2.1

Summary of Fire Environment Instrumentation for Large Pool Fires (Concluded)

Test	Year	Instrumentation	Type	No.	Location	Description
TRUPACT-II(1)	1988	Fire thermocouples	Tower	4	1.37, 2.29, 3.51, 4.62, 6.10 m	Height above pool bottom
			Tower	1	2.21, 3.40, 4.78, 6.10, 9.14, 12.19, 15.24 m	
		Calorimeter	Cylinder	4	2.08 m	10.2-cm diameter, 3.2-cm wall
			Cylinder	1		1.42-m diameter, 3.2-cm wall, shrouded and unshrouded sections
			Plate	1		0.89-, 4.76-, 19-mm walls
		Flame thermocouples		2	10.2 cm off surface	Off 1.02- and 19-mm walls of plate calorimeter
				8	5.08 cm off surface	Off surface of unshrouded 1.42-m calorimeter

The PDF was produced from a histogram of the temperatures measured during a test by a higher-elevation thermocouple. Next, the number of times a temperature fell between two levels was counted. The resulting bimodal shape of the histogram (number of occurrences versus the temperature) suggests two temperature ranges: one corresponding to periods of low wind and one for periods of higher wind speeds. The selection of the transition point is somewhat arbitrary and depends on the shape of the PDF, but it lies between the two peaks of the bimodal distribution.

The average and "flame present" tower temperatures for each test are listed in Tables 2.2 and 2.3 and plotted in Figures 2.1 and 2.2, respectively. The averages for both cases are very similar even though each test had slightly different tower locations and wind conditions. The range in average wind speeds is shown in Table 2.4.

The effect of conditioning the temperature data is to move the location of maximum average temperature upward in elevation and to lower the average temperature of the lowest elevations. Also, the slope of the temperature profile versus height is much flatter after wind effects have been reduced. In general, the implications for performing a test under no-wind conditions would depend on the size and location of the test article. The maximum temperatures would be similar, but the no-wind test would have a much more uniform temperature environment above 2.5 m.

2.1.2 Calorimeters

Calorimeter designs used in large pool fires vary from cylinders to plates. The cylinders range in size from 10.2 cm to 1.42 m in diameter and in mass from 13 kg to 10 tons. Of principal interest are the 10.2-cm- and 1.42-m-diameter cylindrical calorimeters and the plate calorimeters. Net heat flux data are obtained from the inner-wall temperatures by applying a one-dimensional inverse heat conduction code, the Sandia One-Dimensional Direct and Inverse Thermal (SODDIT) code (Blackwell et al., 1987). A cold wall heat flux value is calculated by adding the heat flux radiated by the hot wall of the calorimeter to the net value:

$$q''_{\text{cold}} = q''_{\text{net}} + 0.85\sigma\left(T^4 - T_0^4\right) \tag{2.1}$$

where q''_{cold} is the cold wall heat flux, q''_{net} is the measured net heat flux, σ is the Stefan-Boltzmann constant, T is the actual wall temperature, and T_0 is the cold wall temperature. Cold wall heat flux is a calculational artifice that permits the comparison of heat flux histories for the various calorimeters as if they all had the same cold surface temperature, hence the term "cold wall heat flux." Inconsistencies among heat flux measurements evaluated at the same cold wall temperature can indicate that the laws for radiant heat transport in a transparent medium are not being met in the experiment. In this case, the rules of heat transfer for a participating medium discussed in Section 3.0 must be considered to explain the differences.

2.1.2.1 Small Cylindrical Calorimeters

The 10.2-cm-diameter cylinder was divided circumferentially into four quadrants, each separated from adjacent sections by insulation. Wall material was a mild steel (A517), 3.18 cm thick. Typically the cylinders were mounted horizontally. Each quadrant had a type K thermocouple mounted at the center of the inner-wall surface.

A compilation of average cold wall heat flux data is shown in Table 2.5 and Figure 2.3. Mean values were obtained by averaging over the entire test period without applying a conditioning signal. The DOT fire data were available only as an average over the three tests and were reported only for the top and bottom quadrants from the lower and upper calorimeters, respectively. The data from TRUPACT-I(1) are probably too low, owing to a data acquisition problem that

Table 2.2

Comparison of Average Tower Temperatures for Several Large Pool Fires

Average Tower Temperatures (°C)

Height (m)	DOT Fires			TRUPACT-I(0)	TRUPACT-I(1)	Nuclear Winter	TRUPACT-II(1)
	Test A	Test B	Test C				
1.37				911	874	920	928
2.28	921	935	911				
2.29				981	1024	958	933
2.90				858			720
3.48	768	799	775				
3.51				744	861	882	546
4.72				744	703	748	
6.10				518	597	639	
6.35	529	582	549				
12.04	394	402	350				

Table 2.3

"Flame Present" Average Tower Temperatures for Several Large Pool Fires

Average Tower Temperatures (°C)
"Flame Present" Data

Height (m)	DOT Fires			TRUPACT-I(0)	TRUPACT-I(1)	Nuclear Winter	TRUPACT-II(1)
	Test A	Test B	Test C				
1.37				866	778	853	
2.28	990	1017	979				
2.29				1022	1015	988	
2.90							
3.48	981	1044	996				
3.51				931	1036	1014	
4.72				950	968	1006	
6.10				792	895	952	
6.35	899	903	893				
12.04	710	687	623				

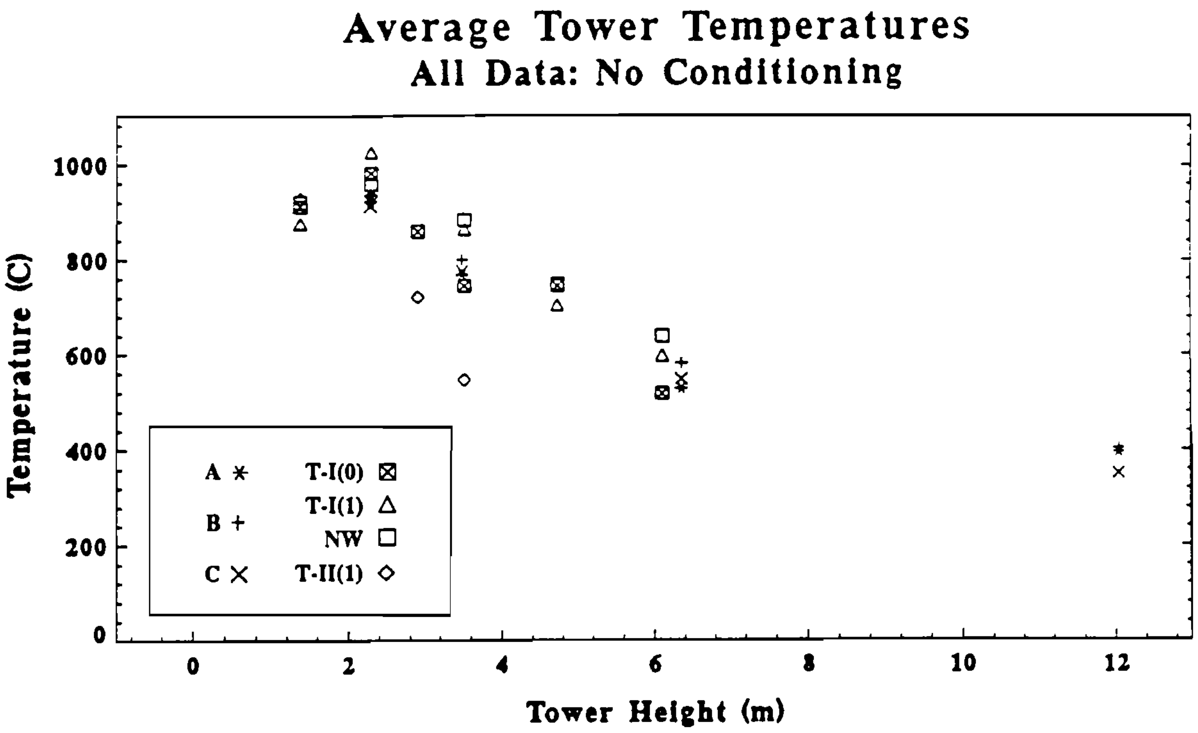

Figure 2.1 Average Tower Temperatures–No Conditioning

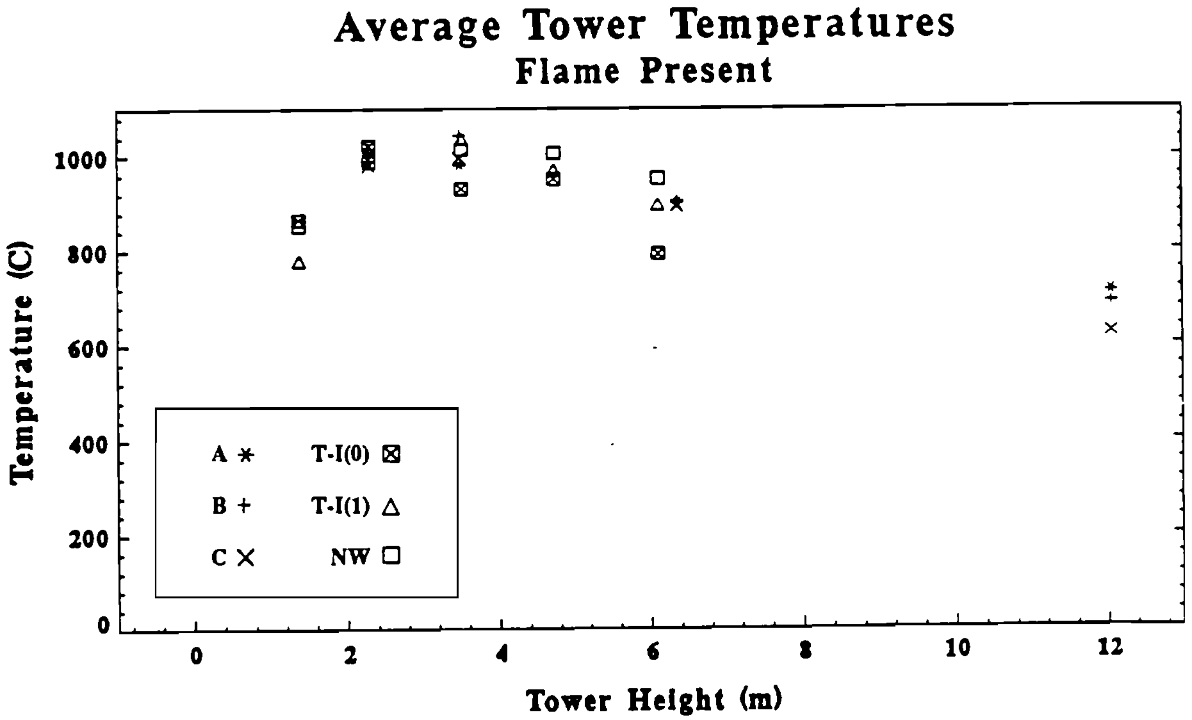

Figure 2.2 Average Tower Temperatures–"Flame Present"

Table 2.4

Average Wind Speed for Large Pool Fire Tests

Pool Fire Test	Average Wind Speed (m/s)	Reference
DOT-A	2.0	Gregory et al., 1987a,b
DOT-B	1.2	Gregory et al., 1987a,b
DOT-C	1.5	Gregory et al., 1987a,b
PNC	<1.2	Mata and Keltner, 1984
TRUPACT-I(0)	1.7	Mihalovich et al., 1985
TRUPACT-I(1)	1.2	Keltner et al., 1987
Nuclear Winter	2.8	Schneider et al., 1988

Table 2.5

Average Cold Wall Heat Flux Data for Small Cylindrical Calorimeters

Small Cylindrical Calorimeters

Test		Average Cold Wall Heat Flux (kW/m^2)
DOT Fires	Lower	165
	Upper	135
	Mean	150
TRUPACT-I(0)	North	144.7
	South	113.5
	Mean	129.1
TRUPACT-I(1)	North	99.3
	South	88
	Mean	93.7
Nuclear Winter	East	131.2
	West	147.5
	Mean	139.4
TRUPACT-II(1)	North	94.1
	East	112.9
	South	106.9
	West	181.1
	Mean	123.8

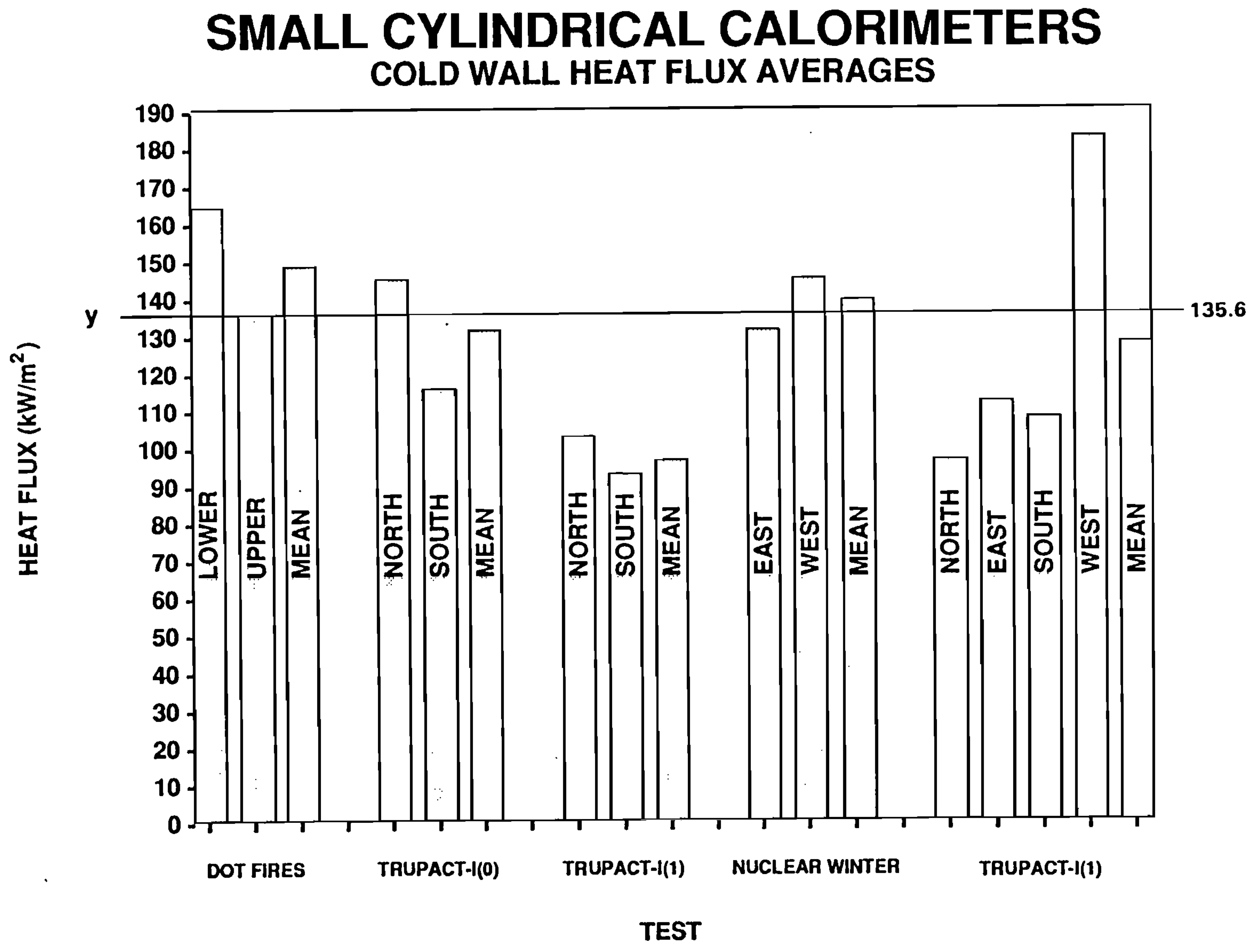

Figure 2.3 Average Cold Wall Heat Fluxes for Small Cylindrical Calorimeters (135.6 kW/m^2), TRUPACT-I(1) Data Not Included

developed during the test. Overall, the mean values lie in a fairly tight grouping—with a group mean of 135.6 kW/m^2 and a standard deviation of s = 11.6, not including the TRUPACT-I (1984) test—even though each test had slightly different locations for the small calorimeters.

2.1.2.2 Large Calorimeter

The 1.42-m-diameter calorimeter was included in the DOT Fire Test series, the Nuclear Winter test, and the TRUPACT-II(1) test. Its size allows comparison of scale effects for objects ranging in size from 10.2-cm calorimeters to massive transportation containers. The large calorimeter was used initially without shrouds (see Figure 2.4) for the DOT test series, and later with shrouded and shrouded-insulated sections. The addition of the shroud, which consisted of a 0.89-mm-thick mild steel sheet, allows examination of the behavior of walls with different heating characteristics and their interaction with the fire environment. Figure 2.4 shows a cross section of the calorimeter and the locations of the instrumentation.

Table 2.6 compares the currently available data for the large calorimeter. For the Nuclear Winter test and the TRUPACT-II(1) test, the large calorimeter had one section unshrouded, exposing the 3.18-cm-thick wall directly to the fire, and two shrouded sections. One shrouded section contained a 2.54-cm-thick layer of high-temperature insulation between the shroud and the inner wall, while the other section did not.

Comparison of the heat fluxes at the different angular locations—top, east, bottom, and west—shows the wind-driven behavior that has been typical of all the fire tests: the stations most protected from the wind undergo the highest heat flux levels. Even with wind effects, the average cold wall heat flux levels were consistently in the range of from 80 to 100 kW/m^2.

The shrouded sections of the calorimeter showed significant changes in response to fire compared to the unshrouded section. Surface temperatures rose more rapidly, and net heat fluxes fell to very low levels. This is even more evident for the shrouded-insulated section of the calorimeter, which isolated the shroud from the heat-sinking effect of the heavy inner wall. The average surface temperatures increased from 589°C for the unshrouded section to 951°C for the shrouded and insulated section.

Information about the behavior of the large calorimeter can be applied in the design of large transportation containers. The design tradeoffs related to the mass and thermal response of the container can be examined by a comparison of the results obtained from the three wall sections of the large calorimeter. The unshrouded section demonstrates the slow heating of a thick steel shell, while the thin shrouds rapidly achieve quasi-equilibrium with the flame temperature.

2.2 Recent Data Analyses

The bulk of the detailed experimental data presented in this section came from a series of three fire tests performed in a 9-by-18-m pool on the TRUPACT-II transport container. Several experiments were installed in the same pool with TRUPACT-II for studies of heat transfer in fires and developing more accurate instrumentation. The data presented here were acquired from the plate calorimeter and the 1.4-m-diameter cylindrical calorimeter.

2.2.1 Experimental Apparatus

The thick-walled side of the plate calorimeter consisted of two steel plates, 3.05 cm wide by 30.5 cm long, mounted with the 3.05-cm dimension vertical. The lower portion of the calorimeter shown in Figure 2.5 shows a cutaway view of the plate calorimeter at its most heavily instrumented area. One steel plate was made of 1.9-cm-thick mild steel and the other of 0.48-cm-thick stainless steel. The plates were mounted side by side, with only one face of each plate

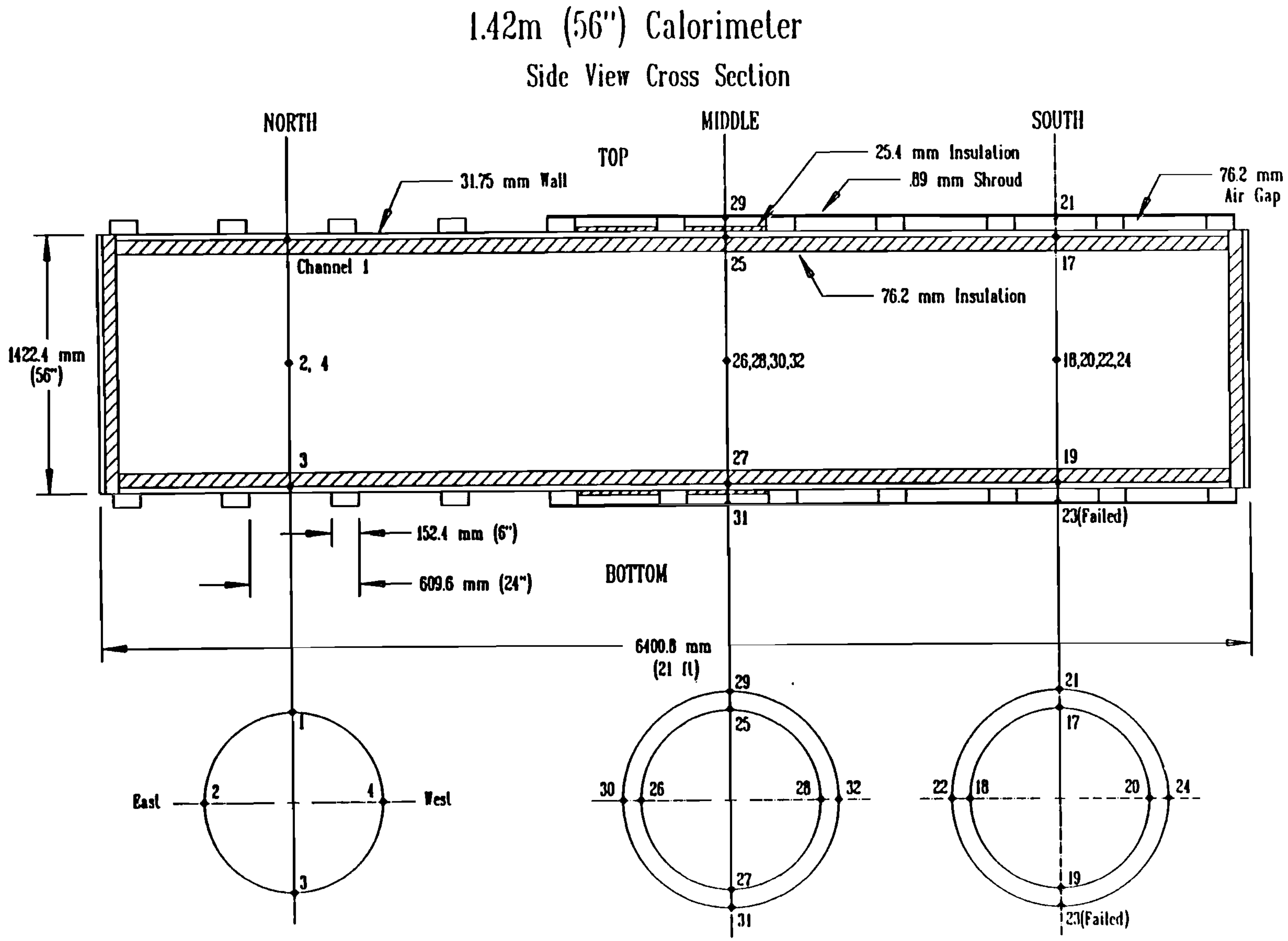

Figure 2.4 Cross Section of Large Calorimeter

Table 2.6

Comparison of Large Calorimeter Data (1.42-m Cylindrical Calorimeter)

		DOT Fires*			Nuclear Winter		TRUPACT-II(1)	
Calorimeter Section	Location	Test A: Cold Wall Heat Flux (kW/m^2)	Test B: Cold Wall Heat Flux (kW/m^2)	Test C: Cold Wall Heat Flux (kW/m^2)	Average Surf. Temp. (°C)	Cold Wall Heat Flux (kW/m^2)	Average Surf. Temp. (°C)	Cold Wall Heat Flux (kW/m^2)
Unshrouded	Top	62	55	64	285	31	601	114
	East	79	66	68	493	91		
	Bottom	110	114	116	627	127	573	106
	West	90	101	106	422	62	594	111
	Average	85	84	88	457	78	589	104
Shrouded	Top	NA**	NA	NA	401		523	39
	East	NA	NA	NA	835		618	55
	Bottom	NA	NA	NA				
	West	NA	NA	NA	699		765	87
	Average	NA	NA	NA	635		635	60
Shrouded-insulated	Top	NA	NA	NA			918	107
	East	NA	NA	NA			951	118
	Bottom	NA	NA	NA			919	109
	West	NA	NA	NA			1016	143
	Average	NA	NA	NA			951	119

---

*The orientation of the DOT calorimeter was east-west, and so north-south stations were mapped to east-west, respectively.

**NA: Not available on this test.

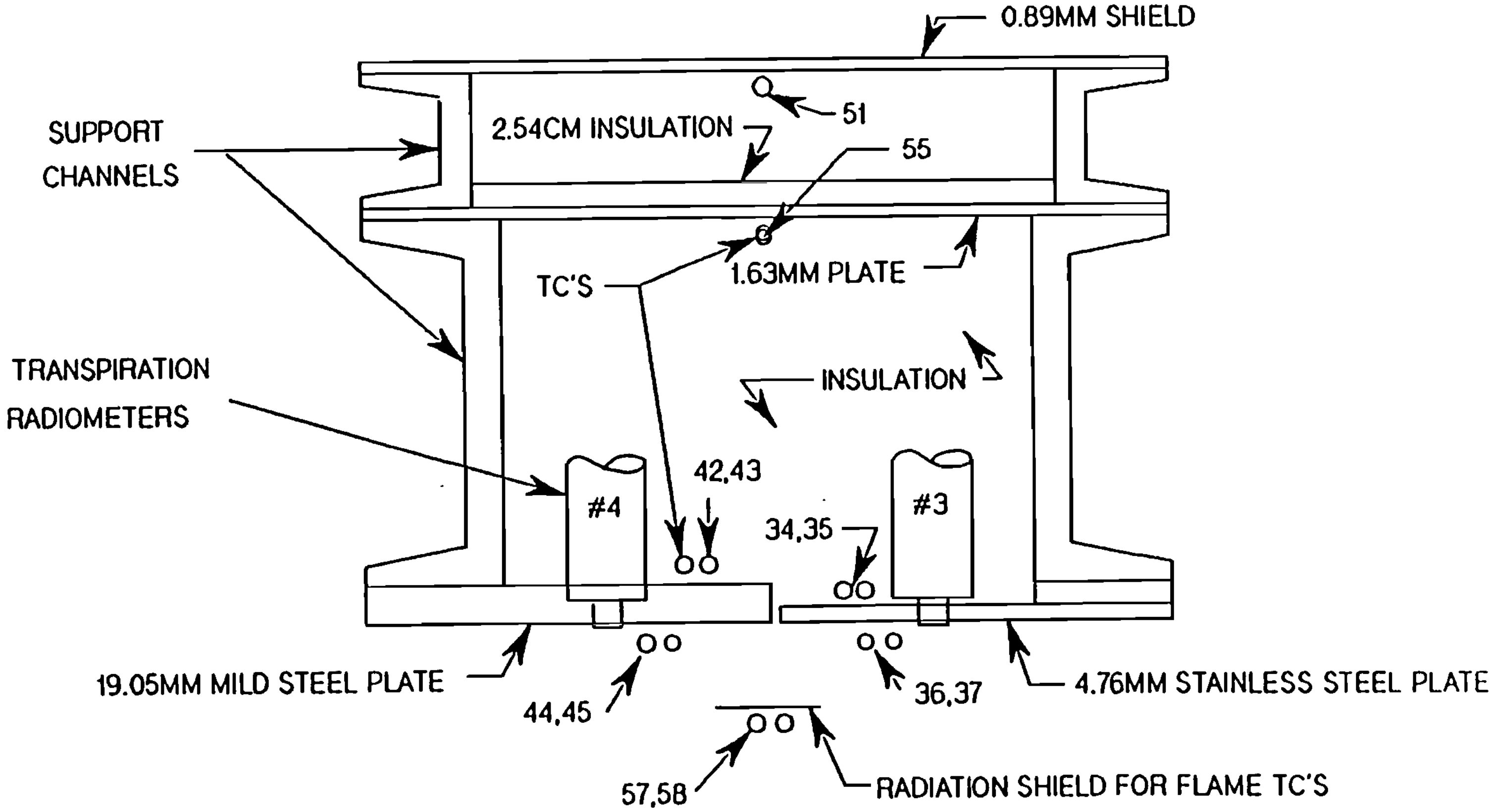

Figure 2.5 Section Through Plate Calorimeter (numbers identify thermocouple locations)

exposed to the fire. The back sides of both thick plates were insulated with about 25.4 cm of high-temperature insulation. The plates were held in place with steel channels and mounted on a stand. The thin plate side could represent the relatively thin outer skin of a shipping container, such as TRUPACT-II, which has a 6.4-mm stainless steel skin and a heavily insulated interior.

The thin-walled side of the plate calorimeter, shown in the upper portion of the calorimeter in Figure 2.5, consists of two thin plates, one 0.89 mm thick and the other 1.63 mm thick. Both are made of mild steel. Between the outer, 0.89-mm-thick shield and the inner, 1.63-mm-thick plate is an air gap and 2.54 cm of insulation. This configuration resembles the situation that occurs in a thermally protected railroad tank car. Only the 0.89-mm shield was exposed to fire.

Both the thick- and the thin-walled sides of the plate calorimeter were instrumented with thermocouples. In addition, the thick-walled side was instrumented with two transpiration radiometers to measure the incident radiative heat flux to the plates.

The cylindrical calorimeter consists of a cylinder made of A517 steel, 1.4 m in diameter by 6.40 m long. It has a wall thickness of 3.18 cm and strengthening ribs every 61 cm. This calorimeter was placed in the west end of the pool, TRUPACT-II was placed in the east end, and the plate calorimeter was placed roughly between. Figure 2.6 shows a cross-sectional view of the cylindrical calorimeter and Figure 2.7 shows a plan view of the pool layout. Like the plate calorimeter, the cylindrical calorimeter has thick- and thin-walled locations. The north end of the cylindrical calorimeter (placed with the long dimension directed north-south) was the thick-walled end, with the 3.18-cm-thick steel exposed to the fire. The south end had a 0.89-mm-thick steel shroud covering the heavier, 3.18-cm-thick wall of the cylinder. The calorimeter has a section with an air gap and 2.54 cm of insulation between the 0.89-mm shroud and the 3.18-cm wall of the cylinder. It also has a section with the air gap but without the insulation.

The cylindrical calorimeter has instrumentation similar to that installed in the plate calorimeter: thermocouples and transpiration radiometers. Two types of thermocouples were installed on the cylindrical calorimeter: 1.59-mm-diameter inconel-sheathed thermocouples on the back face and pencil-probe-type eroding thermocouples (NANMACs) on the front face. The eroding thermocouples are designed to measure front face temperatures and were installed only on the thick-walled end of the cylindrical calorimeter.

In each test about 20 cm of JP-4 jet fuel floated on about 60 cm of water. The bottoms of the plate calorimeter and the cylindrical calorimeter were about 1.78 m from the bottom of the pool, or about 1 m from the top of the initial fuel level.

2.2.2 Thermal Test Data

Discussion of the thermal test data is divided into three parts. First, front face or surface temperature measurements are reviewed; then cold wall heat flux values on both the plate and cylindrical calorimeter. Finally transpiration gauge data, which directly measure the incident radiative component of the heat flux to the plate and cylindrical calorimeters, are presented.

2.2.2.1 Front Face Temperatures

Front face temperature data are required to establish the convective heat transfer to a surface and to calculate the radiation from the surface to the surrounding environment. Figure 2.8 (see also Figures A.1 through A.3 in the appendix) shows comparisons of the measured and calculated front face temperatures on both plates of the thick-walled side of the plate calorimeter and on the top and bottom of the 1.4-m-diameter cylindrical calorimeter. The front face temperatures were measured

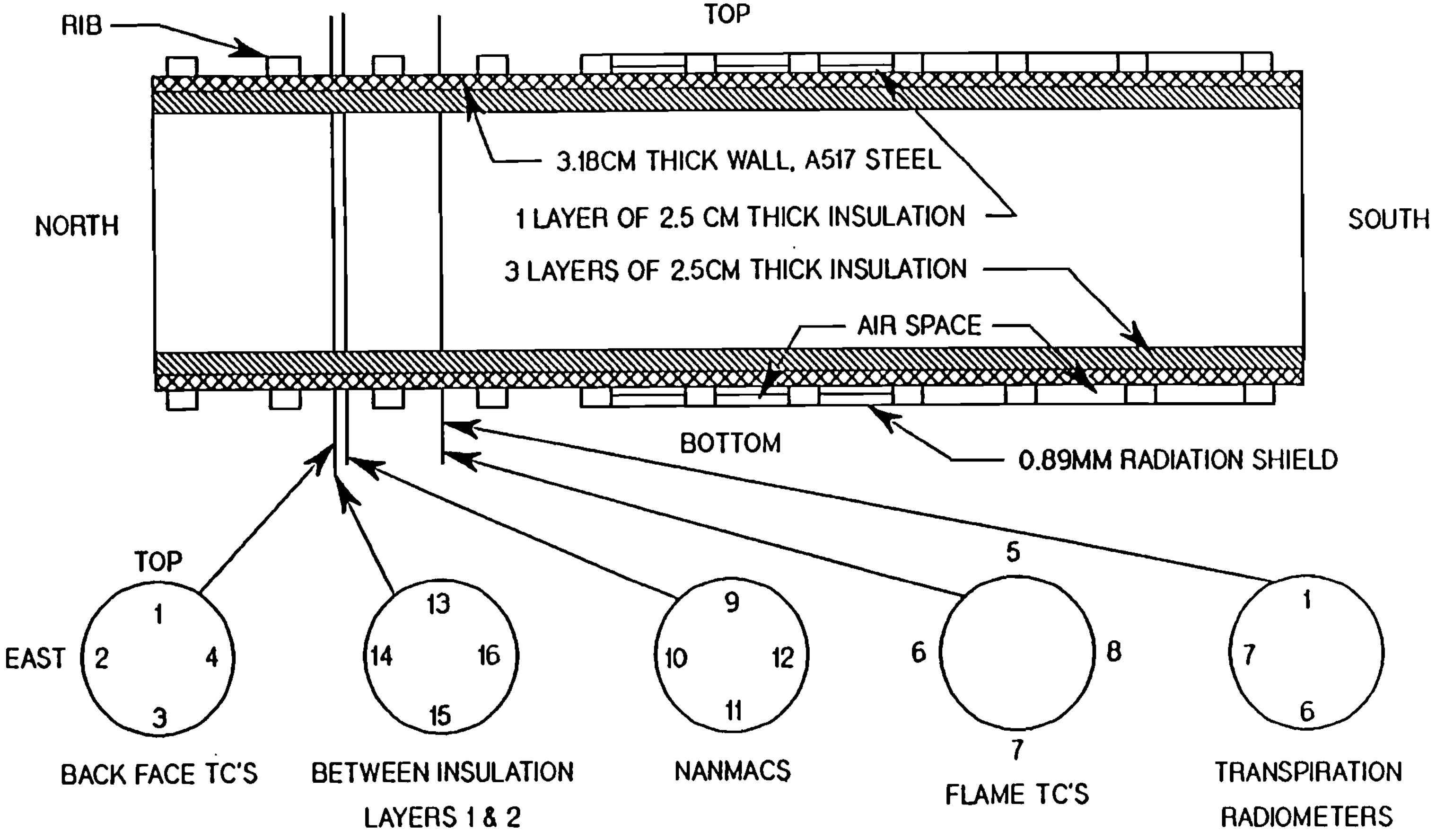

Figure 2.6 Cross-Sectional View of 1.4-m-Diameter Calorimeter (numbers identify thermocouple locations)

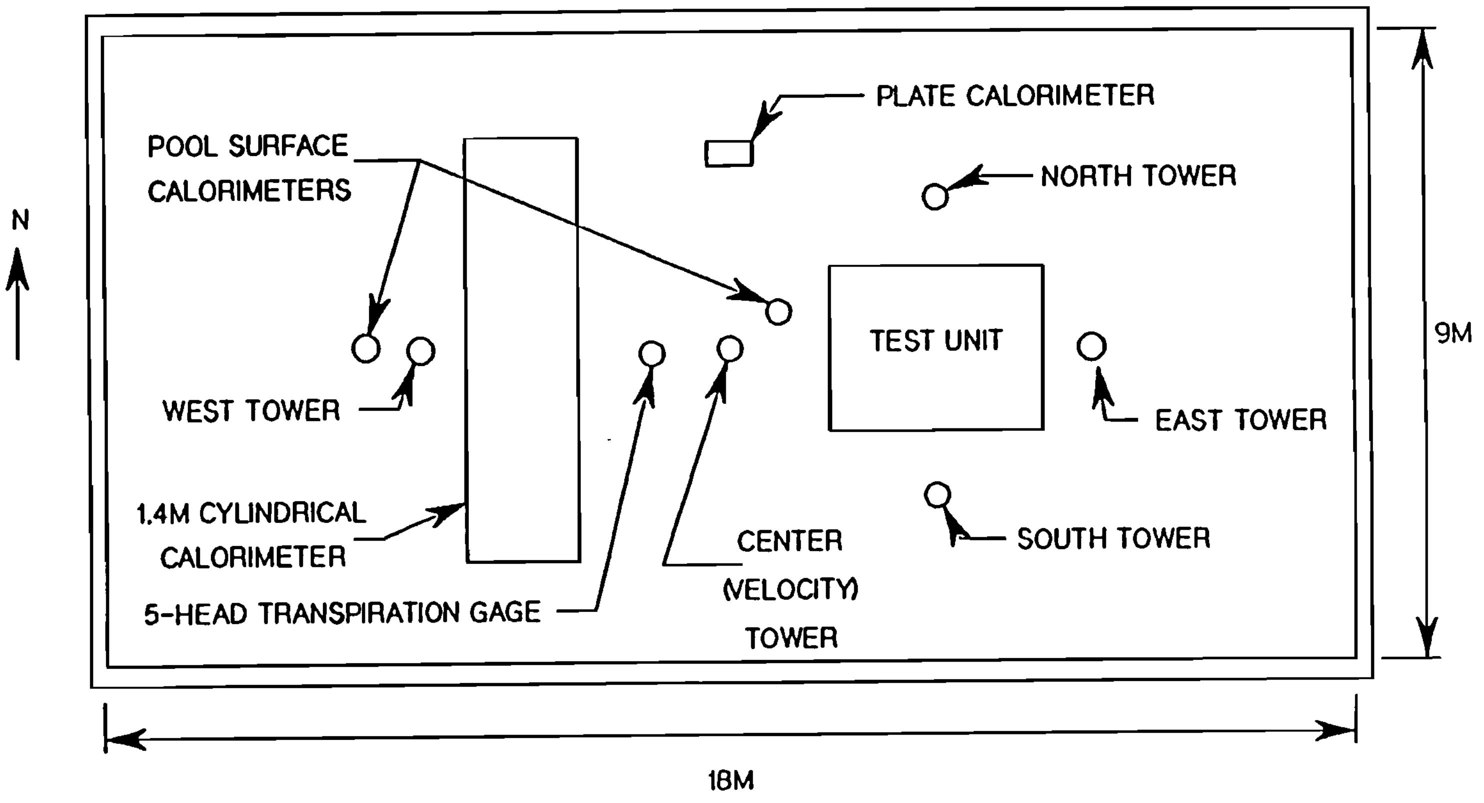

Figure 2.7 Pool Layout (9 by 18 m)

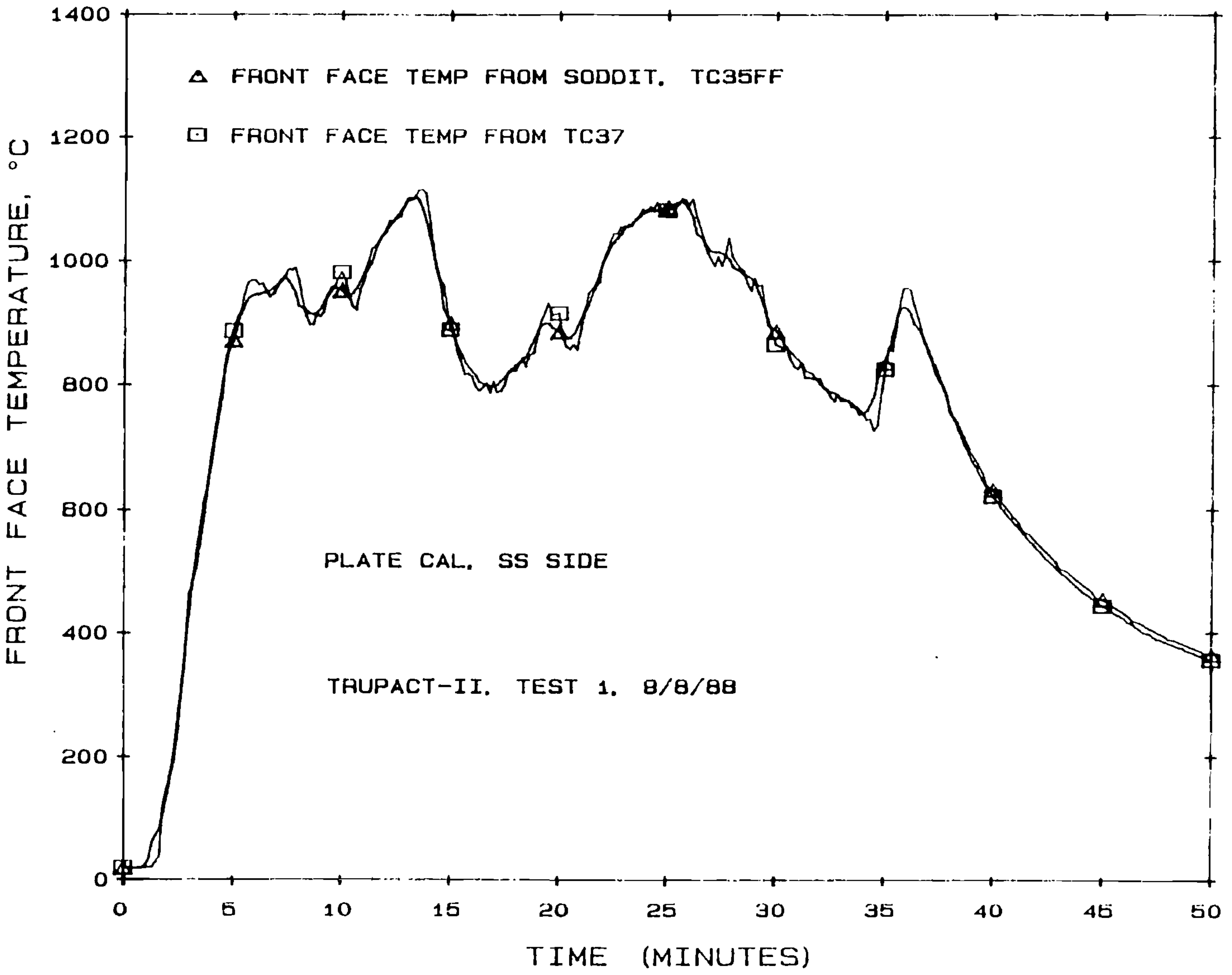

Figure 2.8 Measured Versus Calculated Temperature on the Stainless Steel Side of the Plate Calorimeter (see Figure 2.5)

using 1.59-mm-diameter, inconel-sheathed type K thermocouples on the plate calorimeter and with pencil-type eroding thermocouples (NANMACs) on the cylindrical calorimeter. The inverse heat conduction program SODDIT (Blackwell et al., 1987) was used to estimate the front face temperatures from measured back face thermocouple data. The back face data were also obtained using 1.59-mm-diameter sheathed thermocouples. The plots show quite good agreement between the measured and calculated front face temperatures. In general, both the 1.59-mm-diameter sheathed thermocouples and the NANMAC thermocouples read slightly higher than the calculated front face temperatures. The hemispherical head and sheath of a sheathed thermocouple attached to a flat surface views the surrounding thermal radiation differently than the flat wall and may measure higher temperatures than the surface to which it is attached. In these experiments the sheathed thermocouples on the plate calorimeter show this effect, reading higher than the values calculated from inverse heat conduction. The measured values are also more erratic than the calculated values, suggesting that the thermocouples were reacting faster than the surface. For these reasons, the calculated front face temperatures were used as the "true" temperature in all subsequent calculations. At any location where a back face temperature value is known, a front face temperature can be readily calculated with SODDIT. This has the added benefit of cost savings when a front face temperature estimate is needed.

2.2.2.2 Cold Wall Heat Fluxes

Cold wall heat fluxes are presented as a function of time in Figure 2.9. The cold wall fluxes were calculated by adding to the absorbed heat fluxes a value equal to 85% of the blackbody flux at the front surface temperature. The 85% value comes from the approximate emissivity of the black paint that was applied to both steel plates and of carbon soot generated in the fire. The value for the cold wall flux is close but not identical to the value for the incident radiative flux referred to above. The difference between the two is the reflected flux, which in most cases is only 10 to 15% of the incident value.

Cold wall heat flux values were calculated at 10 different locations on the thick-walled side of the plate calorimeter. Five locations were on the stainless steel side and five on the mild steel side. Those data are shown in Figures 2.9 and A.4, respectively. Location TC33 was situated 30.5 cm from the bottom of the plate, vertically aligned with TC34, as shown in Figure 2.5. TC34 was situated 45.7 cm from TC33, TC38 was 45.7 cm from TC34, TC39 was 61 cm from TC38, and TC40 was 61 cm from TC39, or 61 cm from the top of the plate. Locations TC 41, 42, 46, 47, and 48 were situated at the same positions on the mild steel plate. Figure 2.9 shows that the average cold wall heat flux rises from the lowest station up to the location of TC39, then drops about 10% at the highest location. In addition, there is a large (82%) increase in the average value between the minimum and maximum. A similar trend can be seen for the mild steel side in Figure A.4. The average cold wall flux rises from 77.3 kW/m^2 to 138.0 kW/m^2, an increase of 79%. The average flux also drops at the highest measurement station, but only by about 5%. In Figures 2.10 and A.5 flame temperature plots from the west and north towers show that the location of maximum average flame temperature occurs at about 2.3 m above the pool floor. This agrees with thermal measurement data of Gregory et al. (1987a,b) from the DOT series of large pool fires. Their data locate maximum temperature at 2.2 m, which is close to the 2.3-m measurement from the first TRUPACT-II test. The difference in height is probably only a result of the different setups. The maximum surface temperature and heat flux on both the mild and stainless steel sides of the plate calorimeter occurred about 3.6 m from the pool floor. This is about 1.4 m above where the maximum flame temperature occurred.

The time at which the fire went out is shown to be approximately 36 to 37 min in Figures 2.9 and A.4. The oscillations seen between 36 and 37 min in Figure A.4 are probably not actual heat flux variations but numerical transients initiated by the large temperature changes at the end of the burn. These oscillations are generated in the inverse heat conduction code as the temperature of the mild

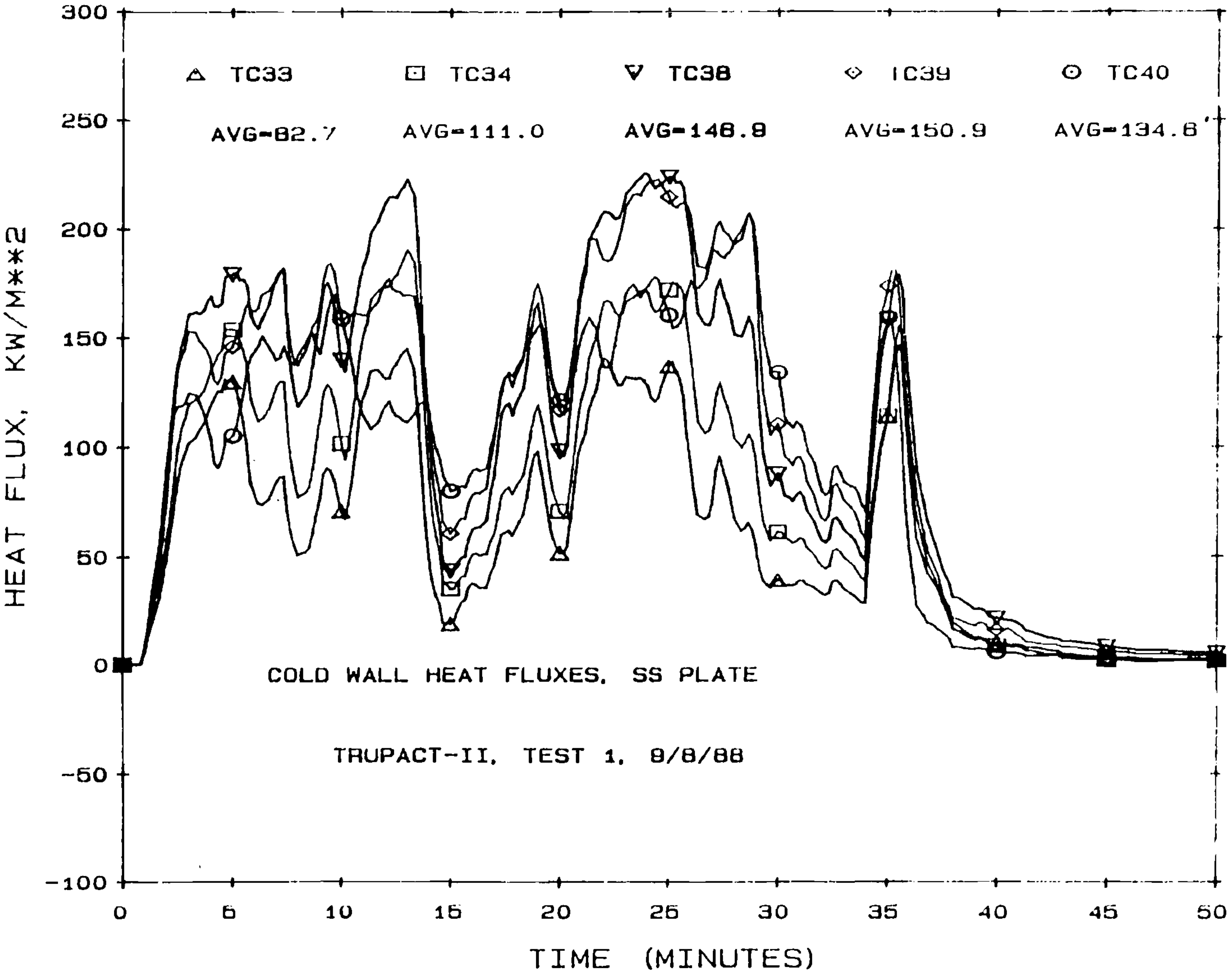

Figure 2.9 Cold Wall Heat Fluxes on the Stainless Steel Side of the Plate Calorimeter (see Figure 2.5)

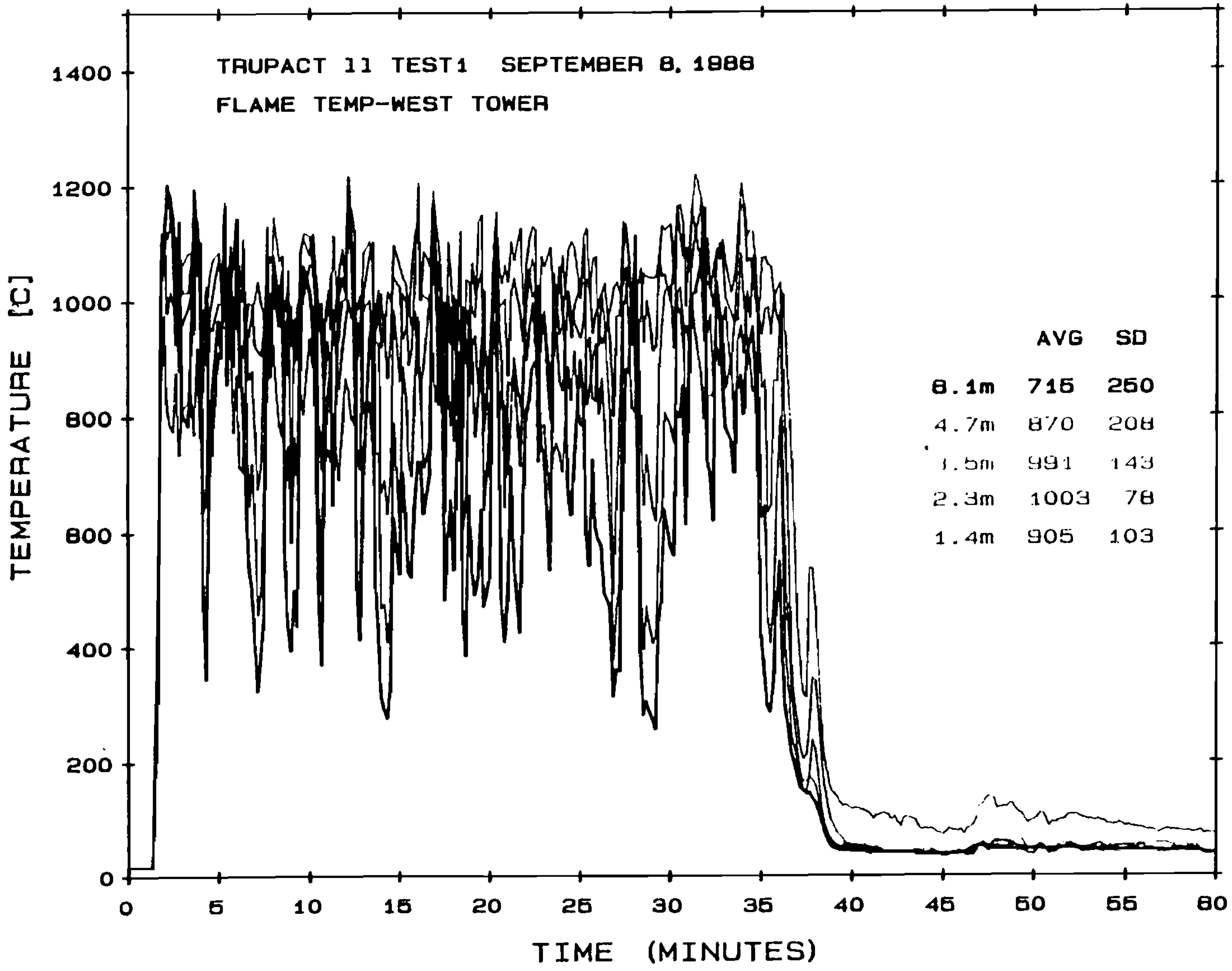

Figure 2.10 Flame Temperatures on the West Tower

steel passes through the Curie point at about 760°C. None of these oscillations occur on the stainless steel side shown in Figure 2.9, because stainless steel has no Curie point at these temperatures.

Figure A.6 plots cold wall heat fluxes on the cylindrical calorimeter. The average flux on the top was 115.2 kW/m^2; on the bottom, 104.6 kW/m^2; and on the west side, 113.0 kW/m^2. These results contradict those from earlier studies (Gregory et al., 1987a,b; Schneider et al., 1988), in which the higher heat flux was seen on the bottom of the 1.4-m-diameter cylindrical calorimeter. For this test, however, a large shipping container, the TRUPACT II, was located at the center of the pool, and the cylindrical calorimeter was located closer to the pool edge. Possible explanations for the observed test-to-test heat flux differences are placement of the calorimeter at the different pool location and varying wind effects.

Figure A.6 shows a sharp dip in the heat flux about 6 to 7 min after the fire went out. As for the plate calorimeter, it is thought that at this time the temperature of the mild steel cylindrical calorimeter dropped through the Curie point, and oscillations were generated from the code. Thus, the sharp downward spike and the equally sharp upward spike between 40 and 45 min on the plot were not actual heat flux variations but a result of the inverse code. Other numerically generated oscillations occurred when the local temperature passed through the Curie point at about 24 to 25 min on the top, at about 26 to 29 min on the bottom, and at about 22 to 25 min on the west side. These oscillations were not as severe as those at the end of the test, at 42 min.

2.2.2.3 Transpiration Radiometers

Transpiration radiometers are heat flux gauges designed to read only the incident radiative component of the heat flux impinging on the surface in question. The "transpiration" gas flow "blows off" the boundary layer, allowing only the radiative flux to be measured (Matthews et al., 1986). Figures 2.11, A.7, and A.8 show transpiration radiometer data from three gauges: two in the plate calorimeter and one in the cylindrical calorimeter. Data were acquired from two other gauges, but at the end of the test their output had such a large offset that the data are not usable. Figure 2.11 shows the data from gauge no. 4, mounted in the mild steel side of the plate calorimeter; Figure A.7 shows data from gauge no. 3, mounted in the stainless steel side; and Figure A.8 shows data from gauge no. 1, at the top of the cylindrical calorimeter. No gauge identified as no. 2 was used for this test. The no. 4 gauge reading started and ended very close to zero (Figure 2.11). The no. 3 gauge reading had an initial negative offset and ended with a larger negative offset (Figure A.7). The no. 1 gauge started at about zero and ended with a large negative offset (Figure A.8). The large ending negative offsets may have resulted from soot covering part of the screen through which the transpiration gas flowed, from changes in gas flow rates, or from changes in gas temperature. Other reasons for the offsets are not yet known.

The average radiative flux to the mild steel side was 105.8 kW/m^2; to the stainless steel side, 93.8 kW/m^2; and to the top of the cylindrical calorimeter, 95.3 kW/m^2 (Figures 2.11, A.7, and A.8). Figure A.7 indicates that the gauge output dropped after about 28 min; Figure 2.11 indicates it did not drop then. Because the gauges are relatively close, one would expect their outputs to be close, but the drop in output after 28 min shown in Figure A.7 would cause the average to drop. This may explain in part why the average output from the stainless steel side is lower than that of the mild steel side. The data from the top of the cylindrical calorimeter, shown in Figure A.8, were adjusted to account for the fact that the transpiration gas flow rate during the test was not the same as the rate used to calibrate the gauge. Because this adjustment was only approximate, the uncertainty is significantly higher for the data shown in Figure A.8 than for the data given in the other two figures. The average flux to the larger cylindrical calorimeter was about 10% below the average flux to the mild steel side of the plate calorimeter.

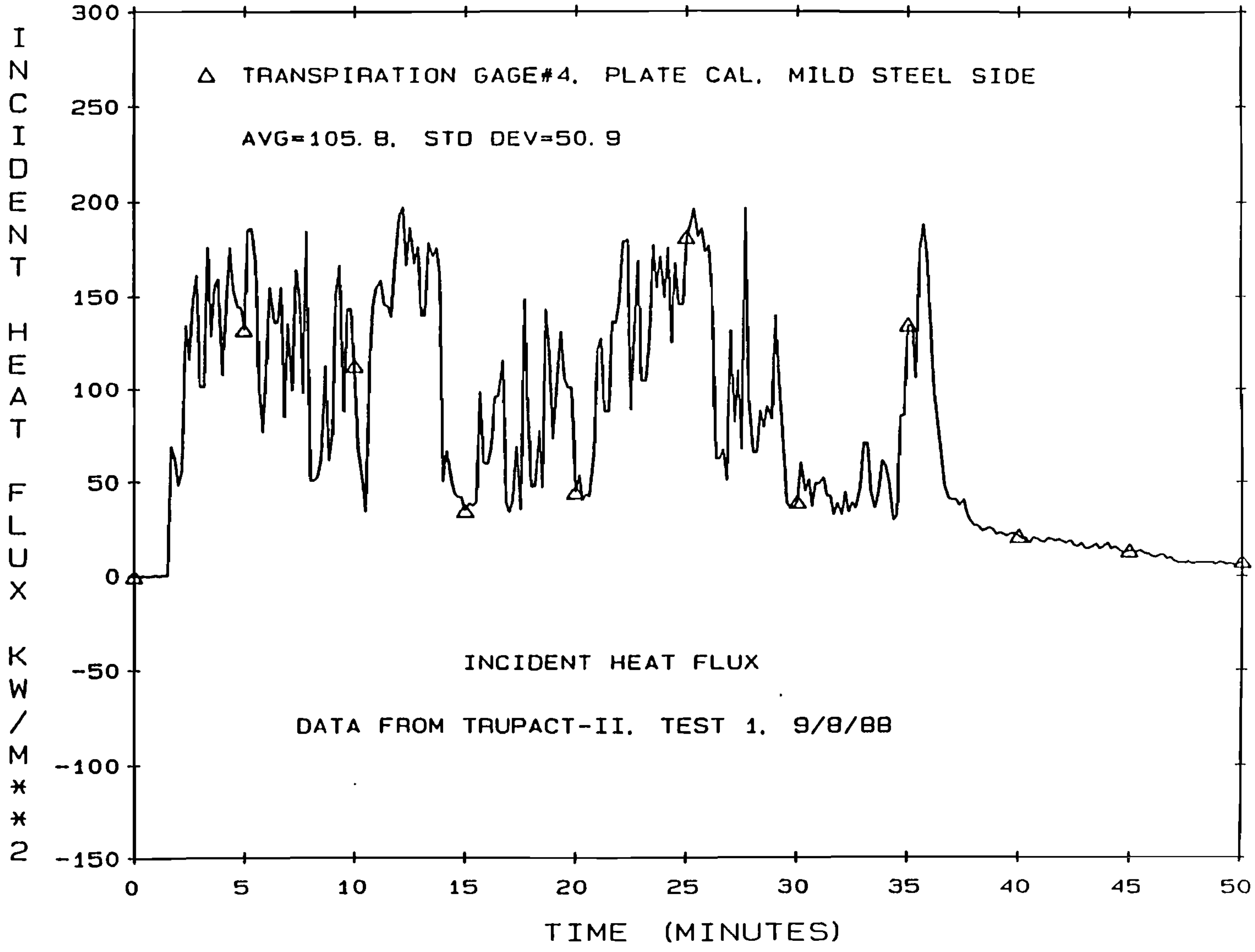

Figure 2.11 Incident Heat Flux on the Mild Steel Side of the Plate Calorimeter (see Figure 2.5)

The data from Figure 2.11 and the flame temperature data can be used to estimate the flame emissivity near the plate calorimeter. If it is assumed that the transpiration radiometer data in Figure 2.11 represent the "true" incident radiative heat flux, the flame emissivity can be adjusted until the average value of $\varepsilon_f \sigma T_f^4$ matches the average value of the transpiration gauge data shown in Figure 2.11. An "average" flame emissivity of 0.82 was the result (the flame temperature data used, T_f, are not shown). The relation $\varepsilon_f = 1 - e^{-\kappa L}$ can be used to compare a calculated value with the measured one. If the optical path length k = 1 m^{-1} (Longenbaugh and Matthews, 1988) and flame emissivity $\varepsilon_f = 0.82$, then the average flame thickness L is 1.7 m, a reasonable value. The value 0.82 for the flame emissivity was used throughout the remaining calculations for estimating the radiative convective partitioning of the heat flux. The 10 CFR 71 regulations specify a flame emissivity of 0.90, and the 0.82 calculated here is within 10% of that value.

Figures 2.12 and A.9 show the radiative heat flux calculated if $\varepsilon_f = 0.82$ in the relation $q_{ir} = \varepsilon_f \sigma T_f^4$. These plots can be compared with the corresponding transpiration gauge outputs shown in Figures 2.11 and A.8. Figures 2.11 and 2.12 compare quite well, as do their averages, because the emissivity was based on the underlying temperature data as discussed in the previous paragraph. The signatures (transient behavior) also agree quite well. The averages for the top of the calorimeter, as shown in Figures A.8 and A.9, do not agree, possibly because the flame emissivity on the top of the cylinder calorimeter is not 0.82 or the adjustment made for the different transpiration gas flow causes a larger error. However, in both cases the signatures on the corresponding plots agree quite well.

When Figures 2.11 and A.7 are compared with Figures 2.12 and A.9, it can be seen that the transpiration radiometers respond faster than the 1.59-mm-diameter sheathed thermocouples. This is expected, because the screen-sensing element on the transpiration gauge is less than 0.25 mm thick and so should respond faster than a 1.59-mm-diameter sheathed thermocouple.

Once a value for flame emissivity is established, the total, radiative, and convective contributions can be estimated if the surface temperature and emissivity are known. The surface emissivity was known because the surface was painted with a high-absorptivity paint (emissivity of about 0.85) called Pyromark Black (Longenbaugh and Matthews, 1988). The surface temperature as a function of time was known from the inverse calculations described above. A heat steady-state balance on the front surface gives the following relation:

$$q_{net} = q_{ir} - q_{er} + q_c - q_{refl} \tag{2.2}$$

where

q_{net} = net absorbed heat flux,
q_{ir} = incident radiant heat flux,
q_{er} = emitted radiative flux from the surface,
q_c = convective flux, and
q_{refl} = reflected radiative flux.

The net flux q_{net} is obtained from back face temperature measurements and SODDIT.

As indicated above, the incident radiative flux can be given by the relation

$$q_{ir} = \varepsilon_f \sigma T_f^4 \tag{2.3}$$

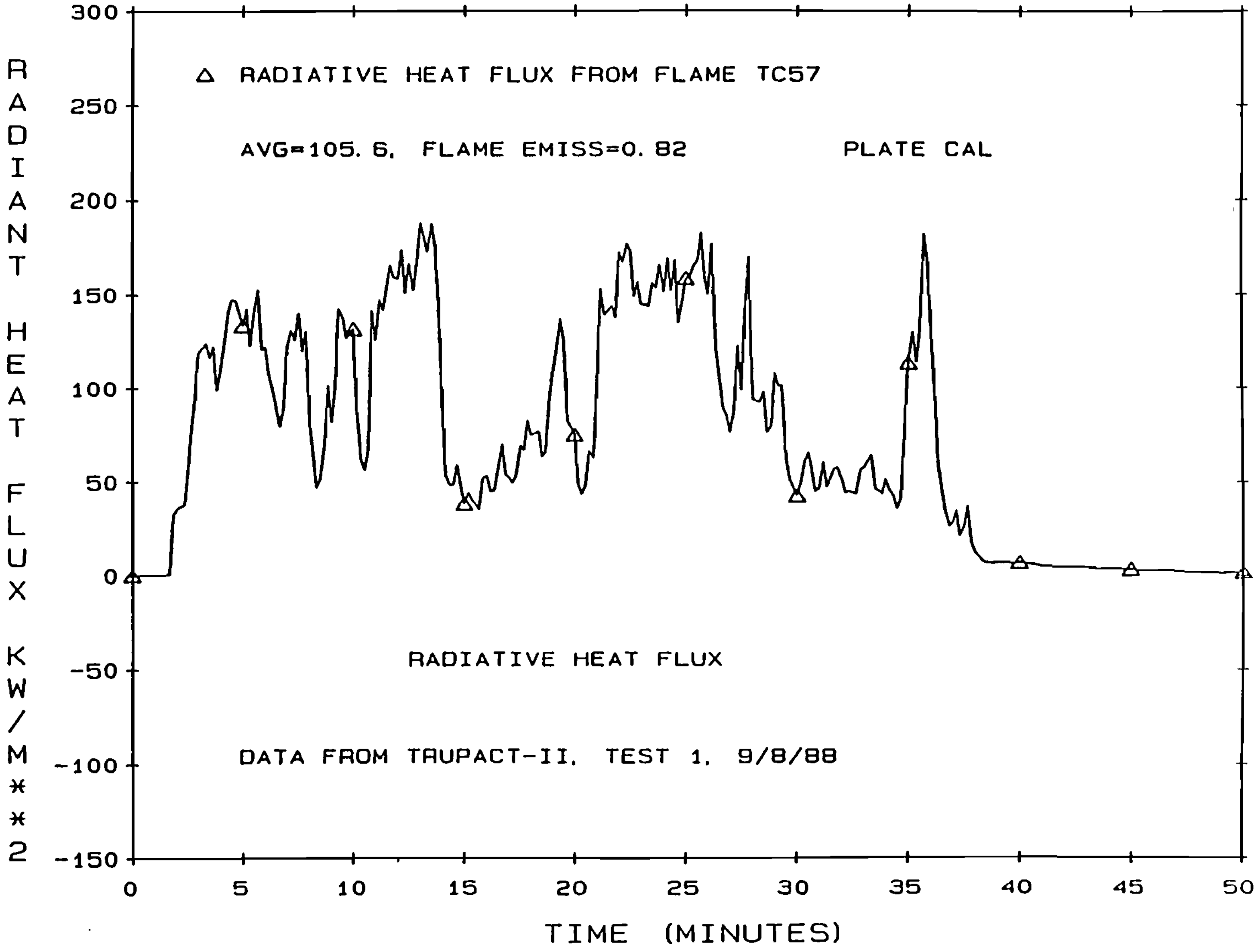

Figure 2.12 Radiative Heat Flux for the Plate Calorimeter (see Figure 2.5 for location of TC57)

where ε_f = flame emissivity and T_f = flame temperature. Substituting into equation (2.2) yields

$$q_{\text{net}} = \sigma\varepsilon_f T_f^4 - \sigma\varepsilon_s T_s^4 \; h_s(T_f - T_s) - (1 - \varepsilon_s)\sigma\varepsilon_f T_f^4 \tag{2.4}$$

where s refers to surface conditions. Equation (2.4) can be rearranged to solve for the convective component q_c:

$$q_c = h_s(T_f - T_s) = q_{\text{net}} + \sigma\varepsilon_s T_s^4 - \sigma\varepsilon_s\varepsilon_f T_f^4 \tag{2.5}$$

Finally, the total heat flux incident on the surface as the sum of the radiative and convective parts can be obtained:

$$\begin{aligned} q_t &= q_{\text{ir}} + q_c = q_{\text{net}} + q_{\text{er}} + q_{\text{refl}} \\ &= q_{\text{net}} + \sigma\varepsilon_s T_s^4 + (1 - \varepsilon_s)\sigma\varepsilon_f T_f^4 \end{aligned} \tag{2.6}$$

The process begins with calculating the net heat flux, q_{net}, from back face temperature measurements and SODDIT. Next the incident radiative heat flux is calculated from equation (2.3) and the appropriate flame temperature. Then equations (2.5) and (2.6) can be used to estimate the convective and total contributions of the heat flux. Although the transpiration gauge data for the incident radiant heat flux, q_{ir}, could be used, they were not because the time base of the transpiration gauge data and that of the q_{net} and T_s data are not the same.

With the above scheme the total, radiative, and convective parts of the heat flux were calculated for the mild and stainless steel sides of the plate calorimeter and for the top of the 1.4-m-diameter cylindrical calorimeter. Similar data are presented in Nakos and Keltner (1989). Figures 2.13, A.10, and A.11 show multiplots of those calculations. Figure 2.13 shows the data from the mild steel side; Figure A.10, from the stainless steel side; and Figure A.11, from the top of the cylindrical calorimeter. The negative convective heat fluxes shown in the figures were caused by strong wind gusts that moved the fire off the calorimeter resulting in heat transfer from the calorimeter to the cooler air. As can be seen in all the plots, the radiative part is by far the largest contributor to the total heat flux. The average convective part varies from only 11.5 to 17.3% of the total flux. However, close examination of the radiative and convective parts of the plots during the first 2 to 3 min of the test shows that the convective part can be a significant fraction, perhaps up to 50% of the total. This kind of behavior was also seen by Cooper and Stroup (1987) in ceiling fires and by Russell for experiments involving cylinders immersed in large aviation fuel fires (1970).

2.3 Analysis of the DOT/NRC Environmental Comparison Test Series

A series of tests was conducted to compare the 10 CFR 71 and 49 CFR 179 regulatory environments. The tests took place at the Radiant Heat Test Facility and the Small Wind Shielded (SWISH) site at the Lurance Canyon Burn Site.

The heat flux of the radiant environments were chosen to match the temperatures of the 10 CFR 71 (800°C) and the 49 CFR 179 (870°C) regulatory fire environments. The 10 CFR 71 regulation actually specifies a heat flux in the environment equal to or greater than the radiant flux from a source at 800°C with an emittance of 0.9. The surface absorptance must be either the value the package would be expected to have or 0.8, whichever is greater. These parameters lead to a minimum acceptable heat flux of 55.5 kW/m^2 for container wall temperatures near 20°C. The 49 CFR 179 regulation specifies a temperature of 870°C in the environment but requires an average heat flux of 30 to 35 kW/m^2 with wall temperatures varying from near 20°C to 427°C

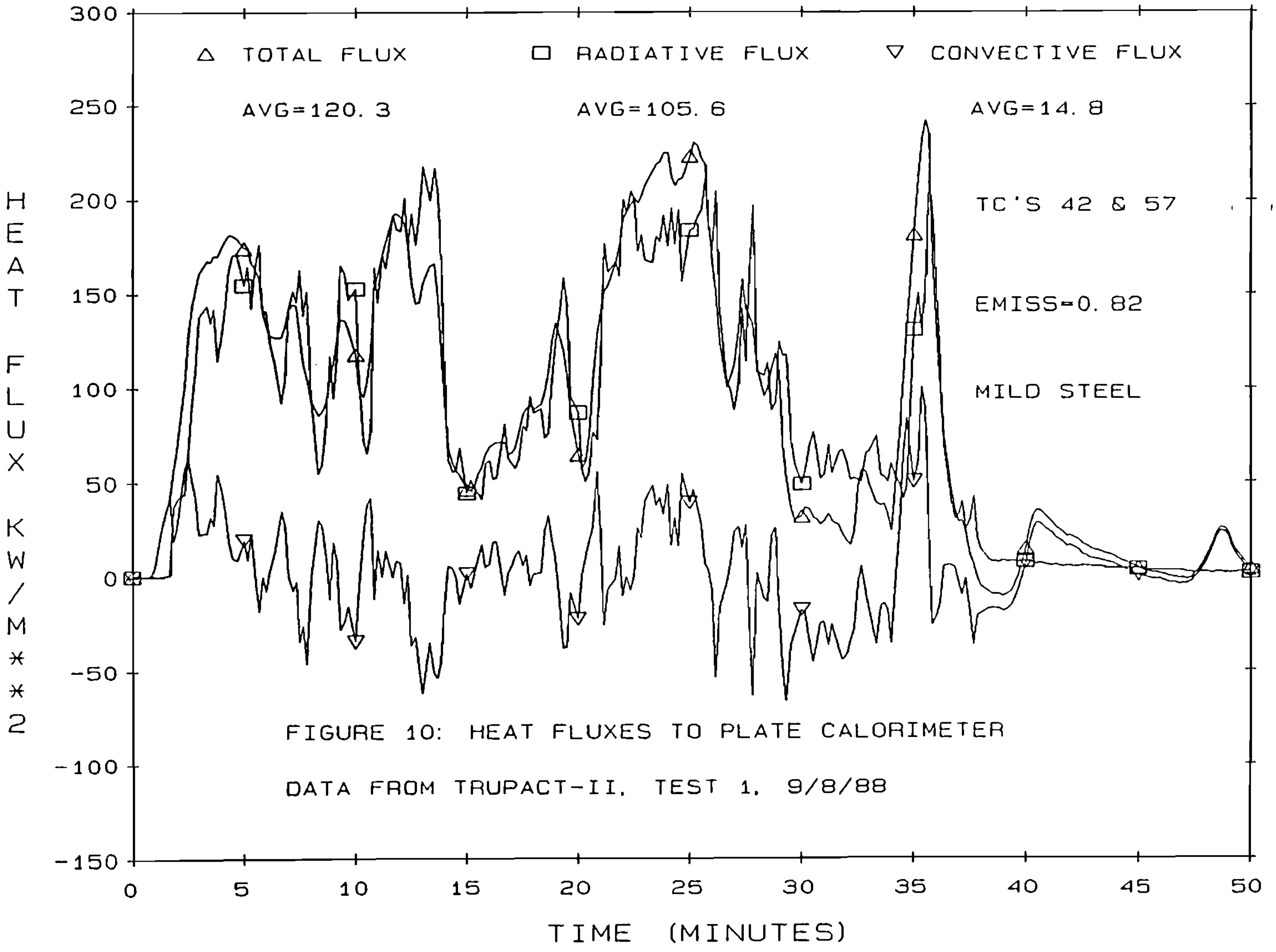

Figure 2.13 Heat Fluxes to the Mild Steel Side of the Plate Calorimeter (see Figure 2.5)

(Keltner et al., 1990). Times specified in the two regulations are also different. The 10 CFR 71 fire duration requirement is 30 min, while the 49 CFR 179 thermal protection system fire test requirement is 100 min. Other differences involve basic differences in test philosophy. For 10 CFR 71, the entire container must be considered, while for 49 CFR 179, a small section of the thermal protection system is typically tested. The heat source considered for 10 CFR 71 is a fully engulfing pool of fire, while for 49 CFR 179 a large, calibrated torch usually simulates the pool fire.

The preceding paragraph may appear to suggest a heat flux ratio of two or more between the 10 CFR 71 and 49 CFR 179 fire environments, but the comparison is complicated by the issue of object response. For example, assuming they are made from similar materials, a small object exposed to a fire heats much more quickly than a massive object. This means that surface temperatures of a small object approach the fire temperature more quickly than for a massive object. Since heat transfer to an object decreases as surface temperatures increase, the smaller object may only absorb slightly more energy during a 100-min fire than it would during a 30-min fire. For massive objects, and especially objects where a change of material phase may occur such as railroad tank cars, surfaces temperatures increase more slowly, and the heat absorbed during a 100-min fire may be significantly larger than for a 30-min fire. However, because the smaller object may attain higher temperatures during the course of the fire, and since material damage is more typically related to high temperatures or high temperature gradients than heat flux, the smaller object may incur more internal damage than the larger object.

The comparison between 10 CFR 71 and 49 CFR 179 fire test environments is further complicated by issues related to the mode of transportation. The 10 CFR 71 regulations for radioactive materials are intended to cover a wide range of transportation such as truck, rail, and waterborne shipments, while 49 CFR 179 (regulations) cover shipments in railroad equipment with thermal protection systems. Furthermore, 10 CFR 71 is intended to prevent release of radioactive package contents for which there are relatively low driving potential pressure, explosive, and/or flammability concerns. In contrast, 49 CFR 179 is intended to assure no release of car contents before 100 min and a controlled release of railcar contents via relief valves thereafter.

With rail shipments, larger quantities of flammable materials are potentially available in the car in question as well as adjacent tank cars than might occur with truck transportation of radioactive materials. Justification of the 30-min test fire duration required by 10 CFR 71 and the 100-min test fire duration cited in 49 CFR 179 lies beyond the scope of this report, but previous studies (Clarke et al., 1974) indicate that these durations exceed the great majority of anticipated fire durations. Clarke et al. demonstrate that for "exclusive use" truck shipments, i.e., shipments with no other flammable lading on the same truck, the 30-min duration exceeds most anticipated durations. Because FRA requires buffer cars containing nonhazardous material on either side of a cask car, the 30-min duration is more appropriate than might be considered based on an analysis of potential fire durations without the use of buffer cars. Similarly, Clarke et al. show that the 30-min duration covers more than half the events and the 100-min test fire duration exceeds most fire durations for accidents involving railcars with flammable material lading. The thermal boundary conditions for fully engulfing fires reported herein are applicable regardless of fire duration.

2.3.1 Description of the Test Units

One of the test units was designed to be thermally massive. This calorimeter will be referred to as the thick wall unit (see Figures 2.14 and 2.15). The thick wall unit consists of a 0.91-m-tall, mild steel cylinder with an outer diameter of 0.46 m. Its wall thickness is 3.18 cm, and the center cavity is filled with ceramic fiber blanket insulation. It is instrumented with 42 inconel-sheathed type K thermocouples. Thermocouple no. 1, situated on the back face of the cylinder halfway from either end, will be used for analysis.

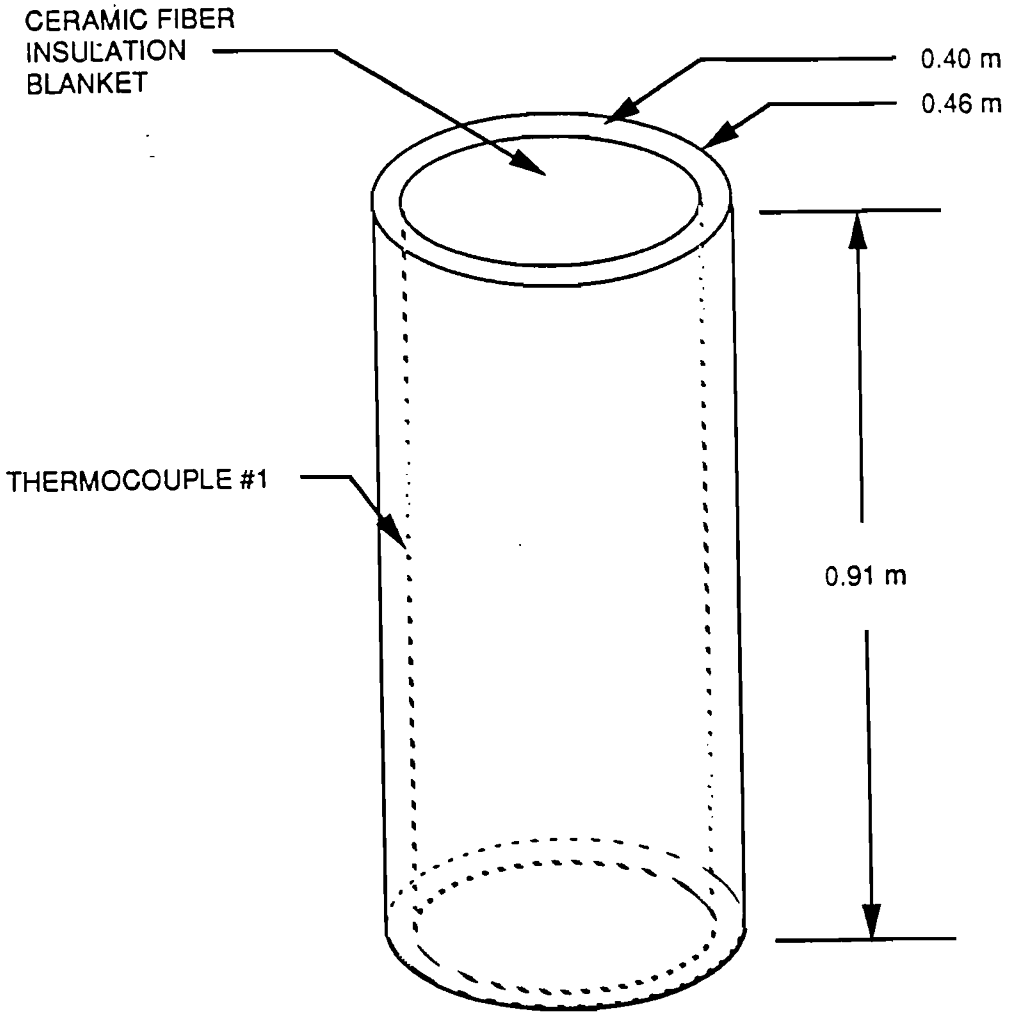

Figure 2.14 Thick Wall Unit

The other unit, referred to as the thin wall unit, was designed to be thermally nonmassive by the positioning of a thin radiation shield and air gap around a cylinder (see Figures 2.16 and 2.17). The inner cylinder is 0.91 m tall, with a 0.3-m outer diameter and 4.76-cm wall thickness. The radiation shield has the same outer physical dimensions as the thick wall unit. The thin wall unit is made of 304 stainless steel, and the inner cavity of the inner cylinder is filled with ceramic fiber blanket insulation. The thin wall unit is instrumented with 28 inconel-sheathed type K thermocouples. Thermocouple no. 13, which is situated on the back face of the radiation shield halfway from either end, will be used for analysis.

All noninsulated surfaces of both units were painted with the high-temperature, high-emissivity black paint Pyromark Black. The total heat capacity of the thin wall calorimeter was 86% of that of the thick wall calorimeter.

2.3.2 Radiant Heat Simulated Fire Tests

Simulated fire tests are conducted at the Radiant Heat Test Facility by exposing a test unit to a stainless steel heating shroud. Banks of quartz lamps are used to heat the shroud from ambient temperature to the specified "fire temperature" in less than 1.5 min. The shroud is painted with Pyromark 2500; the size and shape of the shroud can be tailored to the test unit. The shroud is

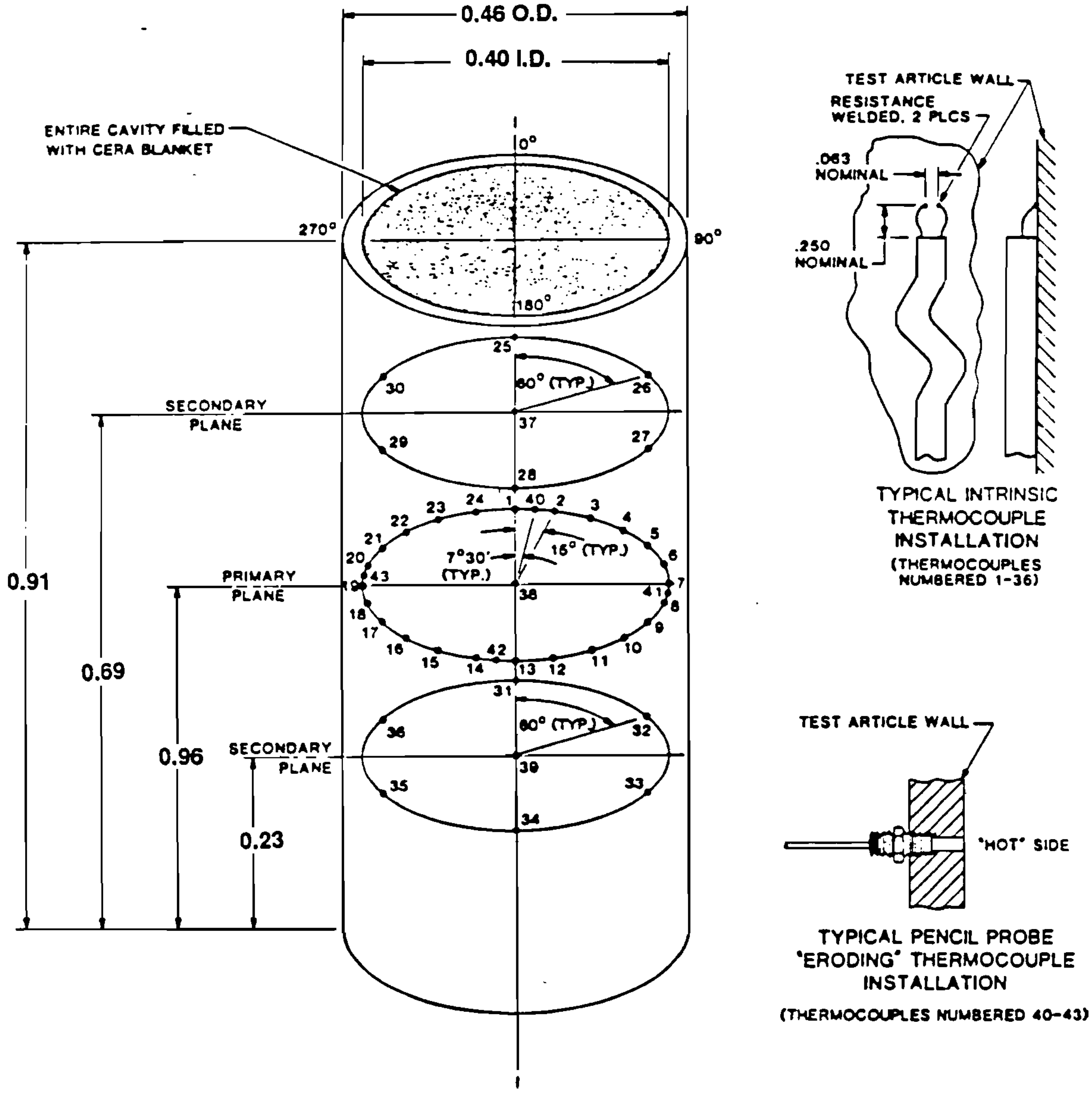

Figure 2.15 Thick Wall Unit Measurement Locations

instrumented with ungrounded junction, inconel-sheathed type K thermocouples. Microprocessor-based controllers with temperature feedback are used to adjust the temperature profile of the shroud.

The test units were centered (one per test) inside a 0.61-m-diameter, 1.2-m-tall circular cylinder heating shroud. Two tests were conducted on each calorimeter: the first at 800°C for 30 min and the second at 870°C for 100 min. The shroud was brought from ambient to the specified temperature in approximately 1.5 min and held at that temperature for the specified regulatory time.

The heat flux produced by a simulated fire test of this type is almost entirely radiative. The radiant heating test provides the heat flux vs. wall temperature profile specified by 10 CFR 71. The temperature required by 49 CFR 179 is provided, but the resulting initial and cold wall heat flux is approximately 85 to 90 kW/m^2, compared to the average 30 to 35 kW/m^2 required to meet 49 CFR 179 calibration specifications.

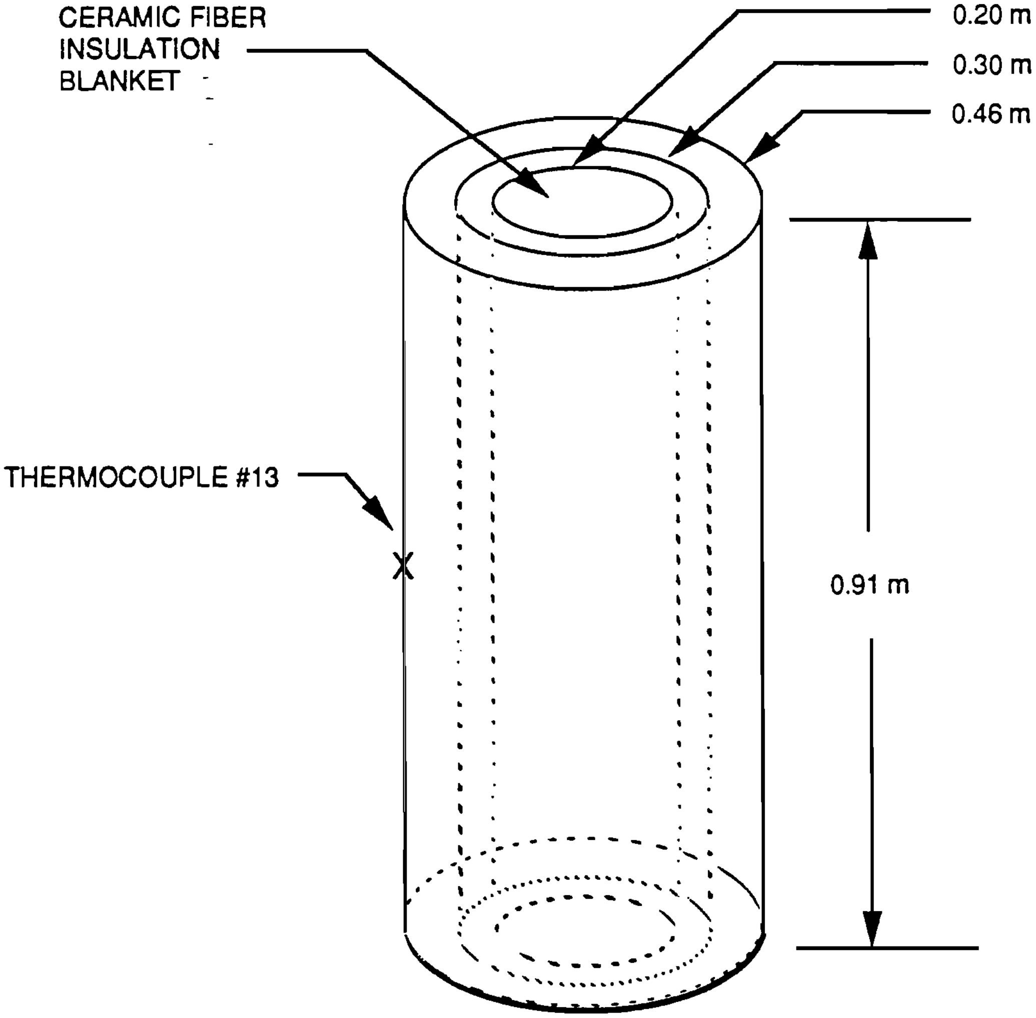

Figure 2.16 Thin Wall Unit

2.3.3 Small Wind Shielded Facility Tests

The fire tests, with a separate test for each unit, were performed in the SWISH facility. The general setup is shown in Figures 2.18 and 2.19.

The test unit was placed on a stand in the center of the 1.8-m-diameter burn pan. The ends of each unit were insulated and the axis of the test unit oriented vertically. The pan was filled with water and enough JP-4 jet fuel to produce a 100-min burn time. "Flame temperatures" were recorded with thermocouples extending from four towers placed around the unit. These thermocouples were placed 0.08 m from the test unit. (The SWISH facility and the test setup are described in greater detail by Kent [1988].)

The airflow rate to the fire can be used to control its temperature. For these tests, the desired temperature was 870°C in order to compare the radiant test environment and the 49 CFR 179 regulatory environment. The thick wall calorimeter test required approximately 40% more airflow to maintain a temperature near 870°C.

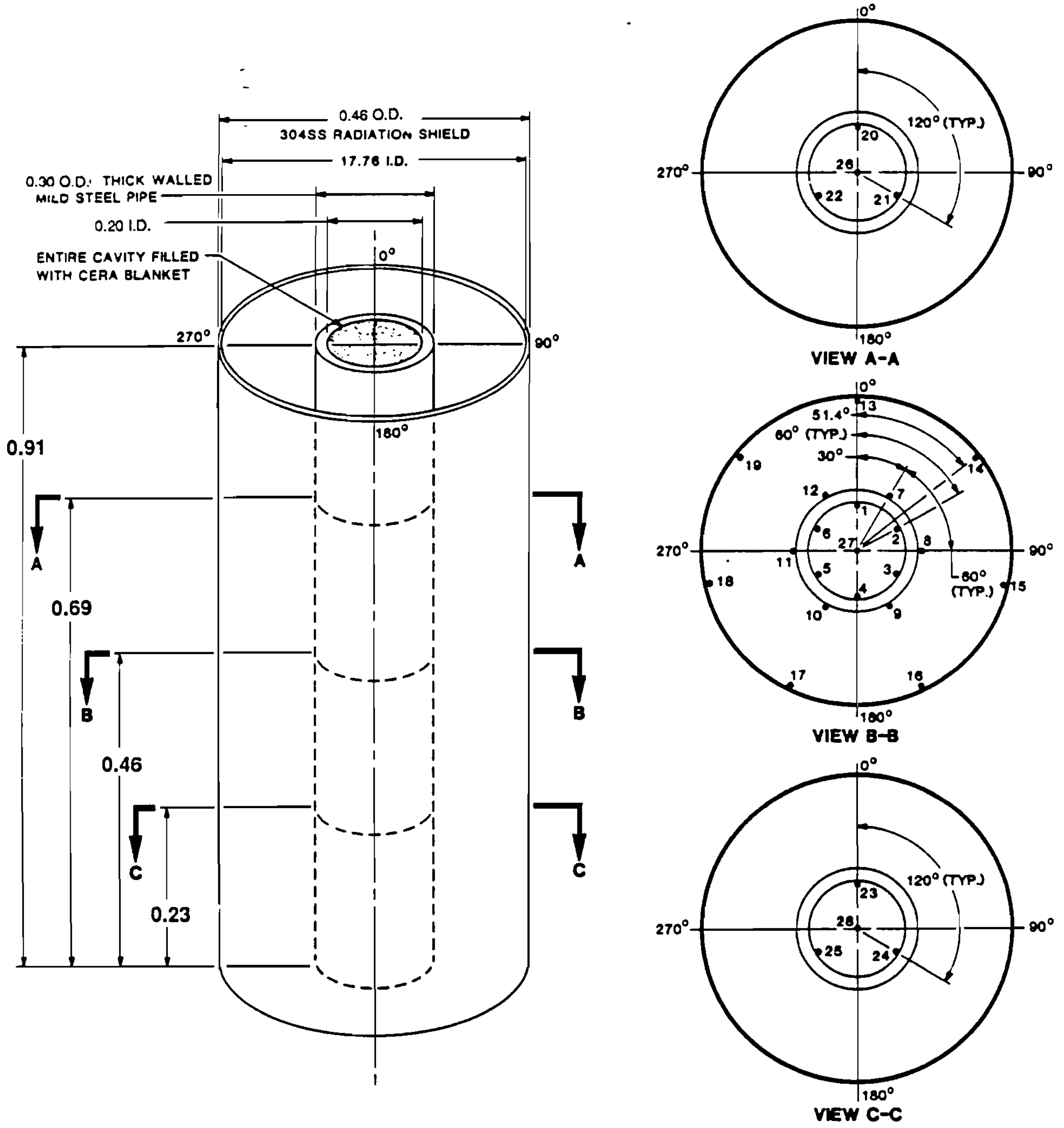

Figure 2.17 Thin Wall Unit Measurement Locations

2.3.4 Environmental Temperatures

Temperature-time histories for the center-plane radiant-heating-shroud thermocouple; the flame thermocouple from the west tower, location B; and the thermocouple used for analysis are superimposed in Figure 2.20 for the thick wall test. For the thick wall SWISH test, the average flame temperature from this thermocouple was 880°C. The average temperature from that location for the thin wall fire test was 874°C, reported by Kent (1988). The environmental temperature from the fire test is similar to that from the 870°C radiant heating test.

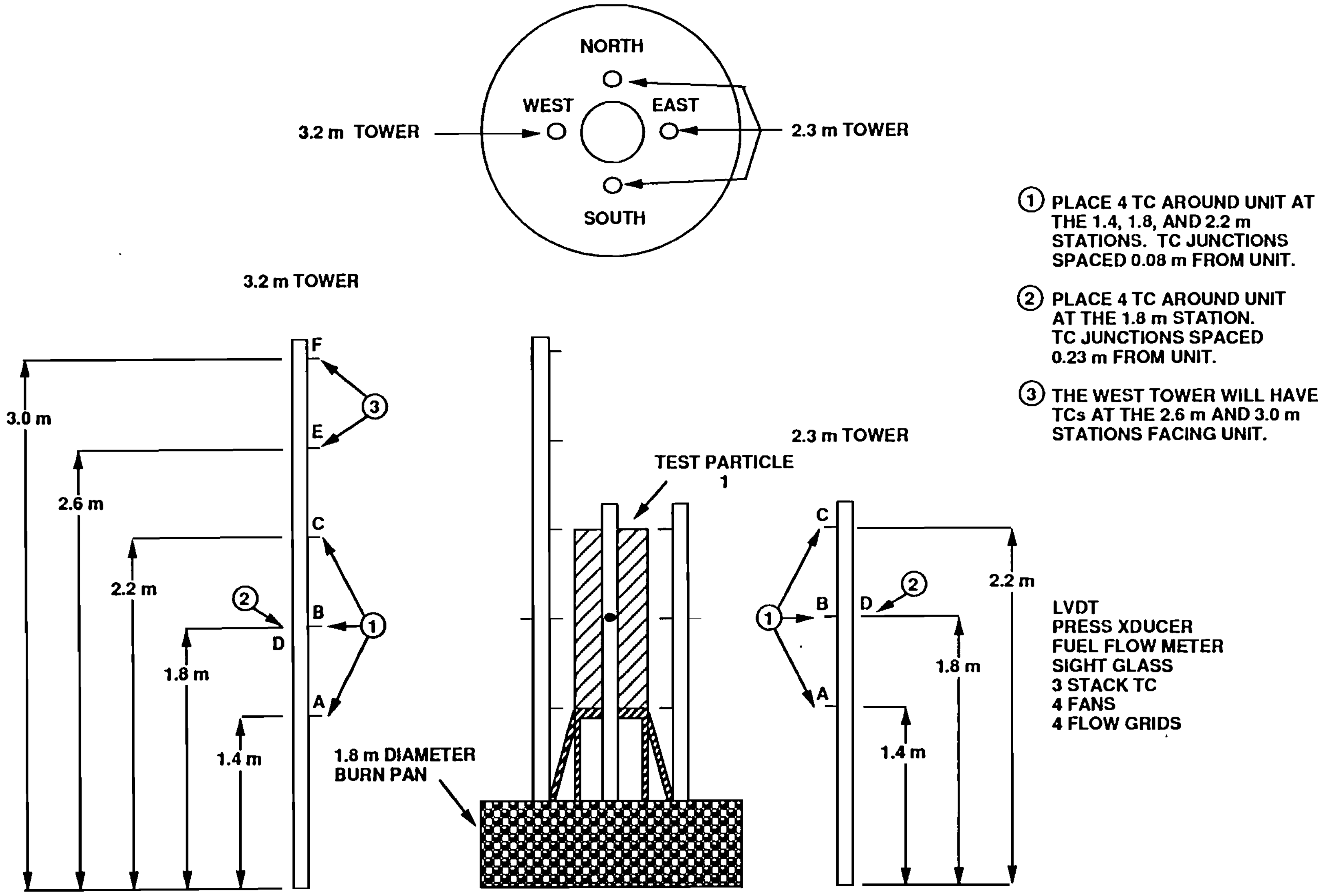

① PLACE 4 TC AROUND UNIT AT THE 1.4, 1.8, AND 2.2 m STATIONS. TC JUNCTIONS SPACED 0.08 m FROM UNIT.

② PLACE 4 TC AROUND UNIT AT THE 1.8 m STATION. TC JUNCTIONS SPACED 0.23 m FROM UNIT.

③ THE WEST TOWER WILL HAVE TCs AT THE 2.6 m AND 3.0 m STATIONS FACING UNIT.

LVDT
PRESS XDUCER
FUEL FLOW METER
SIGHT GLASS
3 STACK TC
4 FANS
4 FLOW GRIDS

Figure 2.18 Small Wind Shielded Facility Test Setup

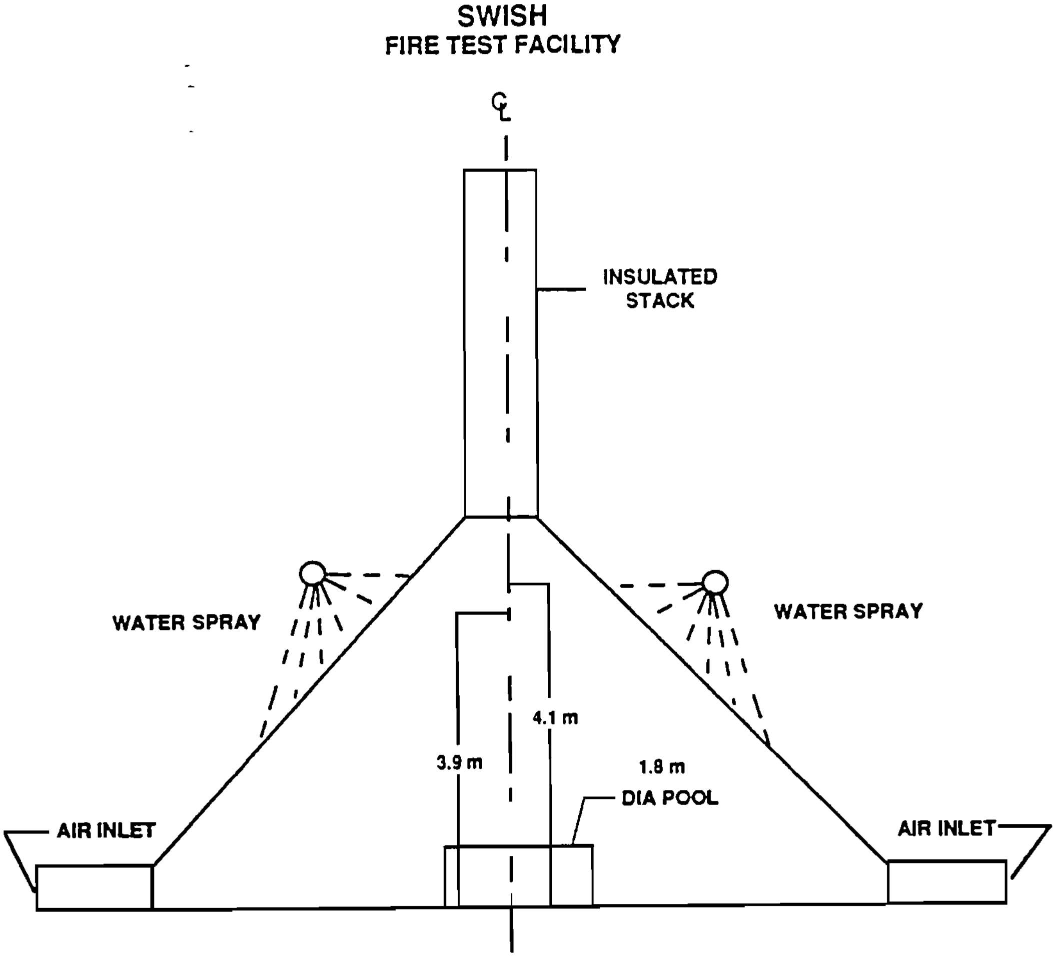

Figure 2.19 Small Wind Shielded Facility

2.3.5 Back Face Temperatures

Data from the thick wall unit, thermocouple no. 1, for each of the three tests are shown in Figure 2.21. At very early times (the first 3 min) data from the SWISH test are similar to those from the 870°C radiant heat test. At later times the data from the SWISH test show cooler temperatures than those from the 870°C radiant heat test. At approximately 30 min the SWISH data are similar to those from the 800°C radiant heat test. The inflection point in the data from the 870°C radiant heat test corresponds to the Curie point transformation of the mild steel.

Temperatures of the radiation shield for the thin wall tests are shown in Figure 2.22. These data are from the thin wall unit, thermocouple no. 13. During the 870°C radiant heat test, the shield came up rapidly to approximately 735°C and heated slowly throughout the remainder of the test to 850°C. The shield's temperature followed the same pattern for the 800°C radiant heat test, with the "knee" occurring at approximately 640°C and the final temperature reaching 692°C. The profile for the SWISH test was a little different. The shield heated rapidly to 704°C, then cooled to 670°C before heating to 687°C at the end of the test.

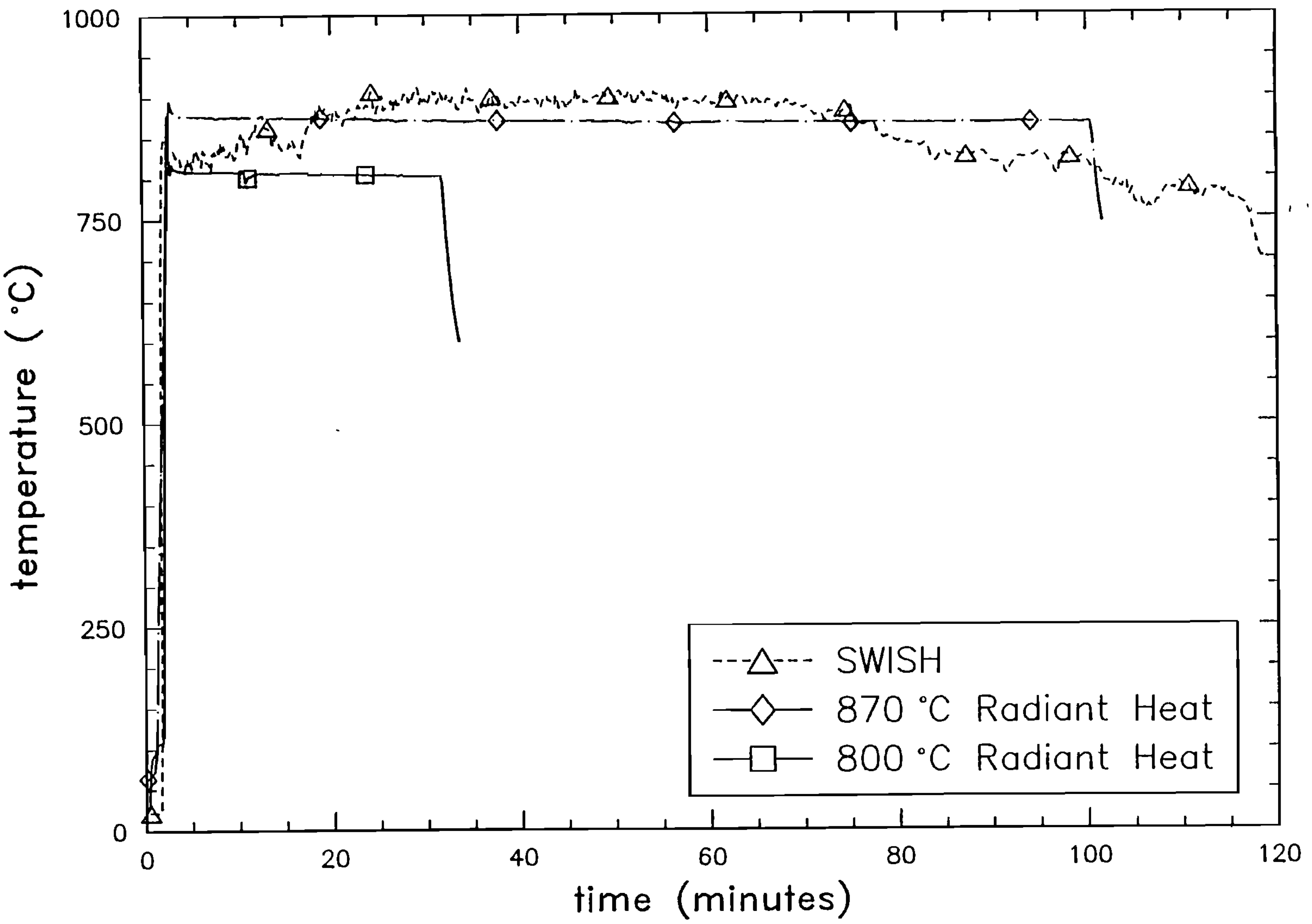

Figure 2.20 Environmental Temperatures for the Thick Wall Tests

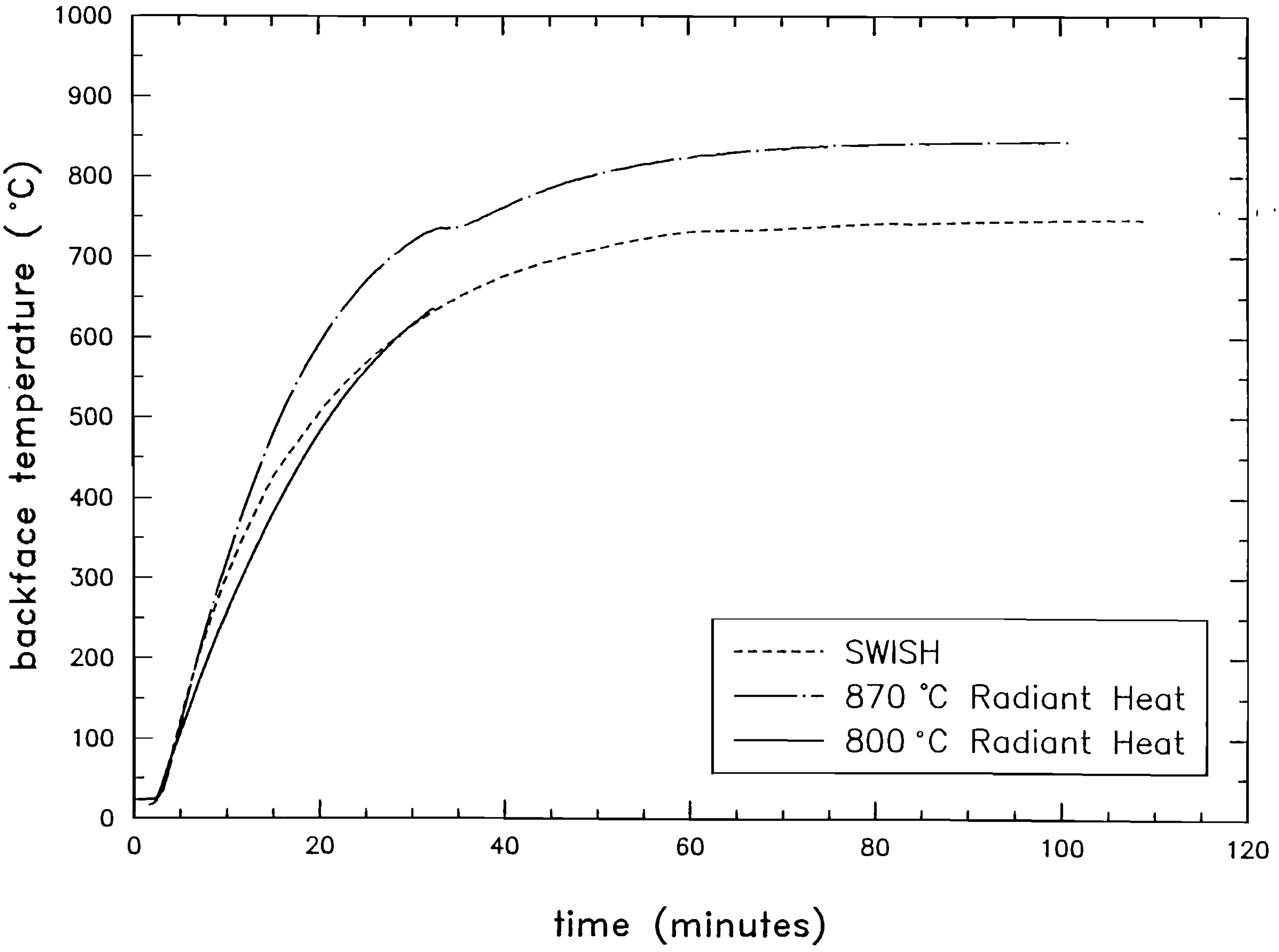

Figure 2.21 Back Face Temperatures for the Thick Wall Tests

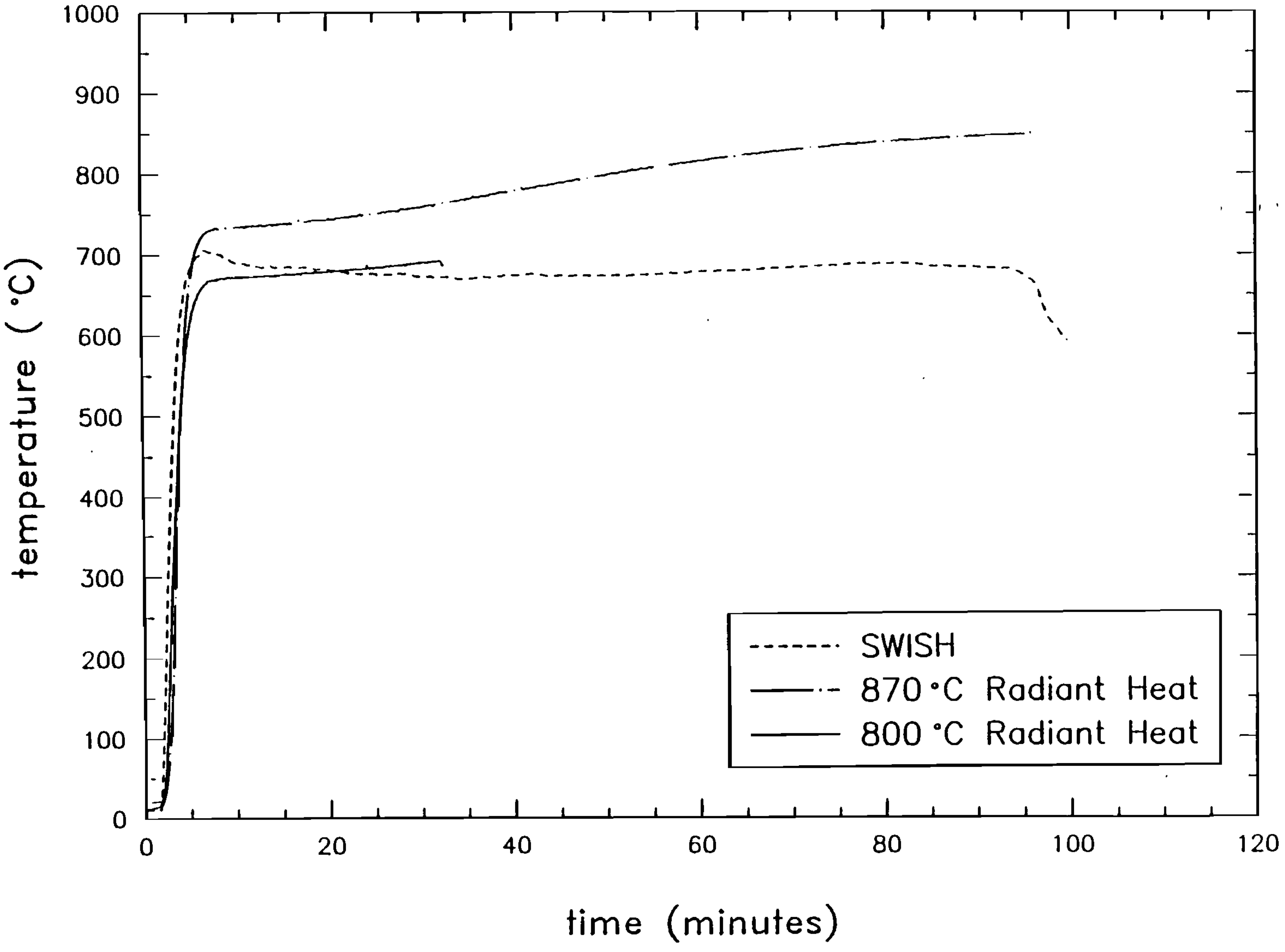

Figure 2.22 Shield Temperature Versus Time for the Thin Wall Tests

2.3.6 Surface Temperatures

The back face temperature data can be used with the one-dimensional inverse conduction code SODDIT (Blackwell et al., 1987) to estimate surface temperatures and heat fluxes absorbed at the surface. Estimates of surface temperatures for the SWISH tests are shown in Figure 2.23. For greater resolution Figure 2.24 shows the first 30 min of each test. As expected, the thick wall heats slowly compared to the thin wall unit. The thermal mass of the radiation shield of the thin wall is small, and the resistance to heat flow from the shield to the inner cylinder is large. Even though the thick wall calorimeter had a larger heat capacity than the thin wall unit, the thick wall eventually becomes hotter than the thin wall because the resistance to heat flow is less. The thick wall calorimeter absorbed more energy than the thin wall calorimeter during the fire tests. The response of the thin wall unit illustrates the usefulness of radiation shields in thermal protection systems for transportation applications.

2.3.7 Hot Wall Heat Fluxes

Hot wall fluxes for the thick wall unit are shown plotted against time in Figure 2.25 and against surface temperature in Figure 2.26. The peak fluxes for the SWISH test and the 870°C radiant heat test are close to the same. The flux from the SWISH test drops much more rapidly, actually below that of the 800°C radiant heat test at a surface temperature of about 425°C. The drop in flux from the 870°C radiant heat test at 33 min and 750°C is caused by the failure of SODDIT to handle the rapidly varying specific heat near the Curie point transformation, making the calculations in this temperature region inaccurate.

The hot wall heat fluxes for the thin wall tests are shown plotted against time in Figure 2.27 and against surface temperature in Figure 2.28. Although the curves for the 870°C radiant heat test and the SWISH test appear similar, the heat flux from the SWISH test results in a fairly stable surface temperature close to 700°C at the end of the test, whereas the temperature at the end of the 870°C radiant heat test was 850°C and increasing gradually. This demonstrates the importance of fire size in the real world. Few long duration fires are large enough to produce either the 10 CFR 71 or 49 CFR 179 regulatory test heat flux and temperature response.

The peak fluxes for the thick wall unit are approximately 50% greater than those for the thin wall, because the thin wall heats much more rapidly. The thin wall is reradiating a significant portion of the flux by the time the environment (the heating shroud or flame temperatures) has reached the test conditions. The shield of the thin wall unit is expected to act as a radiation shield. An ideal radiation shield would reduce the heat flux by approximately one half.

For the SWISH test, the 1.8-m-diameter pool is smaller than the 9-m x 18-m pools reported in Section 2.2. In SWISH, the flame thickness was approximately 0.7 m and therefore not "optically thick." The emittance of the flames can be estimated by

$$\varepsilon_f = 1 - e^{-\kappa L} \tag{2.7}$$

where

κ = the extinction coefficient; a nominal value of 1 m^{-1} is used for JP-4 fires (Longenbaugh and Matthews, 1988), and
L = flame thickness.

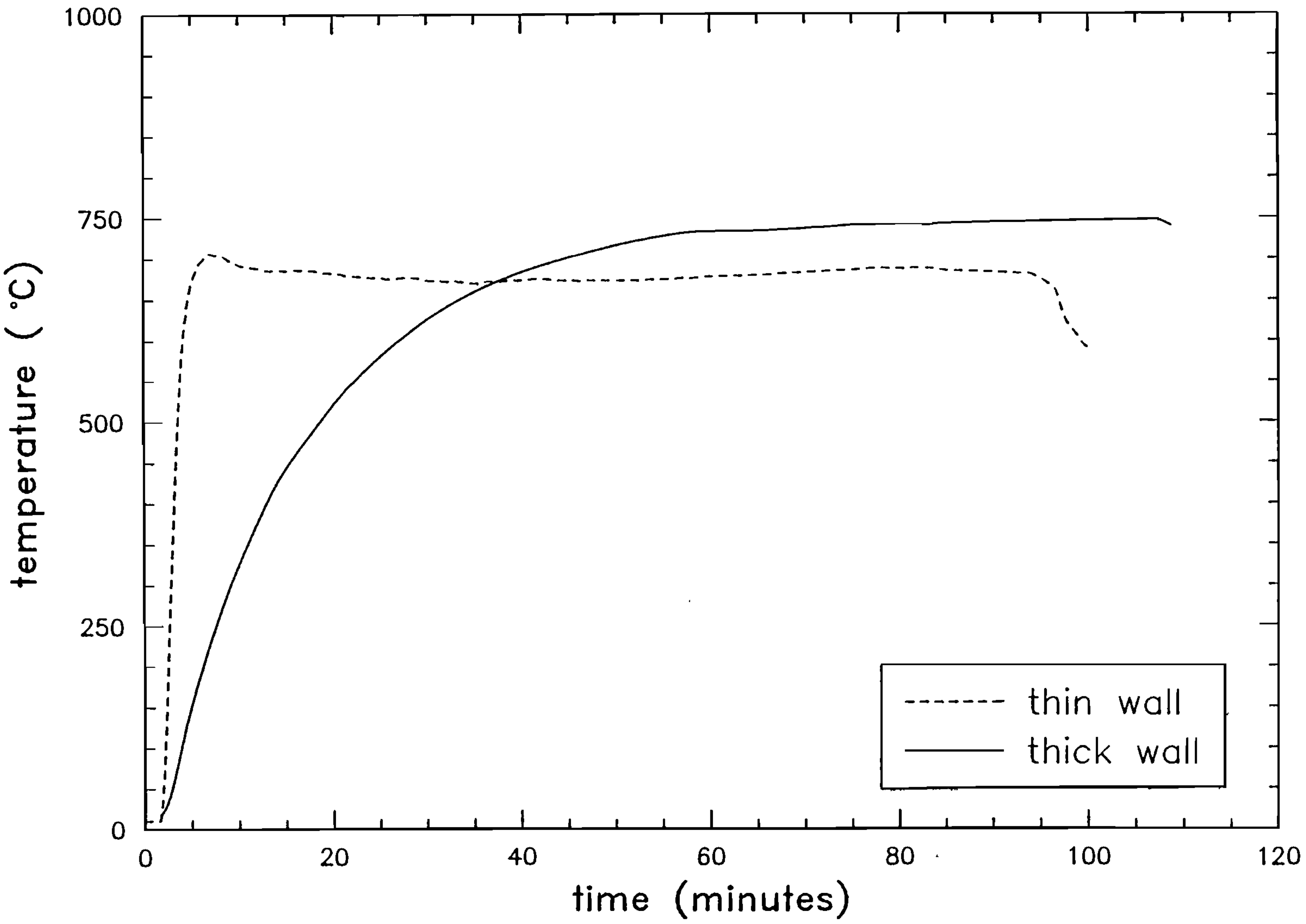

Figure 2.23 Surface Temperature Versus Time for the Small Wind Shielded Facility Tests

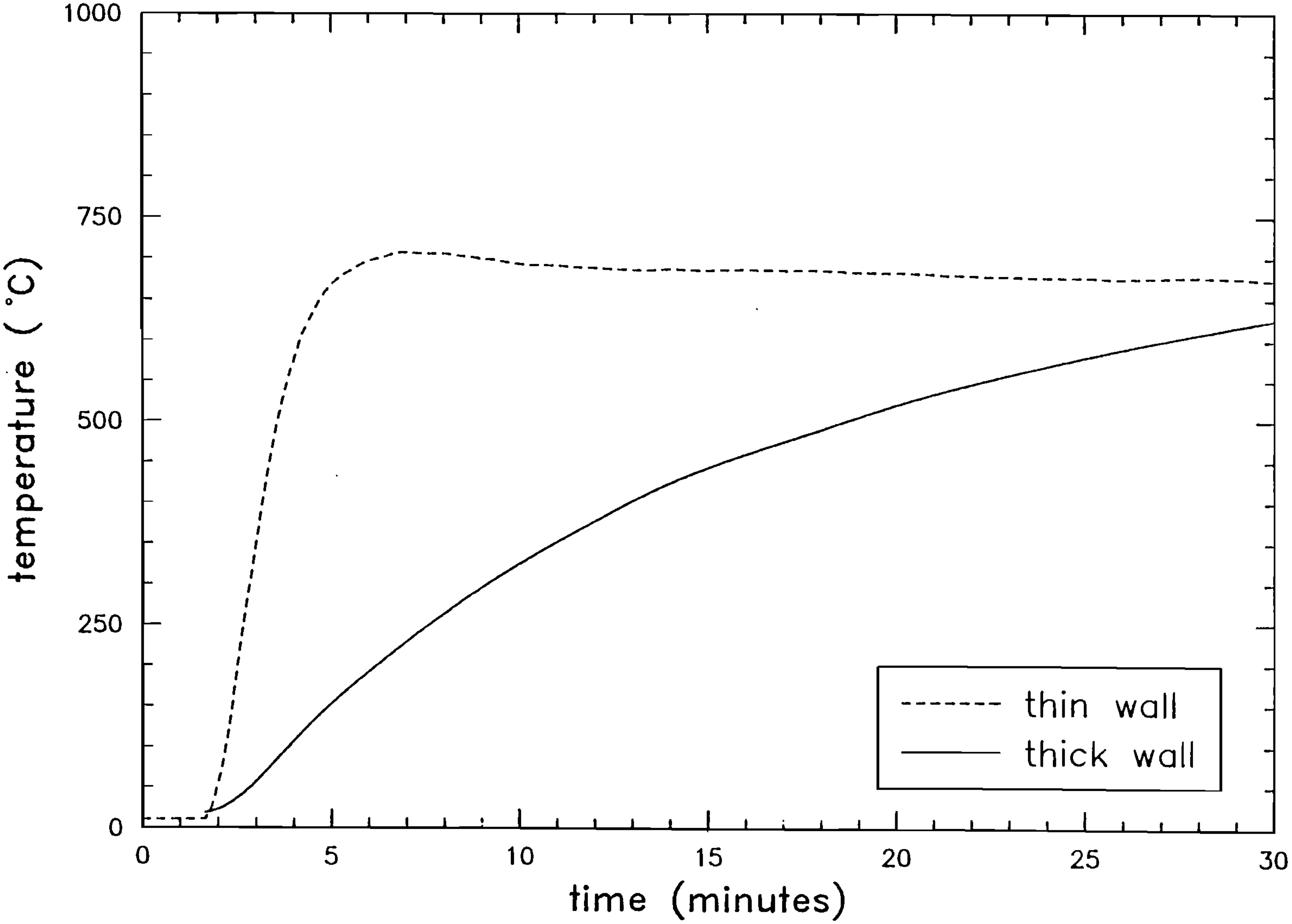

Figure 2.24 Surface Temperature Versus Time for the Small Wind Shielded Facility Tests

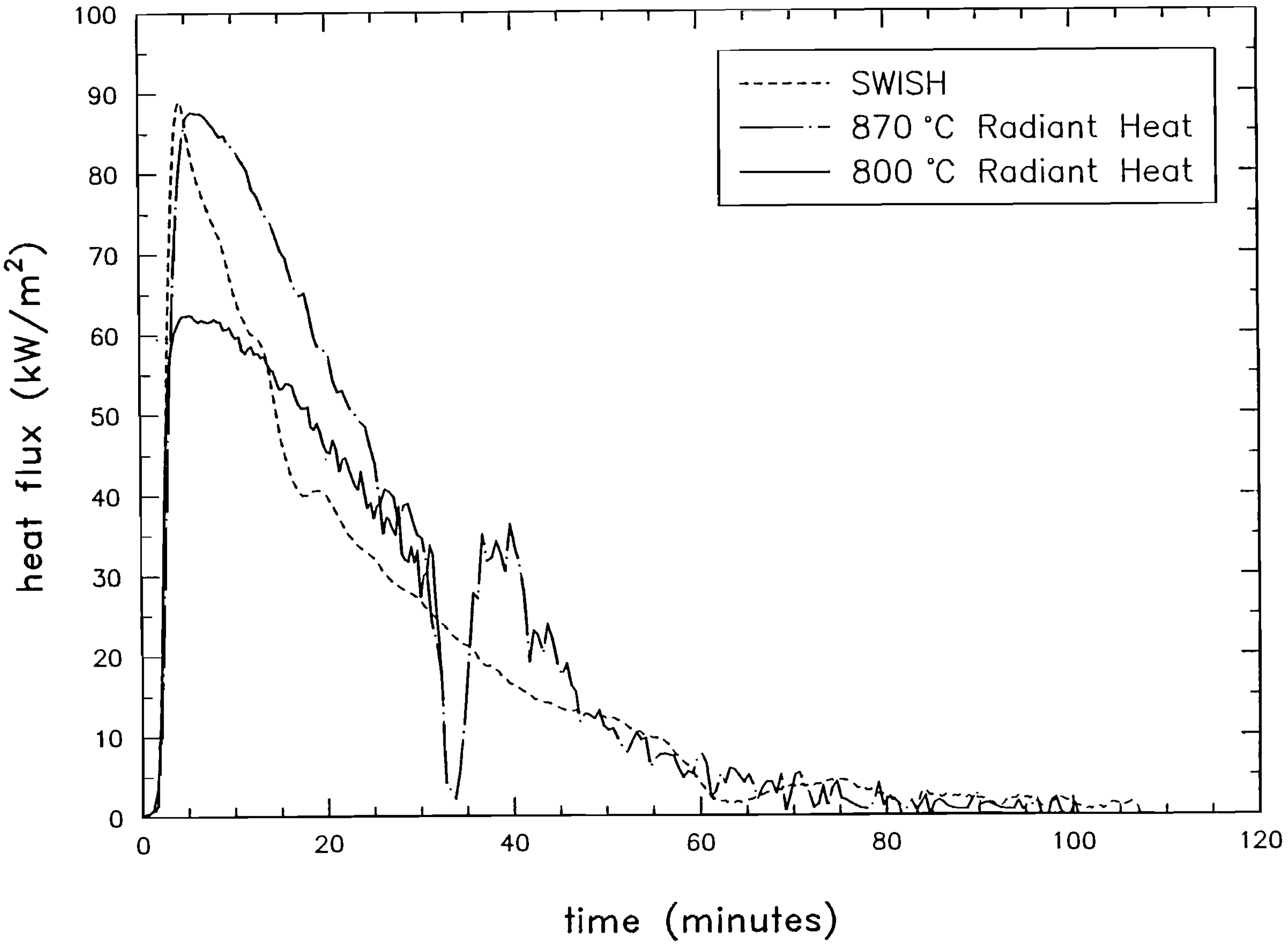

Figure 2.25 Heat Flux Versus Time for the Thick Wall Tests

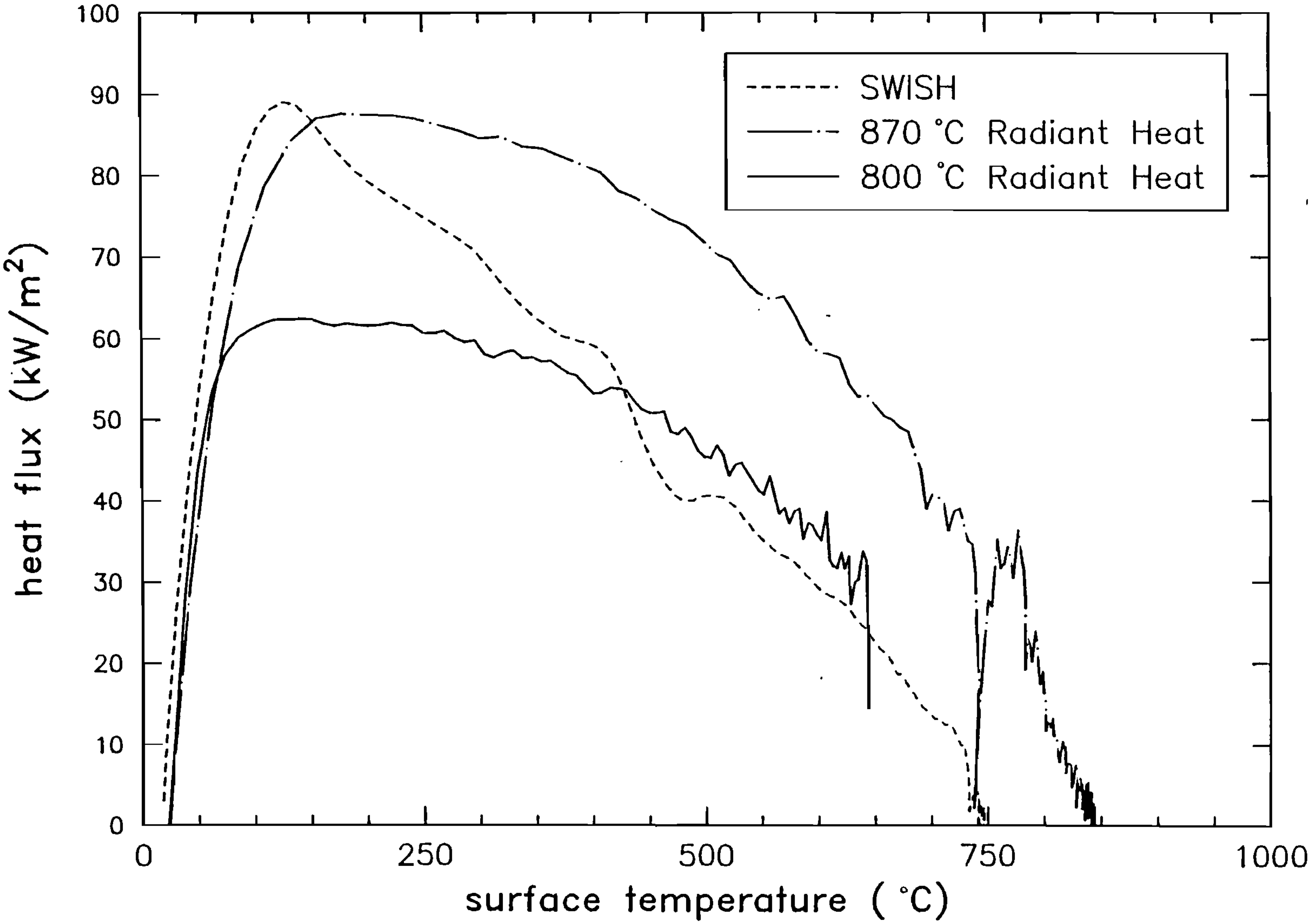

Figure 2.26 Heat Flux Versus Surface Temperature for the Thick Wall Tests

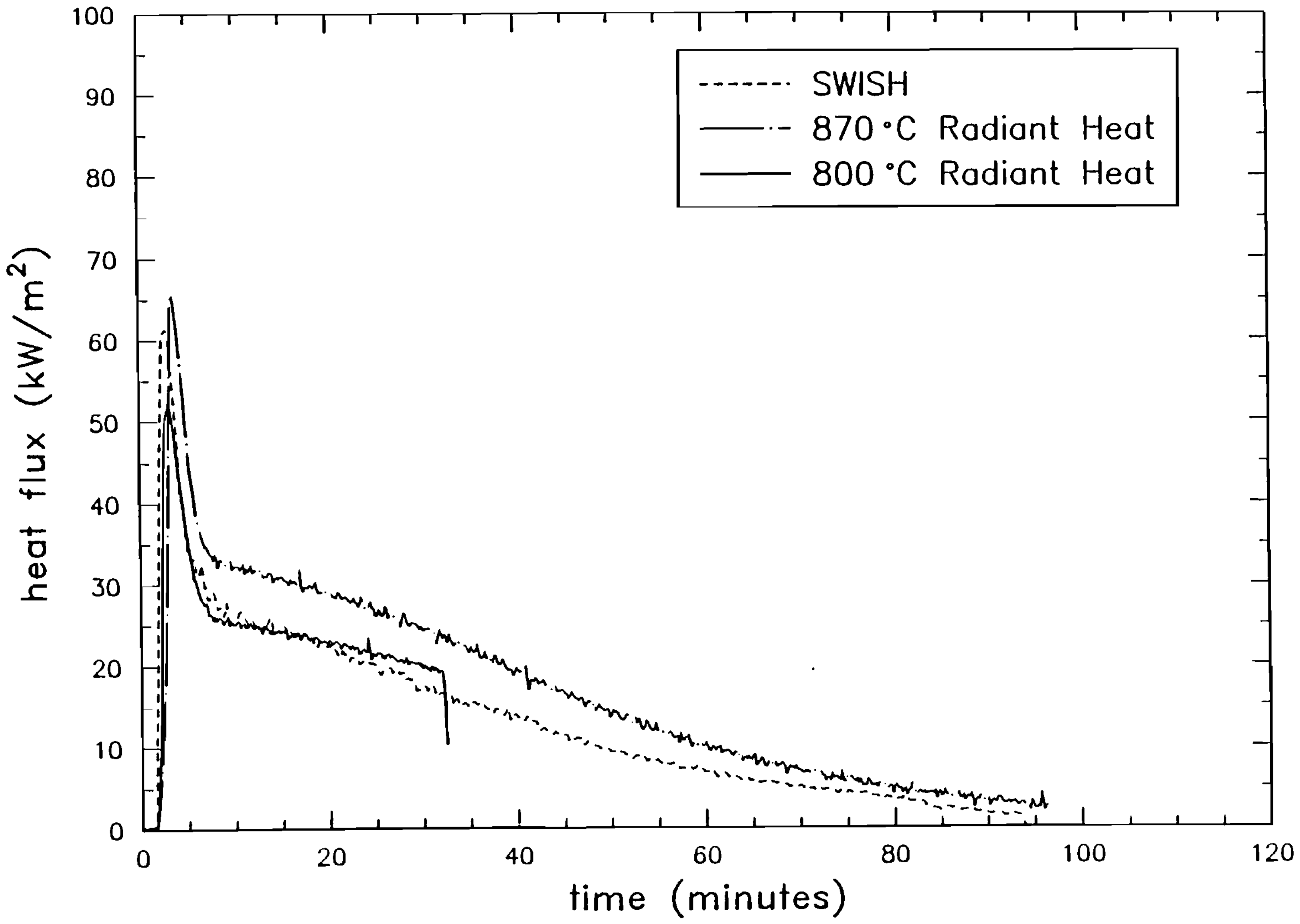

Figure 2.27 Heat Flux Versus Time for the Thin Wall Tests

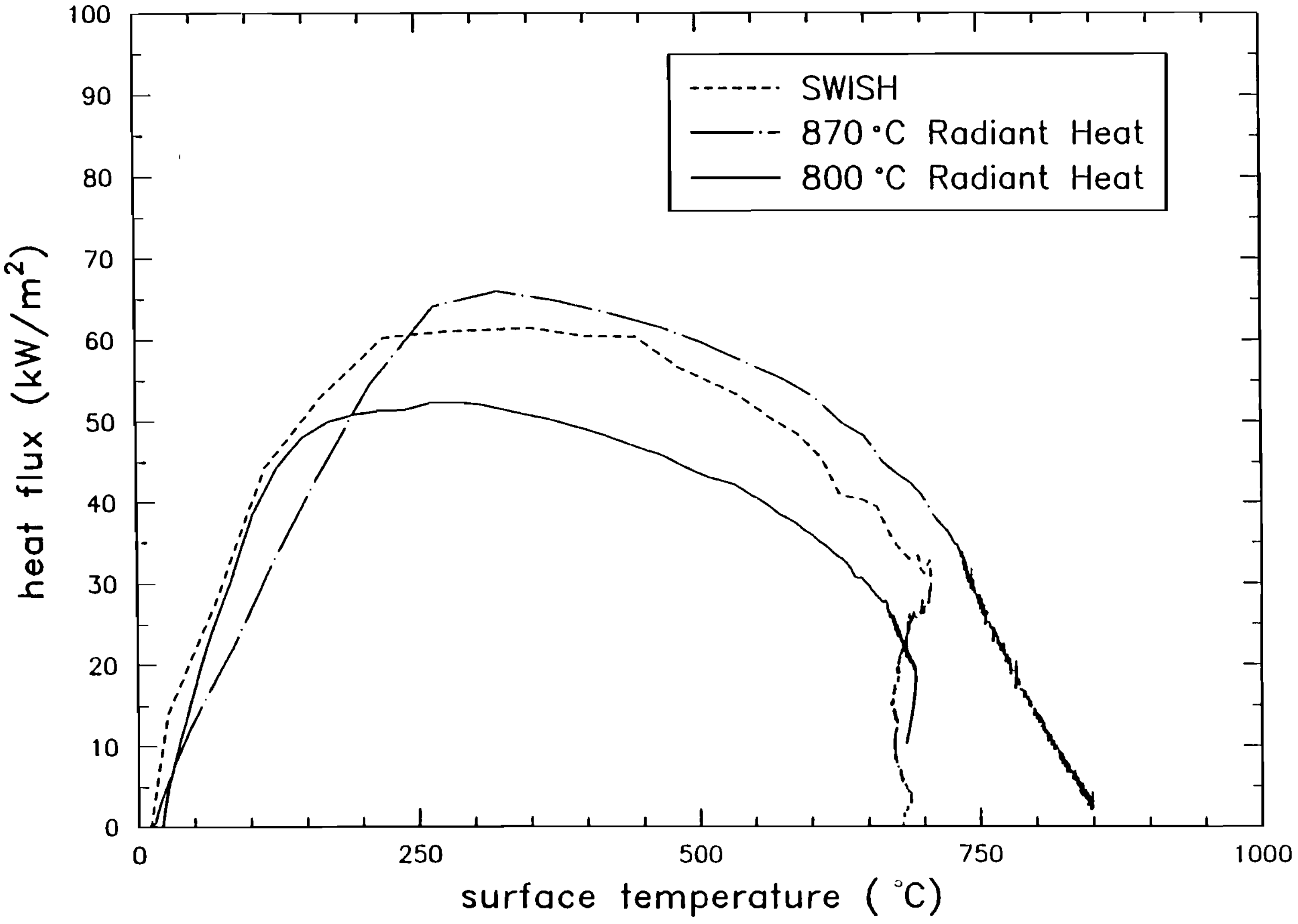

Figure 2.28 Heat Flux Versus Surface Temperature for the Thin Wall Tests

With a flame thickness of 0.7 m, the emittance of the flames was approximately 0.5. An emittance greater than 0.9 indicates an optically thick flame. The radiative flux would be approximately 50% of that expected in a fully engulfing fire. This might not be considered a satisfactory test because of reproducibility problems, but could be considered representative of many accident situations.

2.3.8 Cold Wall Heat Fluxes

Cold wall heat fluxes are shown in Figure 2.29. The cold wall heat fluxes for the radiant heat tests are relatively independent of the test unit. During most of the test period, the cold wall heat flux from the thick wall SWISH test was greater than that for the thin wall SWISH test.

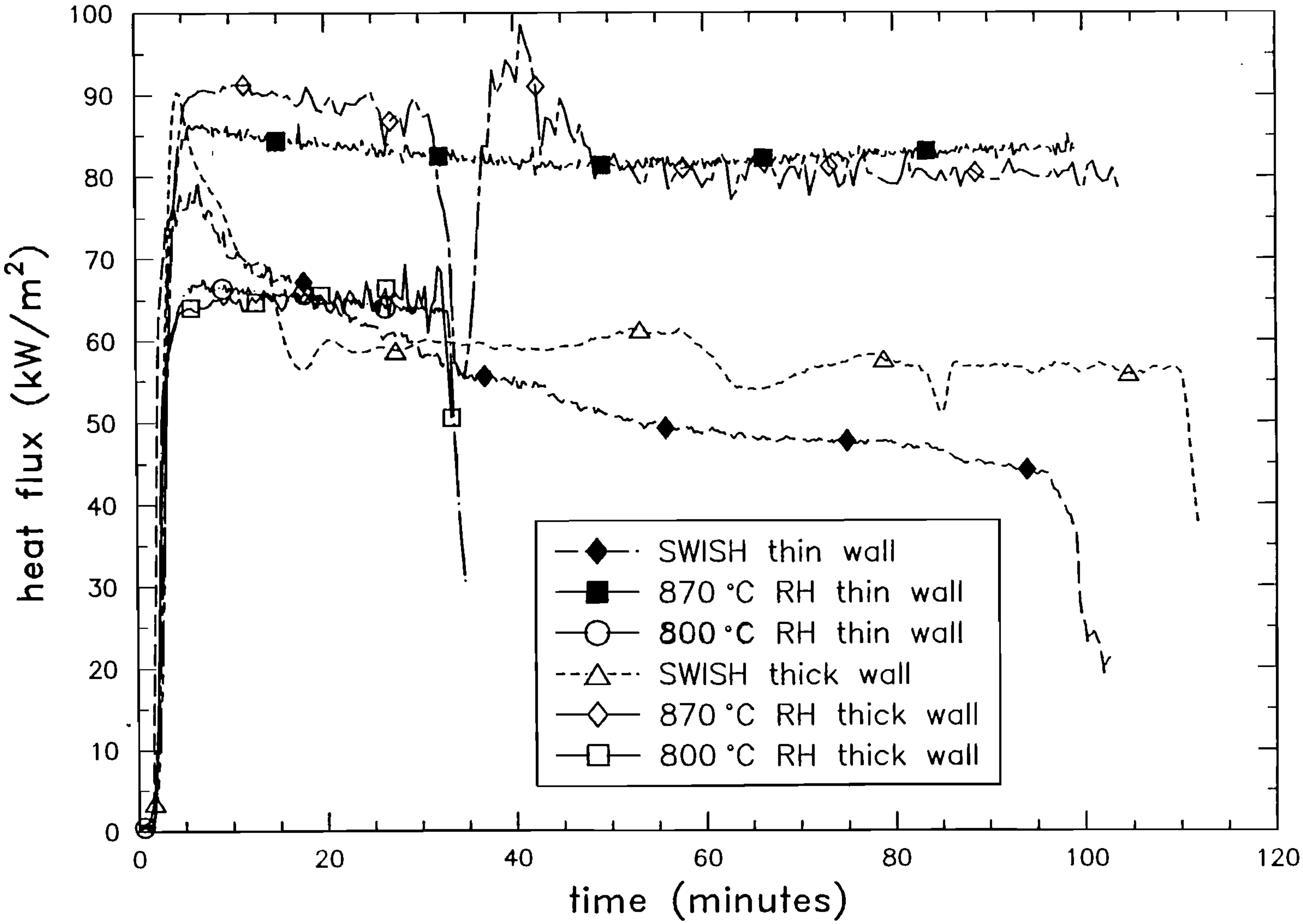

Figure 2.29 Cold Wall Heat Flux Versus Time

3.0 BOUNDARY CONDITION STUDIES

3.1 Calorimeter: - Predicted Versus Actual Data Comparisons

With some of the results from Section 2.0, the responses of the plate and cylindrical calorimeters can be estimated and compared to the actual measured responses. The following sections provide comparisons of the measured and calculated responses of both the front and back faces of the mild steel and stainless steel sides of the plate calorimeter and the thick-walled end of the cylindrical calorimeter.

3.1.1 Model Description

A general radiative and convective boundary condition was used as an input to SODDIT in the direct mode. This allows calculation of the front and back face temperature response of a surface as a function of time. The boundary condition used by SODDIT at the surface, from Blackwell et al. (1987), can be expressed as

$$-k_{tc}\delta T_s/\delta x = h_s(T_{fs} - T_s) + \alpha_s q_{ir} - \varepsilon_s \sigma (T_s^4 - T_{rad}^4) \tag{3.1}$$

Inputs to SODDIT are the thermal conductivity, k_{tc} specific heat c; absorptivity, α_s; surface emissivity, ε_s (all properties as a function of temperature); the convective heat transfer coefficient, h_s, as a function of time; the "free stream" temperature, T_{fs}; the incident radiative heat flux, q_{ir}; and the temperature of the environment, T_{rad}. Outputs from SODDIT (in the direct mode) include both the front face temperature, T_s, and the back face temperature, T_b, as a function of time. Condensation of any material on the surface is ignored in this model, and the cask surface is assumed to be gray.

The convective boundary condition was assumed to be $h_s(T_{fs} - T_s)$, where h_s is the convective film coefficient, T_{fs} is the free stream temperature, and T_s is unknown. The surface temperature, T_s, was calculated in SODDIT with an initial temperature and the boundary condition. T_{fs} was assumed to be the flame temperature, T_f. The value for h_s as a function of time was not known and was adjusted in the calculations to obtain a good fit with the experimental data. With SODDIT the response of the plate calorimeter to the fire was estimated with several values of h_s. In this way convective rates in the free and forced convective regimes could be simulated.

The radiative boundary condition is $\alpha_s q_{ir}$, where α_s is the absorptivity of the surface and q_{ir} is the radiative heat flux incident on the surface. The value of q_{ir} was determined by calculating $\varepsilon_f \sigma T_f^4$, where ε_f was assumed equal to 0.82. This value for ε_f was determined as described in Section 2.0. The transpiration radiometer data from the gauge in the mild steel side of the plate calorimeter (gauge no. 4) were used to estimate ε_f. The average of the transpiration gauge data was compared with the average of the data from $\varepsilon_f \sigma T_f^4$, where T_f was the flame temperature from a thermocouple close to gauge no. 4 and ε_f was adjusted until the averages were the same. The value $\varepsilon_f = 0.82$ was the result. Although there are many uncertainties in the data, this value for ε_f is a reasonable one. The transpiration gauge data were not used as an input to SODDIT. Because the transpiration gauge responded faster than the thermocouple measuring T_f, use of the transpiration gauge data for q_{ir} and the thermocouple data for T_f might have caused inaccuracies in the calculations.

The reradiative condition was assumed to be $\varepsilon_s \sigma (T_s^4 - T_{\mathrm{rad}}^4)$, where ε_s is equal to α_s for steady state, T_s is the front face temperature, and T_{rad} is zero. Although T_{rad} should really be the temperature of the environment, little error results from assuming it is zero.

The surface was painted with the high-absorptivity black paint Pyromark Black. Since the absorptivity of both virgin and used paint have been measured, the surface properties ε_s and α_s are well known (Longenbaugh and Matthews, 1988).

3.1.2 Comparisons of Predicted and Measured Responses

Results from the direct mode SODDIT calculations are shown in Figures 3.1 through 3.3. On all subsequent plots the "actual" front face temperature is represented by the data generated from SODDIT, not the measured front face temperature because, as discussed in Section 2.0, the measured front face temperatures are thought to be less accurate than the calculated data.

Figure 3.1 shows a comparison of the "actual" and calculated response of the front face temperature of the mild steel side of the plate calorimeter, with no convection assumed ($h_s = 0$). The predicted response, shown by the lower curve, is lower than the actual temperature throughout the test. Although the predicted response is low, it is within about 11% of the actual response at the maximum temperature reached.

Figure 3.2 shows the results when a constant convective coefficient is used. The value for h_s was 56.8 W/m^2-K. This value is in the forced convective regime and agrees quite well with an average value from Russell and Canfield (1973) for JP-5 fires. The agreement is very good until about 37 min, when the fire is over. Because there is no forced convection after the fire is out as assumed with the SODDIT code, one might expect that the model would predict a faster cooldown than what actually occurred, and this is the case.

Figure 3.3 shows the results of a calculation using a forced convective heat transfer coefficient up to 37.5 min during the fire and a free convective heat transfer coefficient after the fire is over. The values used for h_s are 56.8 W/m^2-K during the fire and 11.4 W/m^2-K after the fire is over. The predicted response is as good as that shown in Figure 3.2 for during the fire but much better after 37.5 min. The predicted and actual responses of the mild steel side of the plate calorimeter are within 10% throughout the test.

Figure A.12 shows the results of a calculation on the stainless steel side; h_s was 56.8 W/m^2-K during the fire and 11.4 W/m^2-K during the cooldown, as in Figure 3.3. The predicted response is always lower than the actual response but is still within 10% throughout.

Figures A.13 and A.14 show results for the cylindrical calorimeter. The same convective coefficients used in Figures 3.3 and A.12 were used in all subsequent calculations: $h = 56.8$ W/m^2-K during the fire and $h = 11.4$ W/m^2-K after the fire is out. Agreement between the predicted and measured front face temperatures is very good in Figure A.13—less than 10%—but only within 15% in Figure A.14.

Figures A.15 through A.18 show back face temperature comparisons on the plate and cylindrical calorimeters, corresponding to the values in Figures A.12 through A.14 for the front face. Overall agreement between predicted and measured response is very good.

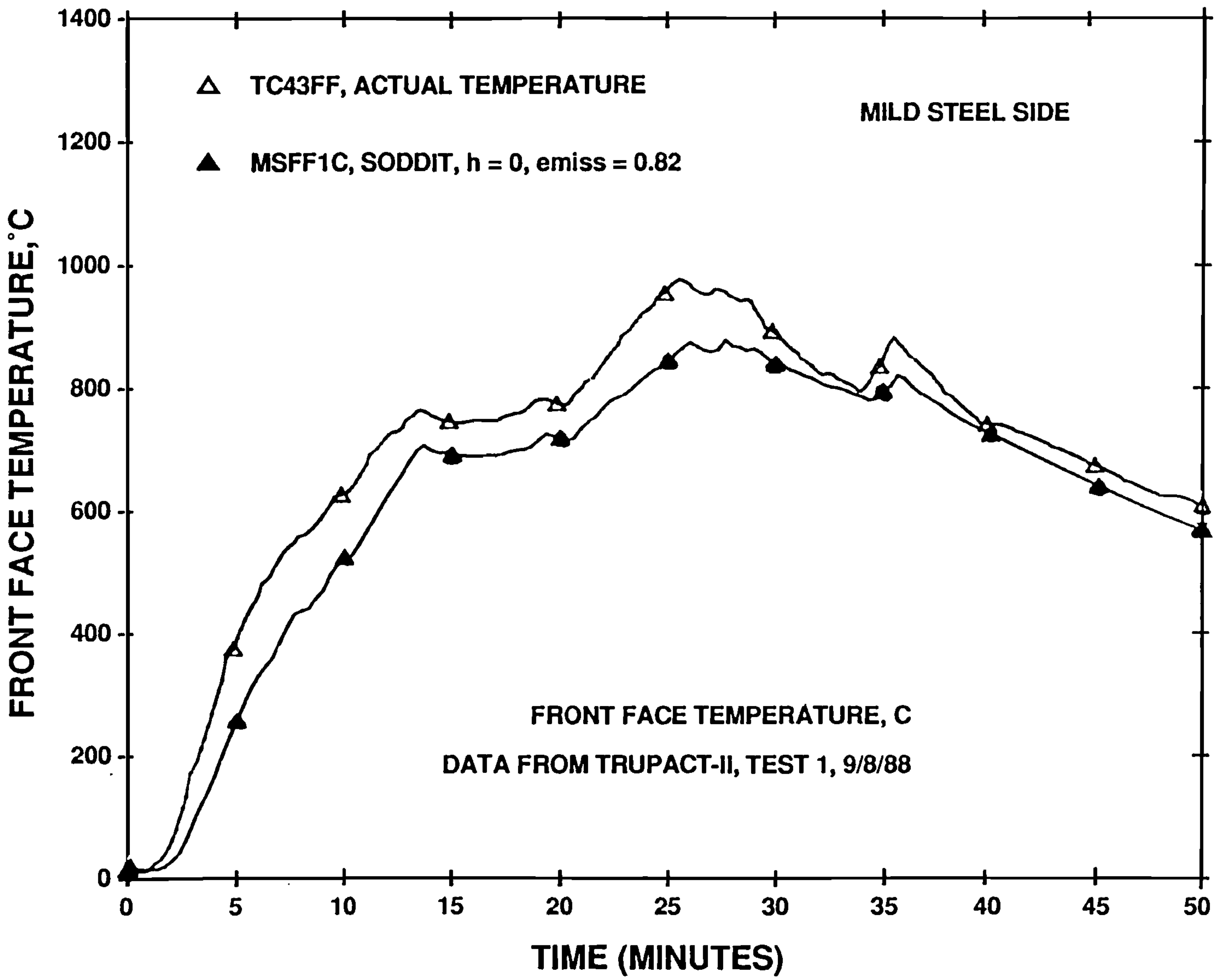

Figure 3.1 Front Face Temperatures With No Convection—Mild Steel Side of Plate Calorimeter (see Figure 2.5 for location)

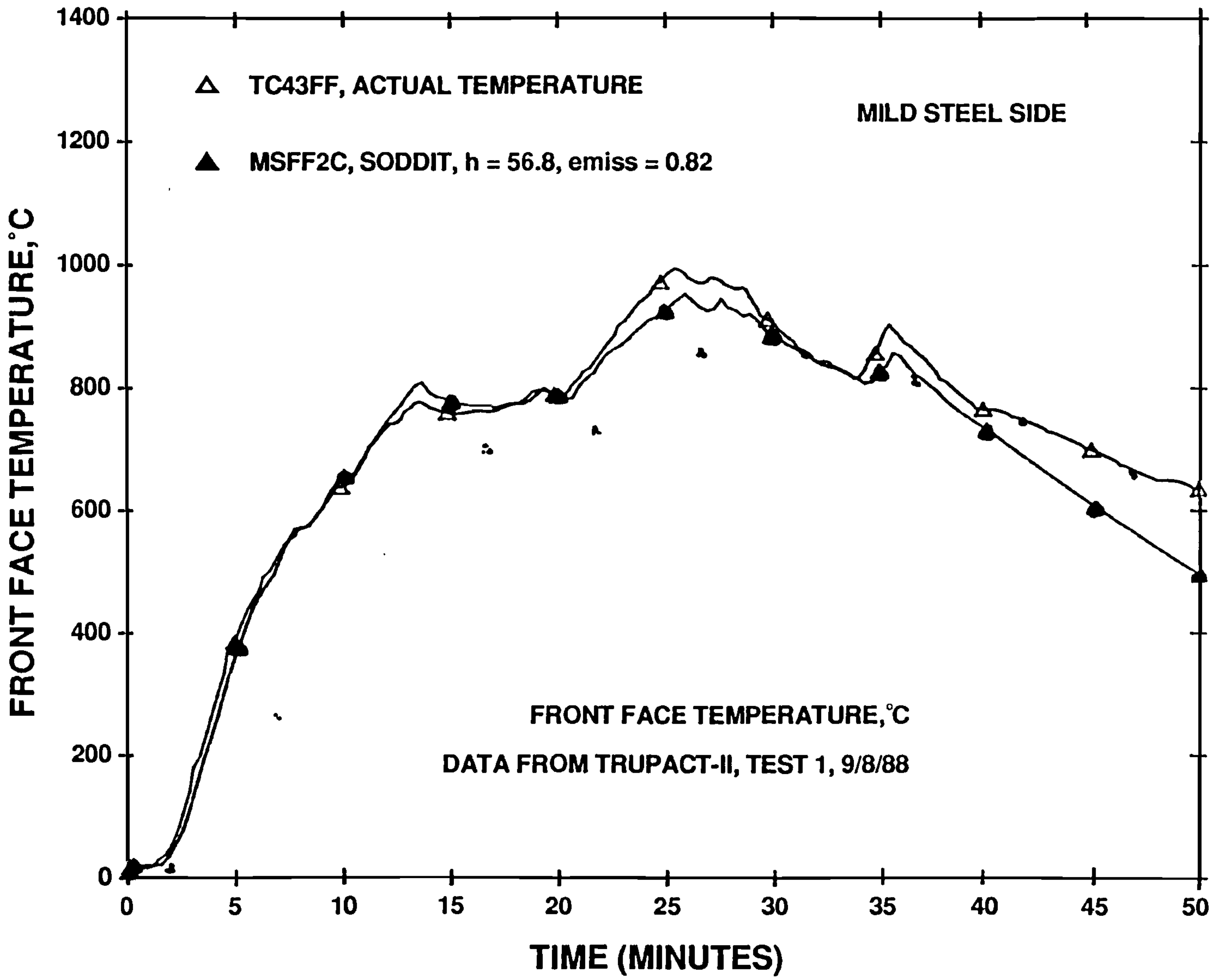

Figure 3.2 Front Face Temperatures With Convection—Mild Steel Side of Plate Calorimeter

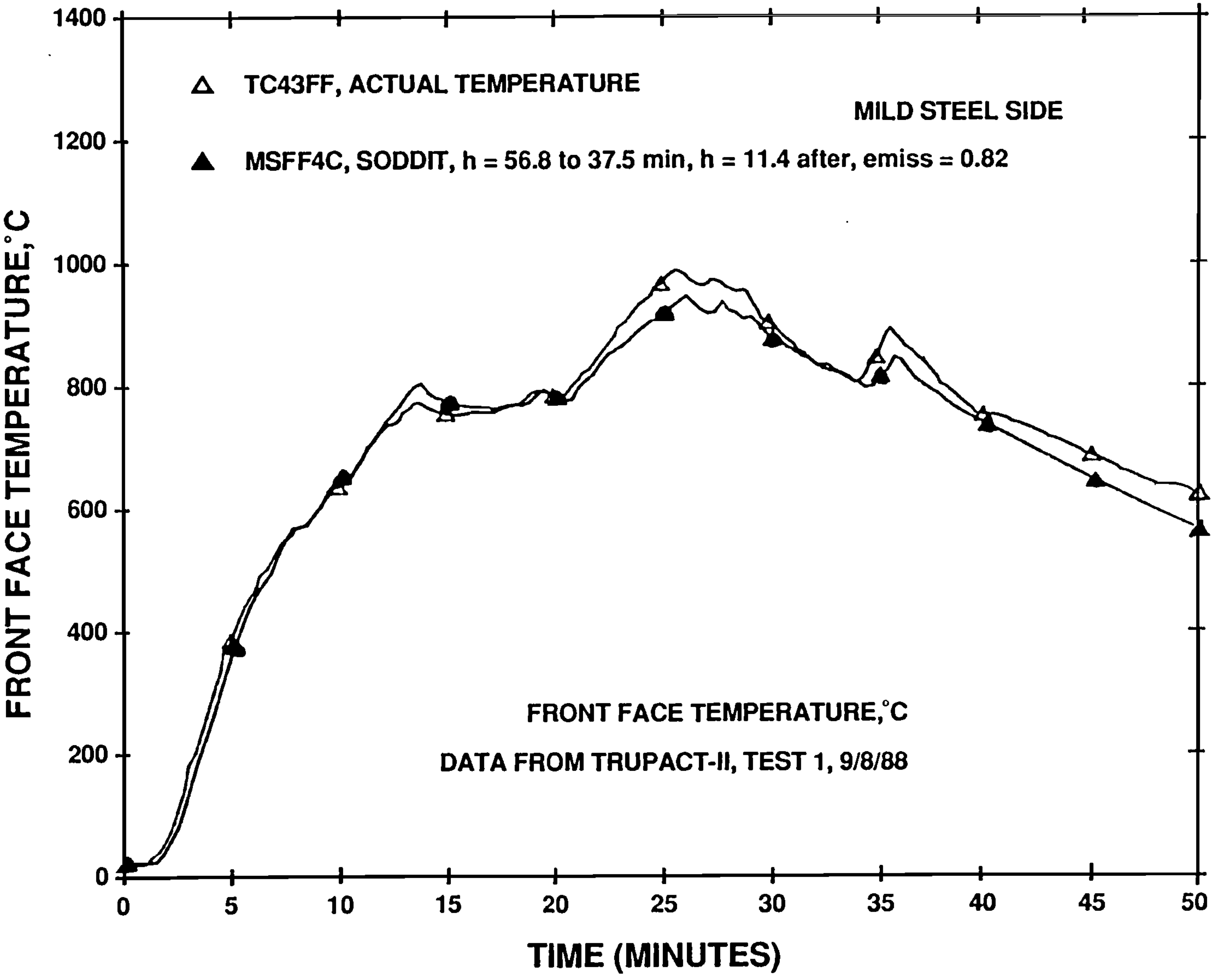

Figure 3.3 Front Face Temperatures With Two Convection Coefficients—Mild Steel Side of Plate Calorimeter

In most of the comparisons, the predicted temperature is less than the actual temperature. Keltner et al. (1989) have shown for heat transfer in severe accident conditions that gas (free stream or flame) temperature measurements in furnaces and fires made with unshielded thermocouples can be low by 10 to 30%. None of the flame temperature thermocouples on the cylindrical calorimeter was shielded (TC5 to TC8), and so the cylindrical calorimeter was almost certainly affected by their output. This error source may explain in part why the model consistently predicts lower temperatures than the actual temperatures of the calorimeters.

Figures 3.4 through 3.6 provide a comparison of predicted and measured front face temperatures. The input to the SODDIT code was the boundary condition specification set forth in 10 CFR 71: a "fire temperature" of 800°C and a fire emissivity of 0.9. This calculation was made for the stainless steel side because that side most closely represents the outer skin of the TRUPACT-II transport container, and also for the cylindrical calorimeter to simulate a very massive, thick-walled structure. The testing of the TRUPACT-II transport container was governed by the 10 CFR 71 regulations. As Figure 3.4 shows, for this location in this particular fire, the front face temperature prediction is below the actual temperature, especially during the early stages of the fire. In addition, the signature of the predicted response is not similar to the actual response. Figures 3.5 and 3.6 show that the 10 CFR 71 model again underpredicts the actual temperature, this time on the cylindrical calorimeter. However, in this case the signature is similar to the actual temperature, because the thick-walled cylinder responded slowly to the fire fluctuations. Comparison results would be the same whether the SODDIT code or another thermal computer code is used to complete the 10 CFR 71 portion of the calculations. Differences between actual and regulatory temperature histories shown in Figures 3.4 through 3.6 can, at least in part, be attributed to point-to-point variations of surface heat fluxes. These local variations occur in actual fires in contrast to the overall uniform surface heat flux specified by 10 CFR 71. This underscores that the 10 CFR 71 pool fire simulation was selected to encompass the average behavior of most real world transportation fires by providing a test typical of very severe accidents. This hypothetical fire accident condition and the fire model included in the regulations do not predict localized effects in very intense test fires.

A possible objection to comparing the above 800°C measurements to actual measurements is that a JP-4 fire is "hotter" than the average 800°C fire in the 10 CFR 71 regulations. This is certainly true in the vicinity of the plate calorimeter, where the average flame temperature was about 935°C (not shown). However, the argument is not persuasive for other locations in the fire. If the average flame temperatures from the towers surrounding TRUPACT-II are considered at the 7.5- and 11.5-ft levels, the result is different. The 7.5- and 11.5-ft levels span most of the height of the TRUPACT-II container. The average flame temperatures from test 1 on the east tower were 834°C and 583°C, for an average of 708°C. Similarly, the overall average for the two stations on the north tower was 977°C; the south tower, 888°C; and the center tower, 731°C. For all four towers, the overall average is 826°C for test 1. For test 2, the overall average was 809°C, and for test 3, 824°C. These averages are all close to the 800°C "average fire temperature" described in the regulations. However, like the response of the plate calorimeter, actual measurements on the TRUPACT-II container (not shown) were much higher (up to 1093°C) than would be predicted from an 800°C average fire temperature specification. Therefore, even with the towers measuring temperatures that averaged close to 800°C, the actual response of objects in the fire would be as if the average fire temperature was much higher. It seems that the best that might be obtained from a constant-temperature fire specification is a confidence level estimate (Nelson, 1986). That is, if the constant-temperature fire specification is high enough, for example, 1010°C, then the actual response of the object would be below that temperature some high percentage of the time. It does not seem possible that the actual response shape can be effectively modeled with a constant temperature, unless the structure is massive, like the cylindrical calorimeter. In that case, a higher constant-temperature specification than 800°C may make possible effective modeling of the response.

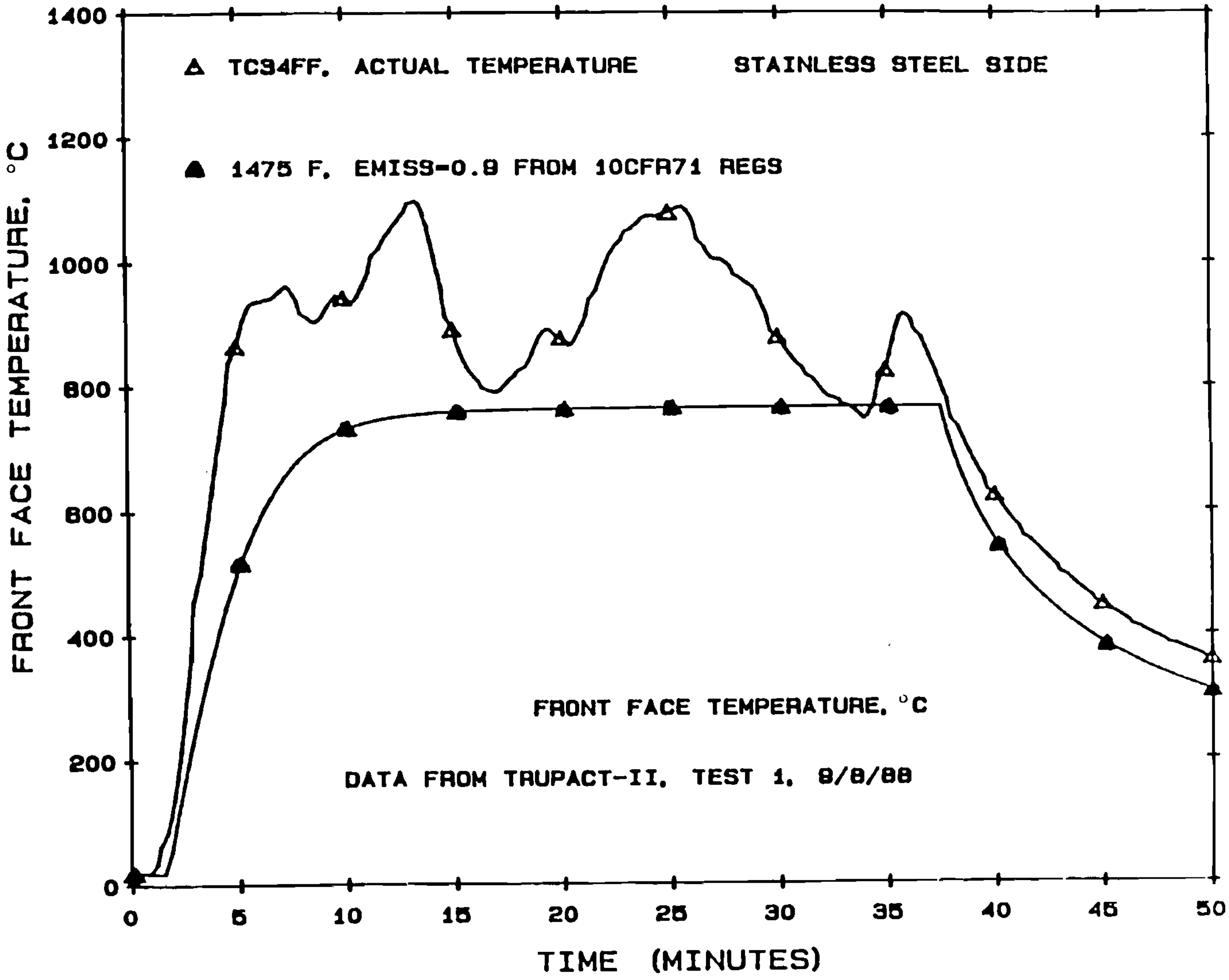

Figure 3.4 Front Face Temperature Comparisons with 10 CFR 71 for the Stainless Steel Side of the Plate Calorimeter

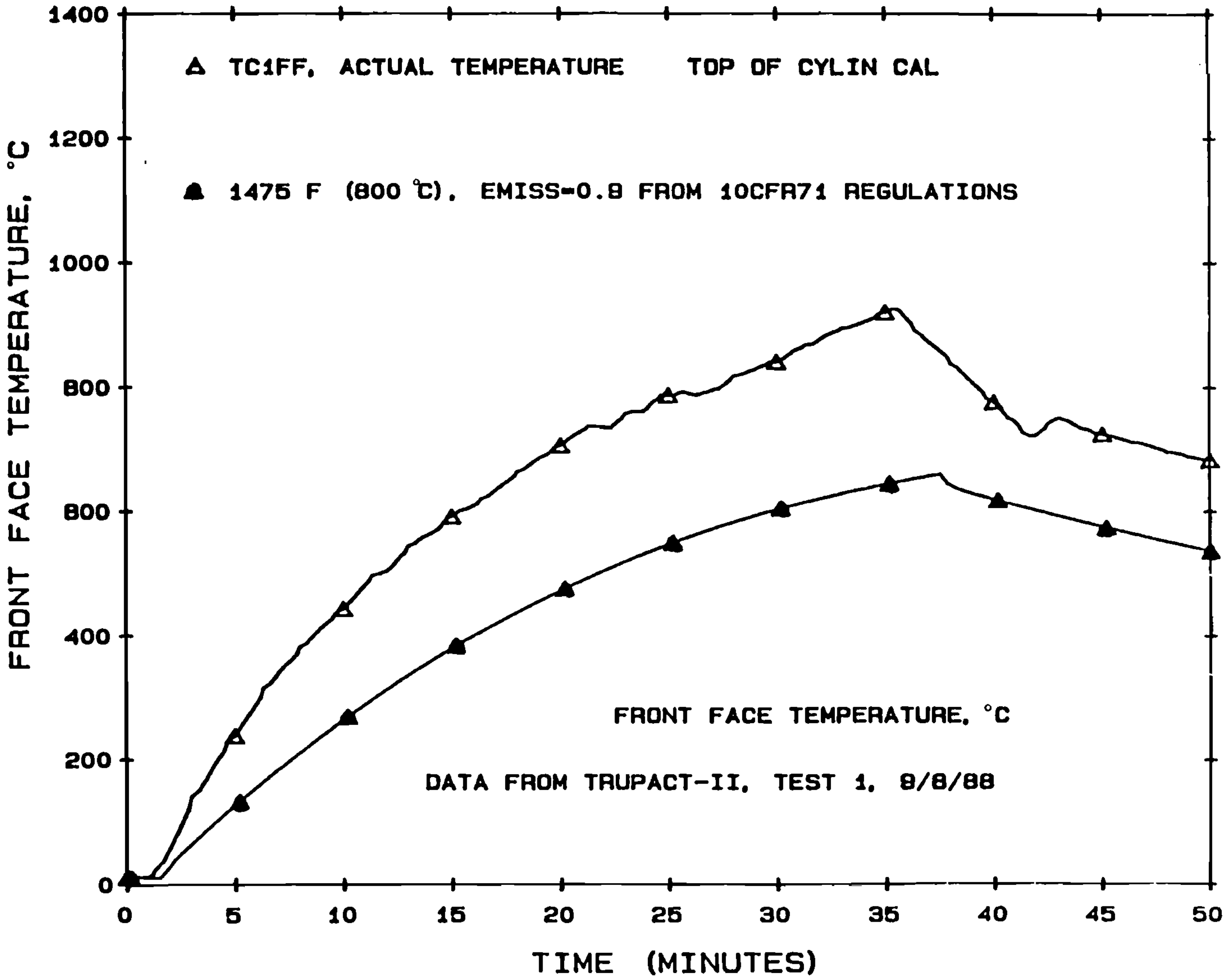

Figure 3.5 Front Face Temperature Comparisons with 10 CFR 71 for the Top of the 1.4-m Calorimeter

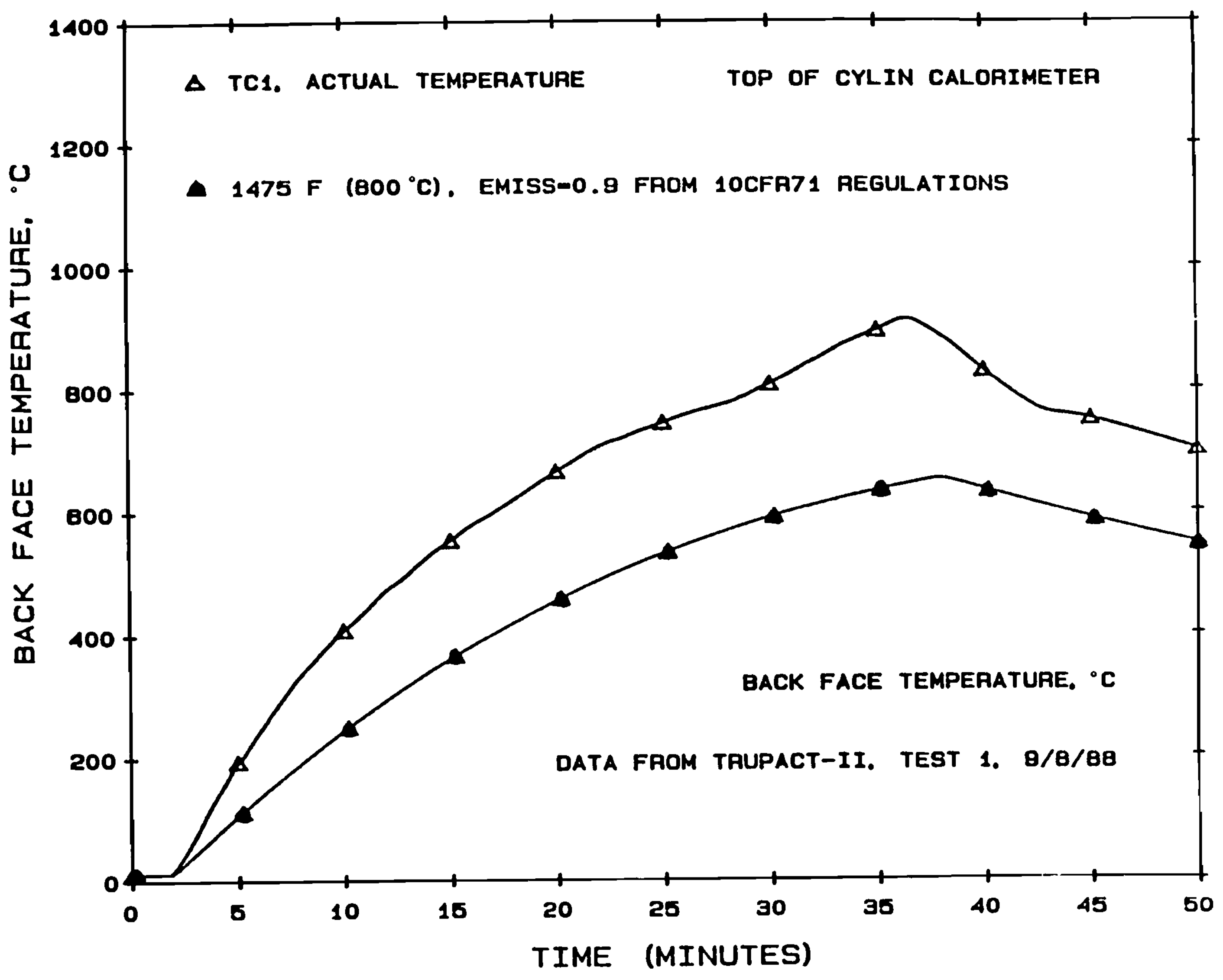

Figure 3.6 Back Face Temperature Comparisons with 10 CFR 71 for the Top of the 1.4-m Calorimeter

3.2 Influence of Cold Surfaces

3.2.1 Background

Results of large pool fire tests indicate that calorimeters of different size and mass will measure significantly different incident heat fluxes in the same fire. The influence of a thermally massive test article (cold surface) on the local fire environment would explain these results (Gregory et al., 1987a,b). This section describes the work performed to determine whether such an influence can be explained and modeled, and if so, whether the magnitude of the effect could be responsible for the experimentally measured difference in heat fluxes to calorimeters of different sizes. If such an influence does exist and is of sufficient magnitude to explain the experimental results, then the influence of a test article on the local fire environment must be taken into account in analytic models of the response of objects to engulfing fire environments.

Some of the experimental data that indicate the existence of a size and thermal mass effect on measured heat fluxes are shown in Figures 3.7 and 3.8. The average heat fluxes from a series of three tests are plotted versus calorimeter surface temperature. In these tests 0.10-m-diameter calorimeters (S3000 and S1180) and 0.20-m-diameter calorimeters (S4000 and S2180) were placed at the same elevations as corresponding stations on the top and bottom of a 1.4-m-diameter, 10-ton calorimeter (T3000 and T3180).

The data shown in Figure 3.7 for the lower elevations (underside of the calorimeters) are relatively smooth. The peak heat flux to the 1.4-m-diameter calorimeter is about 20% below the peak heat fluxes to the 0.10- and 0.20-m-diameter calorimeters. The magnitudes of the heat fluxes to the 0.10- and 0.20-m-diameter calorimeters are approximately equal over the entire temperature range. All three heat flux curves converge to approximately the same value for surface temperatures above about 480°C.

The data for the higher elevations (top side of the calorimeters) shown in Figure 3.8 reveal much more fluctuation, perhaps due to wind or wake effects. The peak heat fluxes to the 1.4-m-diameter calorimeter are about 33% less than the peak heat fluxes to the 0.10- and 0.20-m-diameter calorimeters. The three heat flux curves show less scatter at temperatures above about 530°C.

The above experimental data suggest that the size and thermal massiveness of the test article affect measured heat flux in ways that are not predicted by simple radiation laws for a transparent medium. The size effect is apparent in that the heat fluxes for the 1.4-m-diameter calorimeter are significantly lower than the heat fluxes for the smaller calorimeters. The thermal mass (surface temperature) effect is suggested by the convergence of all three curves at the higher surface temperatures, when thermal massiveness is no longer important, that is, no longer influences the surrounding fire environment to a significant extent. Trends such as these in large-pool-fire test data defied explanation for many years.

The data provided above and the theory that it appears to support mean that for massive objects such as railcars, heat fluxes during the early portion of a fire will likely be lower than expected, but as the object heats up, as could happen in a 100-min duration fire, the heat fluxes will be closer to expected values. The net effect is that the total heat flux is likely to be lower than might be predicted from simple analytical models. If phase change of cargo occurs, then the object response of the railcar is more complicated, as mentioned in Section 2.3 of this report.

3.2.2 Analytic Model

In providing an understanding of the experimentally observed reduction in heat transfer to thermally massive objects, the purpose of this work, many simplifying assumptions were necessary to isolate and elucidate the important heat transfer mechanisms in the fire. Since only

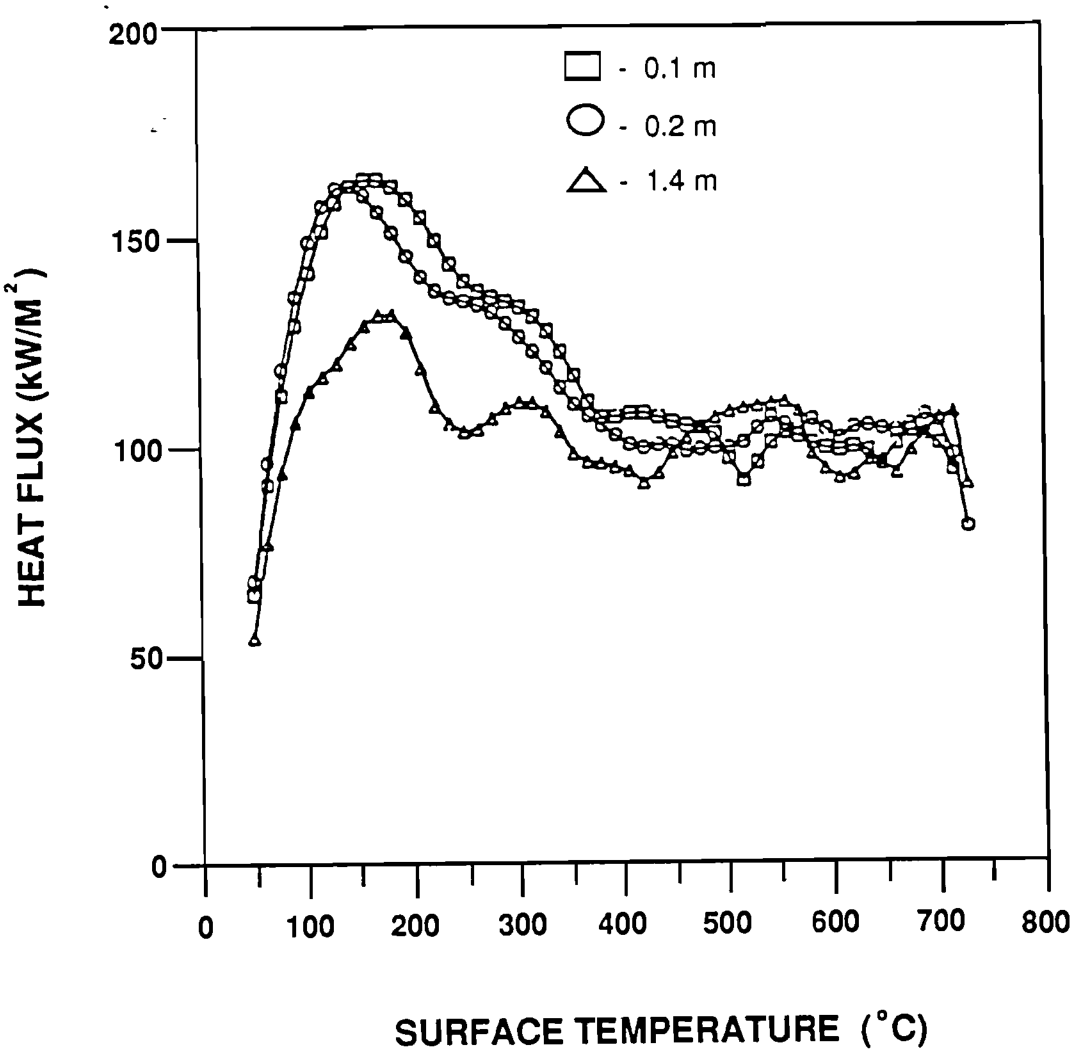

Figure 3.7 Experimentally Measured Heat Fluxes to Three Different-Size Cylindrical Calorimeters: Bottom of Calorimeters

scoping calculations were appropriate, the simplest model possible that still retained the important physics was adopted. The simplified model was developed in an effort to isolate the independent effects of surface temperature, convective velocity, flame temperature and composition (radiation absorption coefficient), viscous boundary layer, turbulent mixing, and combustion source strength, even though these effects are highly coupled.

In the large pool fires under consideration, approximately 10 to 20% of the heat transfer is via convection; the majority is via radiation. Therefore, as a first approximation, convection heat transfer was neglected in the model, but because of the coupling of radiation to the flow field, the fluid motion must be included.

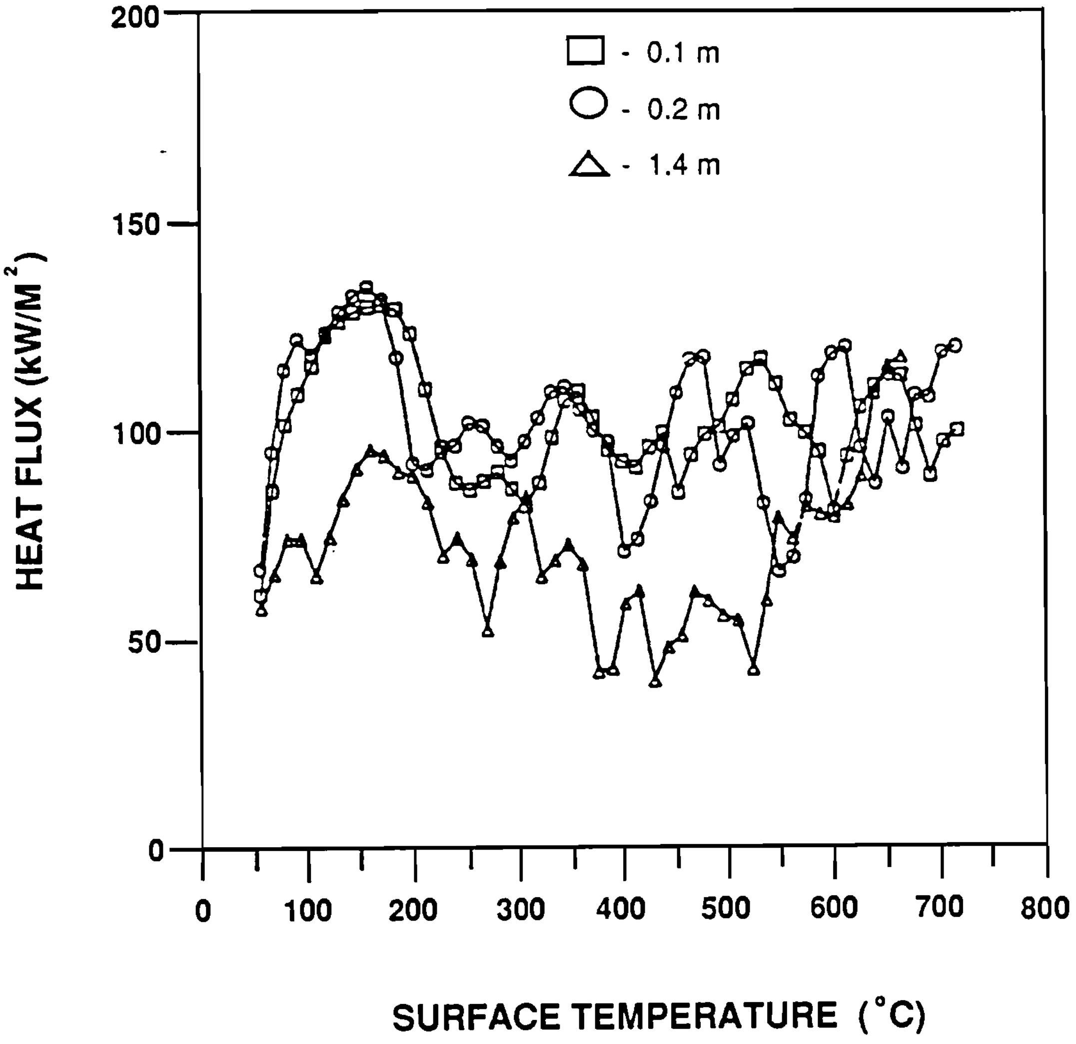

Figure 3.8 Experimentally Measured Heat Fluxes to Three Different-Size Cylindrical Calorimeters: Top of Calorimeters

The simple geometry shown in Figure 3.9 was selected to model a representative test article: a vertical flat plate at constant temperature completely engulfed by thick flames. Some test articles such as a vertical wall of a transport container would be reasonably well represented by this configuration. Other articles such as cylindrical casks will respond differently because the shape and orientation of the test article will influence the results. For example, the flow field and radiation field around a circular cylinder in cross-flow are fundamentally different than along a vertical flat plate. The flat plate geometry was selected because the flow field and radiation field along a flat plate are relatively easy to model compared to other geometries. The combustion gases travel upward along the plate with some uniform velocity. Viscous boundary layer effects are neglected, since the viscous boundary layer is on the order of a few inches, whereas radiation effects extend several meters into the flow field. The fluid is modeled as nonconducting, with no turbulent mixing and no concentration gradients. The combustion products are treated as dry air with uniform soot distribution and constant properties.

Thermal radiation to the surface of the plate from the combustion gases was modeled under the assumption that one-dimensional gray gas radiative transfer is normal to the surface. The plate surface was assumed to be a blackbody absorber and emitter. The far field boundary condition

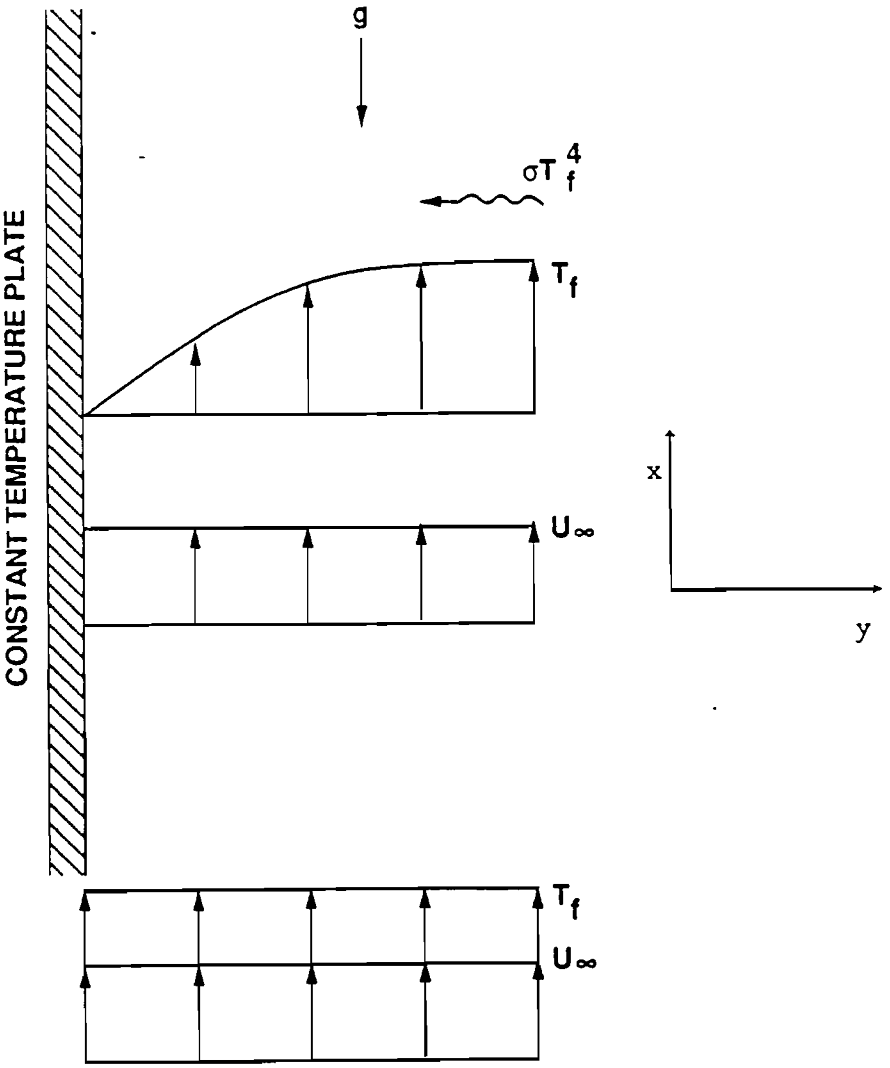

Figure 3.9 Model Geometry

was applied at the distance from the surface at which any thermal radiation originating from the surface had been attenuated by 99%. This distance is a function of the absorption coefficient of the combustion gases. For a typical absorption coefficient of 1 m^{-1}, the far field boundary condition was applied at a distance of 3 m from the surface. At this distance the surface does not have any radiative influence on the fluid at the far field boundary.

The combustion gases were modeled with and without a combustion source term. For the cases modeled without a source term, the far field boundary was set equal to the flame temperature and given an emissivity of unity. For the cases with a combustion source term, the far field boundary temperature was calculated with a zero temperature gradient at the boundary.

Under these conditions the energy equation reduces to

$$\rho c_p\left(\frac{\partial T}{\partial t}+U_\infty\frac{\partial T}{\partial x}\right)=\frac{\partial}{\partial y}(q_r)+S''' \tag{3.2}$$

where q_r is the local radiative heat flux and S''' is the local volumetric combustion heat source. This equation was solved numerically using a line-by-line implicit procedure in the y direction and marching upward along the surface. To solve equation (3.2), q_r was used from the previous time step. Only 10 to 20 iterations (time steps) were necessary to reach a steady-state solution.

A two-flux formulation of the one-dimensional gray gas radiative transport equation was used to solve for the local radiative flux, q_r, based on the temperature field. Use of the exponential kernel approximation (Siegel and Howell, 1981) yields

$$\begin{aligned} q_r(k) = {} & \sigma T_1^4 \exp\left(-\frac{3}{2}k\right) - \sigma T_2^4 \exp\left[-\frac{3}{2}(k_D - k)\right] \\ & + \frac{3}{2}\int_0^k \sigma T^4(k')\exp\left[-\frac{3}{2}(k-k')\right]dk' \\ & - \frac{3}{2}\int_k^{k_D} \sigma T^4(k')\exp\left[-\frac{3}{2}(k'-k)\right]dk' \end{aligned} \tag{3.3}$$

where

T_1 = surface temperature,
T_2 = far field boundary temperature,
k = optical path length, and
k_D = optical path length at the far field boundary.

Fires of this type are absorption dominated, and so scattering can be neglected (Longenbaugh and Matthews, 1988). The optical path length is then the integral of the absorption coefficient along the physical path length:

$$k = \int_o^y \alpha dy \tag{3.4}$$

where α is the soot absorption coefficient, a function of soot concentration.

The combustion source term in equation (3.2) was estimated based on experimental data (Gregory et al., 1987a,b). The total heat release rate of the fire was divided by the estimated continuous flame volume. This provided a ballpark number for examining the influence of a combustion source term. For all but one case with a combustion source term, S''' was assumed to be constant and uniform. An additional case was evaluated in which the combustion source term was assumed to be a function of local temperature. For this case the reaction rate was assumed to depend on temperature according to a first-order Arrhenius relation:

$$\frac{S'''}{S_0'''} = \frac{T_0 \exp(-E/RT)}{T \exp\left(-E/RT_0\right)} \tag{3.5}$$

where S_0''' is the constant source term discussed above, T_0 is a reference temperature at which S''' equals S_0'', R is the universal gas constant, T is the local combustion gas temperature, and E, the activation energy of fuel, was estimated as 30 kcal/mol. A reference temperature of 897°C was used. That temperature was selected to keep the exponential behavior of equation (3.5) within physical limits and to match the far field boundary temperature at the top of the surface to the temperature calculated with a constant source term. This allows comparison of the two solutions.

A length of 1 m was selected for the vertical flat plate in the model. This is representative of the characteristic length of the larger calorimeters used in the experiments.

3.2.3 Results

The model described above was employed to investigate the influence of a cold surface on engulfing flame environments. The calculations were of a scoping nature to assess the magnitude of the effect of radiation-convection interaction on the incident radiative heat flux to the cold surface. Because of the scoping nature of the calculations, a relatively coarse grid, 21 by 21, was used to model the 3-m- (out from the surface) by-1-m- (along the surface) flow field. A calculation using a 61-by-61 grid produced results within 2% of the 21-by-21 grid results.

In order to understand the role of the radiation-convection interaction, it is convenient to compare the case with interaction to the case with no interaction. With no interaction (a nonparticipating medium), the region outside the viscous boundary layer is at the free stream temperature. The radiative heat flux incident on the cold surface is equal to the radiative heat flux along the far boundary; in this case, $\alpha T^4_{\text{flame}}$.

The presence of a participating medium results in the cold surface influencing the temperature of the free stream. The radiative heat flux from the far boundary is now affected by the presence of a lower-temperature absorbing/emitting medium. For the case of zero free stream velocity, the magnitude of the reduction in heat flux incident on the cold surface can be estimated with the diffusion approximation if the medium is optically thick. Since fire environments have significant upward velocities, a coupling occurs between the radiation field and the convective flow. The upward convective flow acts to replenish the flow field around the surface with hot fluid at T_{flame}. As a result of the radiation-convection coupling, a radiation boundary layer forms along the surface (Figure 3.10) and extends into the flow field much farther than a typical viscous boundary layer. However, a viscous boundary layer with steep velocity and temperature gradients is still present near the surface in the case with a participating medium.

The results obtained without a combustion source term are presented in Section 3.2.3.1, followed in Section 3.2.3.2 by the results obtained with a combustion source term. The results with no combustion source term are representative of flows with large quenched regions from oxygen or fuel depletion.

3.2.3.1 No Combustion Source Term

The result of interest with no combustion source term is the reduction in radiative heat flux incident on the cold surface from the surrounding flame environment. A surface length of 1 m was used in all the calculations since this is a representative length of the actual test calorimeters. A base case fire environment was selected with the following characteristics: $T_{\text{flame}} = 1100°\text{C}$, free stream velocity = 5 m/s, and absorption coefficient = 1 m^{-1}.

The incident radiative heat flux on the cold surface is shown in Figure 3.11 as a function of surface temperature and position along the 1-m surface for the base case fire environment. A colder surface has a greater influence on the surrounding flame environment, resulting in a greater reduction in the radiative heat flux incident on the surface. As the surface temperature approaches T_{flame}, the radiative heat flux incident on the surface approaches the blackbody radiative heat flux at T_{flame}. The results are also a strong function of location along the surface. Near the leading edge there is little reduction in the incident radiative heat flux relative to the blackbody radiative heat flux at T_{flame}. Near the top of the 1-m surface, the reduction in the incident radiative heat flux is as large as 23%.

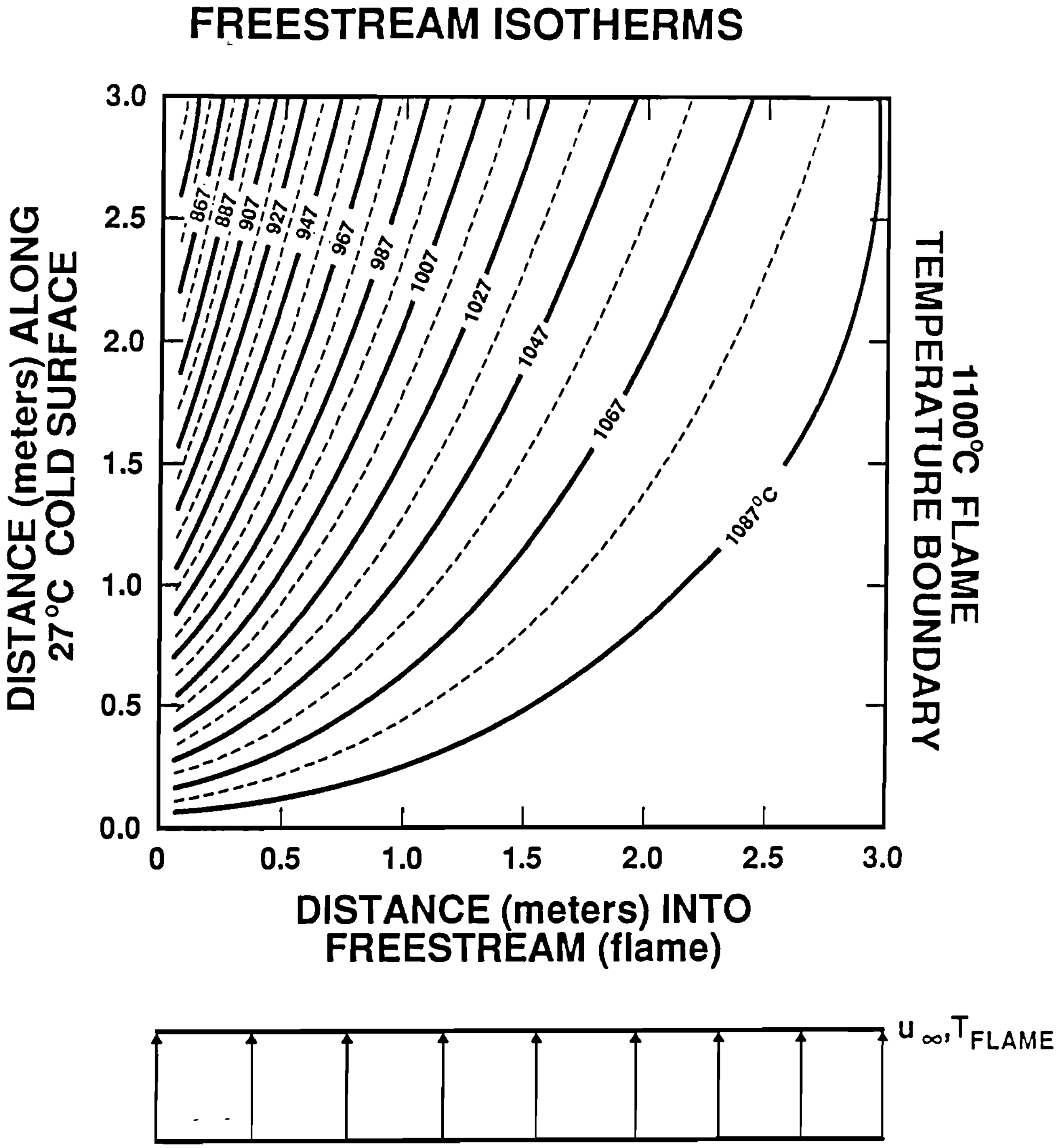

Figure 3.10 Radiation Thermal Boundary Layer Development from Convection-Radiation Interaction

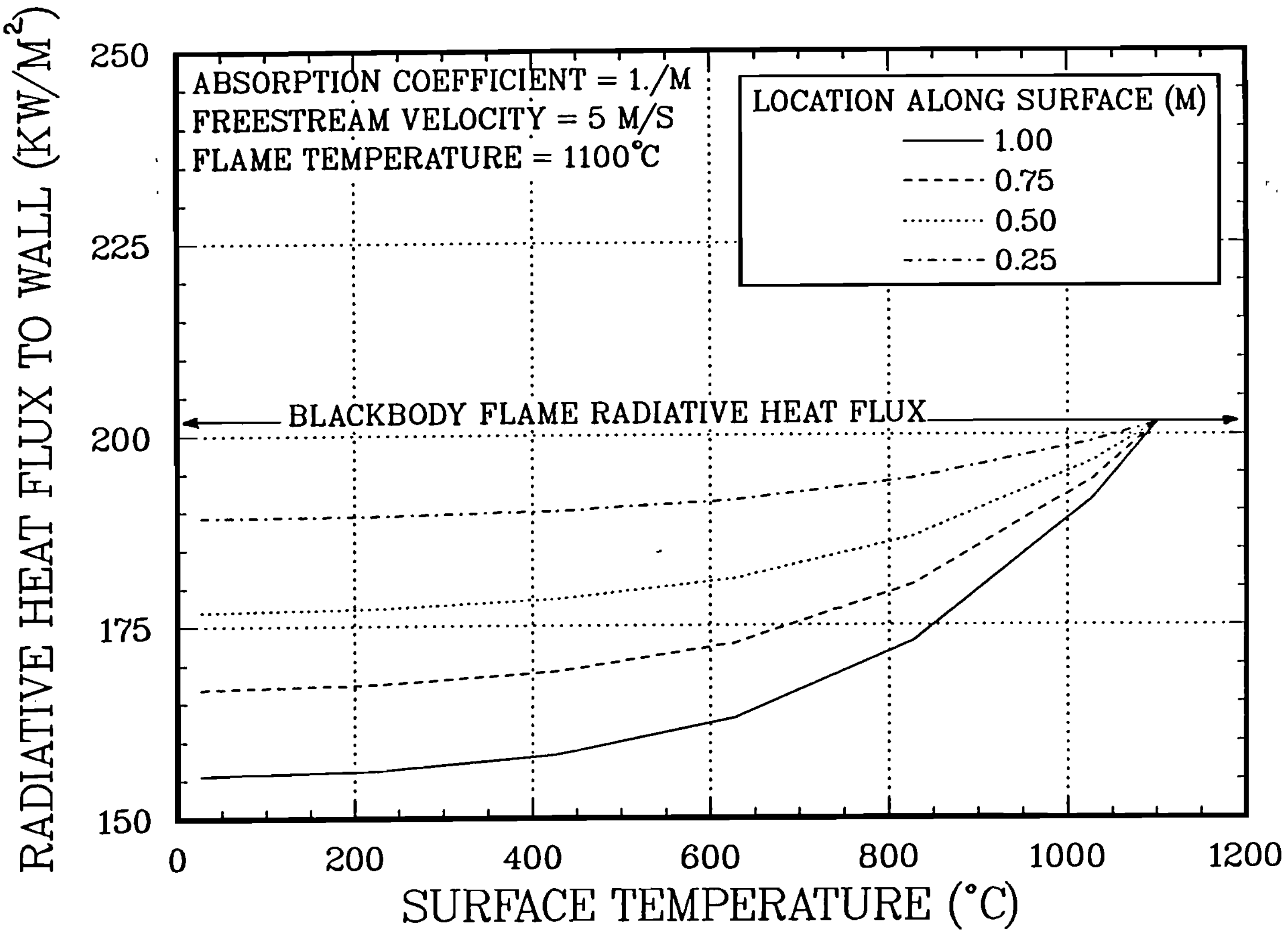

Figure 3.11 Effect of a Cold Surface on Incident Radiative Heat Flux

These results imply that during the transient phase the radiative heat flux incident on a surface in a fire environment can be significantly influenced by the surface temperature. They also imply that calorimeters of differing sizes can indicate different incident radiative fluxes and may not be directly comparable.

A more convenient way to express the results is in terms of the fraction of flame radiative heat flux that is effectively blocked by the participating medium. This fraction is defined as

$$\text{Fraction blocked} = 1 - \frac{\text{Flame radiative heat flux reaching surface}}{\text{Blackbody flame radiative heat flux } \left(\sigma T^4_{\text{flame}}\right)} \qquad (3.6)$$

which can also be viewed as

$$\text{Fraction blocked} = 1 - \text{effective flame emmissivity} \qquad (3.7)$$

where the effective flame emissivity is less than 1.0 as a result of radiative cooling of the combustion gases by the cold surface.

With this definition, the results from Figure 3.11 can be presented as shown in Figure 3.12. The rest of the results will also be given only for the top of the surface, at $L = 1$ m.

In the large pool fires, flames are generally nonisothermal, and flame temperatures typically vary from 900°C to 1100°C. The effect of flame temperature variation is shown in Figure 3.13. Higher flame temperatures result in a higher fraction of heat flux blocked because the effect of the cold surface is more pronounced. However, the incident radiative heat flux reaching the surface [(1 - fraction blocked) $\sigma T^4{}_{\text{flame}}$] is always larger for the higher-temperature flames, as expected.

The experimentally measured gas velocities in large pool fires are a function of elevation above the pool surface. For elevations of from 1 to 2 m, the typical location of test calorimeters, the measured velocities are in the range of from 3 to 7 m/s (Schneider et al., 1988). The effect of free stream velocity on the results is shown in Figure 3.14. Lower velocities result in higher blockage fractions because the fluid has more time to interact with the cold surface before being swept downstream. The limiting case of zero velocity is shown for comparison and agrees well with the diffusion approximation solution (Siegel and Howell, 1981).

The effect of the absorption coefficient on the results is shown in Figure 3.15. Representative absorption coefficient values in the range of from 0.5 m to 10 m^{-1} based on experimental measurements (Longenbaugh and Matthews, 1988) have been used. Various depths out into the free stream were used in the calculations since a lower absorption coefficient implies that a larger depth of fluid is affected. As expected, the results are a strong function of absorption coefficient. This is especially important since in an actual fire environment, the absorption coefficient can exhibit large gradients in the vicinity of a cold surface owing to incomplete combustion, quenching, and soot migration effects.

Several phenomena that have not been included in the model influence the results presented to this point, such as combustion heat sources, viscous boundary layer effects, and turbulent mixing of the free stream. The effects of combustion source terms will be presented in Section 3.2.3.2, and the latter two phenomena will be discussed here.

To investigate the effects of the viscous boundary layer on the radiative heat flux reaching the surface, a "worst case" assumption was made: the fluid in the viscous boundary layer was assigned zero velocity and a temperature equal to the cold wall temperature. This was intended to

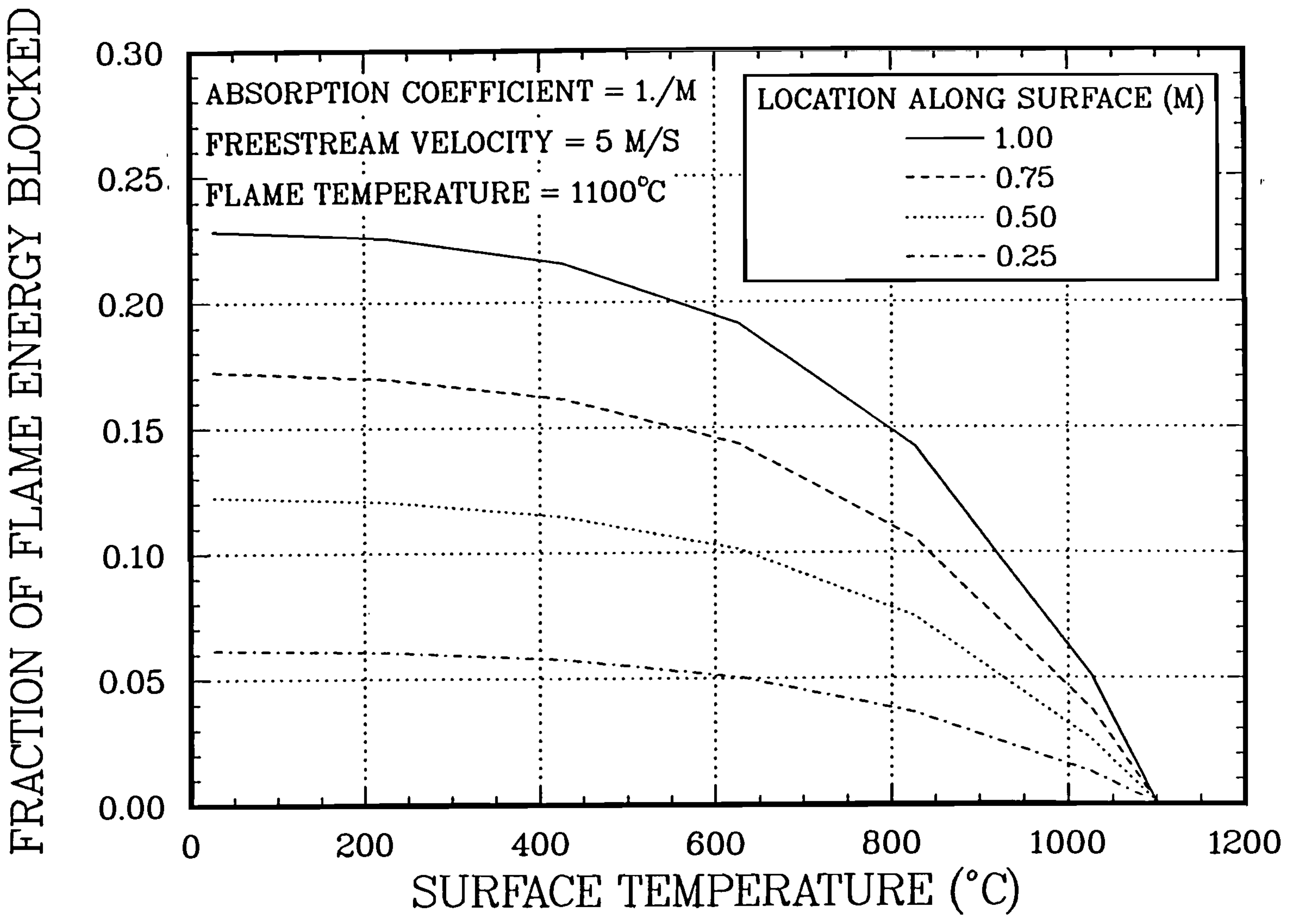

Figure 3.12 Fraction of Flame Radiative Energy Blocked by Participating Medium

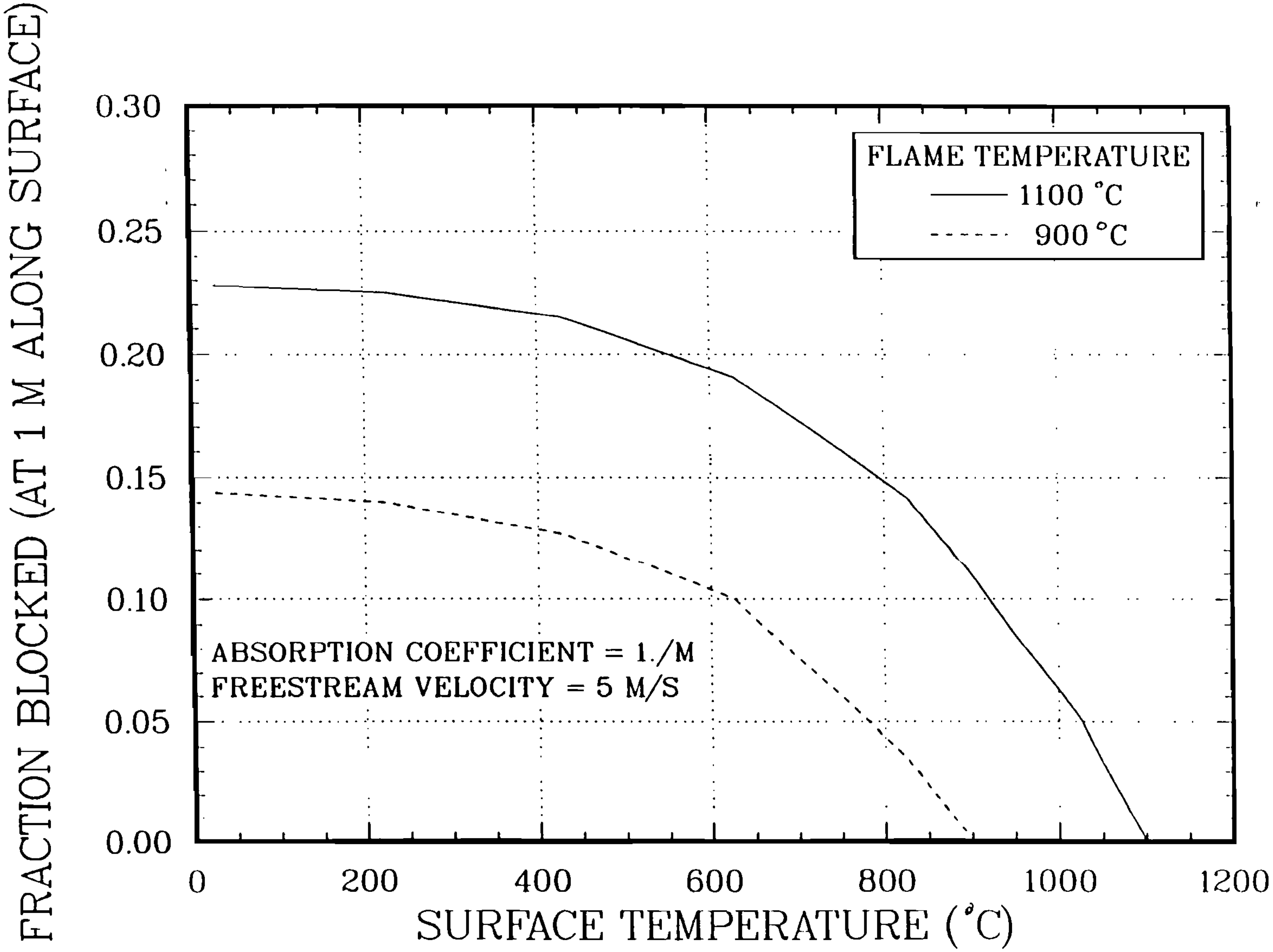

Figure 3.13 Effect of Flame Temperature Variation on Fraction of Energy Blocked

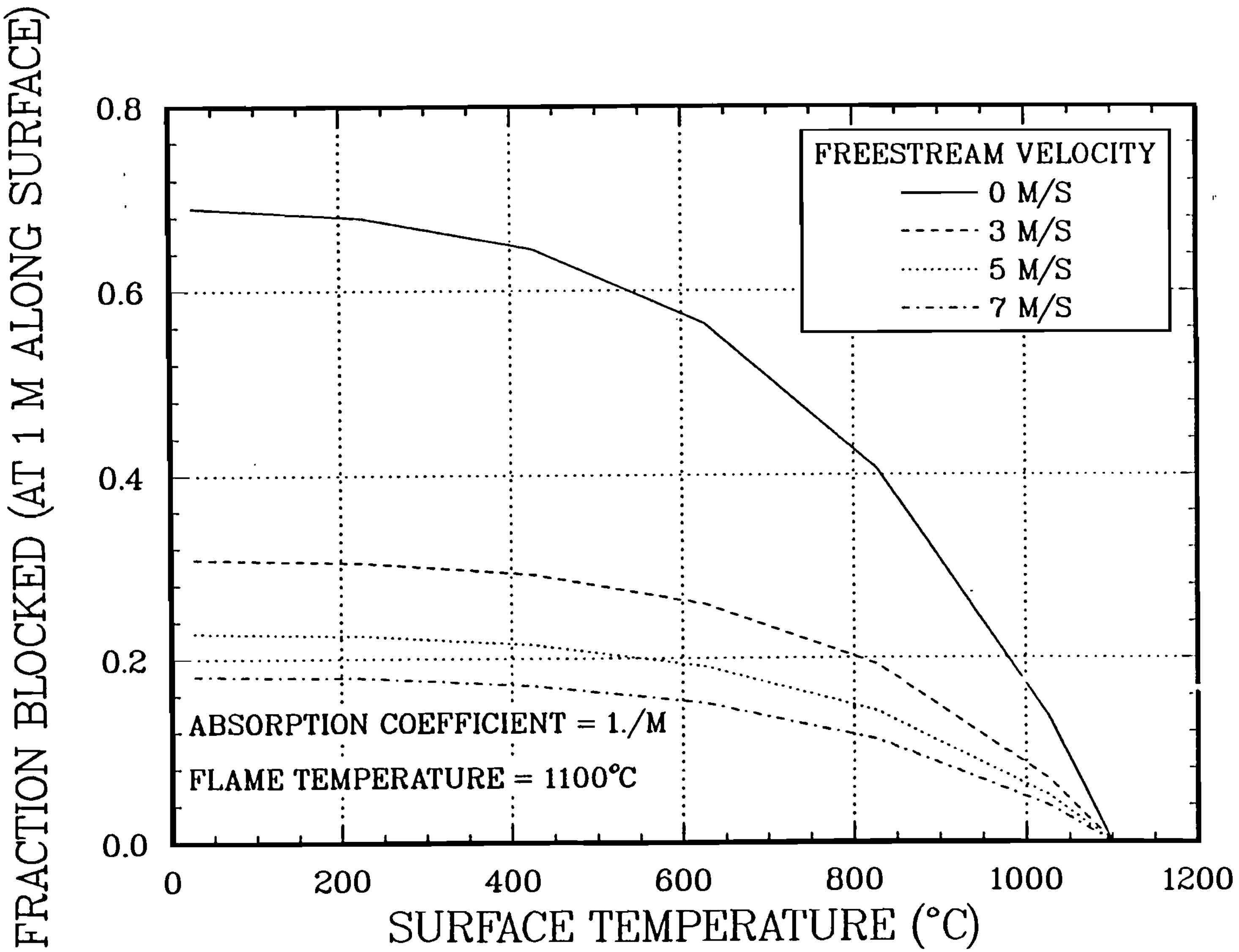

Figure 3.14 Effect of Free Stream Velocity Variation on Fraction of Energy Blocked

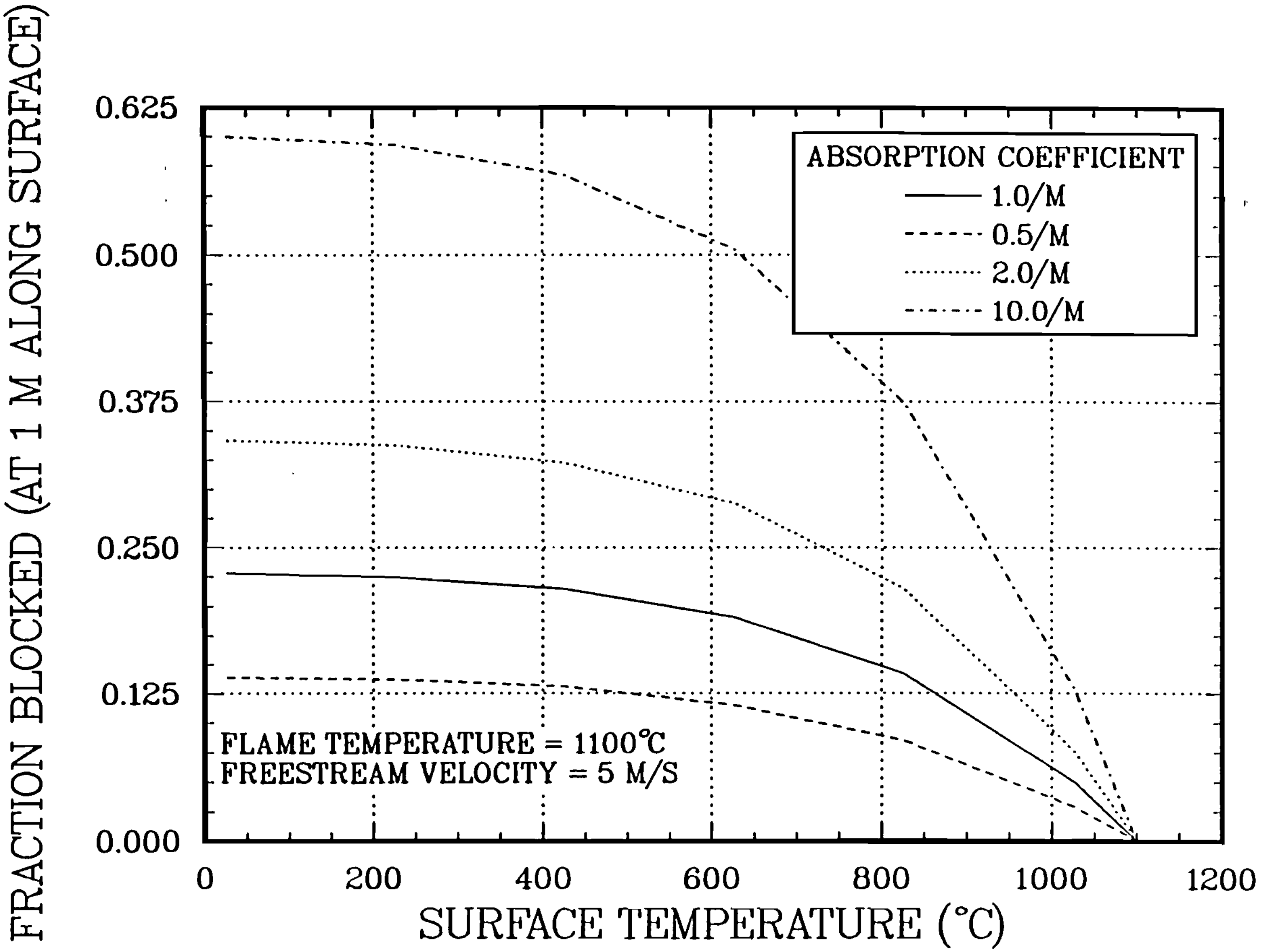

Figure 3.15 Effect of Absorption Coefficient Variation on Fraction of Energy Blocked

provide an upper bound on the radiative flux blockage of the viscous boundary. A 21-by-61 grid was used, with each computational cell being approximately 0.05 m in width. Thus, the layer of cells nearest the surface corresponded roughly to the thickness of the viscous boundary layer. The results of this worst case approximation are compared in Figure 3.16 to a slip boundary condition (no boundary layer). Since values for the effect of a more realistic viscous boundary layer would lie somewhere between the two curves shown in Figure 3.16, it appears that the overall effect on the radiative heat flux reaching the wall is not important in these scoping calculations.

Because large pool fires are highly turbulent, the effect of including turbulent mixing in the free stream was examined. The fluid thermal conductivity, which had been set to zero up to this point, was set equal to 100 times that of air to investigate turbulent transport of energy in the free stream. As Figure 3.17 indicates, such mixing does enhance the effect of the cold surface on the surrounding environment, but the reduction in radiative heat flux is not large. Thus, neglecting turbulent mixing in these calculations appears justified.

3.2.3.2 With a Combustion Source Term

The influence of combustion on radiative heat flux was determined by incorporation of a uniform source term in the energy equation. Although admittedly the estimation of combustion source term strength is simplistic (see Section 3.2.2), it does allow investigation of the magnitude of the effect. All else being equal, the inclusion of a uniform combustion source term should reduce the blockage effect compared to no source term, because the source of radiative heat flux is distributed nearer the cold surface. However, a direct comparison of these results to those without a combustion source term should probably not be made because the boundary conditions for each case are different.

The initial temperature of the fluid must be specified at the leading edge of the surface. A temperature of from 827° to 927°C was selected based on experimental data at an elevation of 1 m (Schneider et al., 1988). The results indicate a weak dependence on initial temperature (Figure 3.18). In general, the magnitude of the fraction of radiative heat flux blocked by the participating medium is somewhat lower than for the base case with no combustion source term.

Figure 3.19 shows the effect of free stream velocity variations on the radiative flux with a combustion source term. The trend is similar to the results with no combustion source term.

The combustion source term strength was varied by a factor of 2, since its magnitude is not well known. Figure 3.20 indicates that higher combustion source strength results in a larger fraction of heat flux blocked. The reason is that the larger source term yields higher flame temperatures, and so the results are consistent with those shown in Figure 3.12. The higher flame temperatures cause larger radiative heat fluxes to reach the surface in spite of the increase in the blockage fraction, also shown in Figure 3.12.

One test was run to investigate the effects of a locally varying combustion source term in which Arrhenius-type, or exponential, behavior was assumed. The results (Figure 3.21) show a substantial increase in the fraction of the heat flux that is blocked by the participating medium, slightly exceeding 30% at a distance of 1 m along the surface. In this calculation, the fluid at the far boundary heats up owing to the combustion source term. Very little combustion occurs in the fluid near the cold surface because of the influence of the cold surface and the exponential variation in source term with temperature. These results indicate that knowledge of the source strength distribution is crucial in estimating the radiative heat flux that reaches the surface.

The results presented above generally indicate that reductions in heat flux of from 15 to 40% are possible from the influence of a cold surface on the surrounding fire environment. The experimentally measured reductions in heat flux shown in Figures 3.7 and 3.8 fall within this range, with reductions in peak heat fluxes of 20 and 3[illegible]%, respectively. A strict comparison

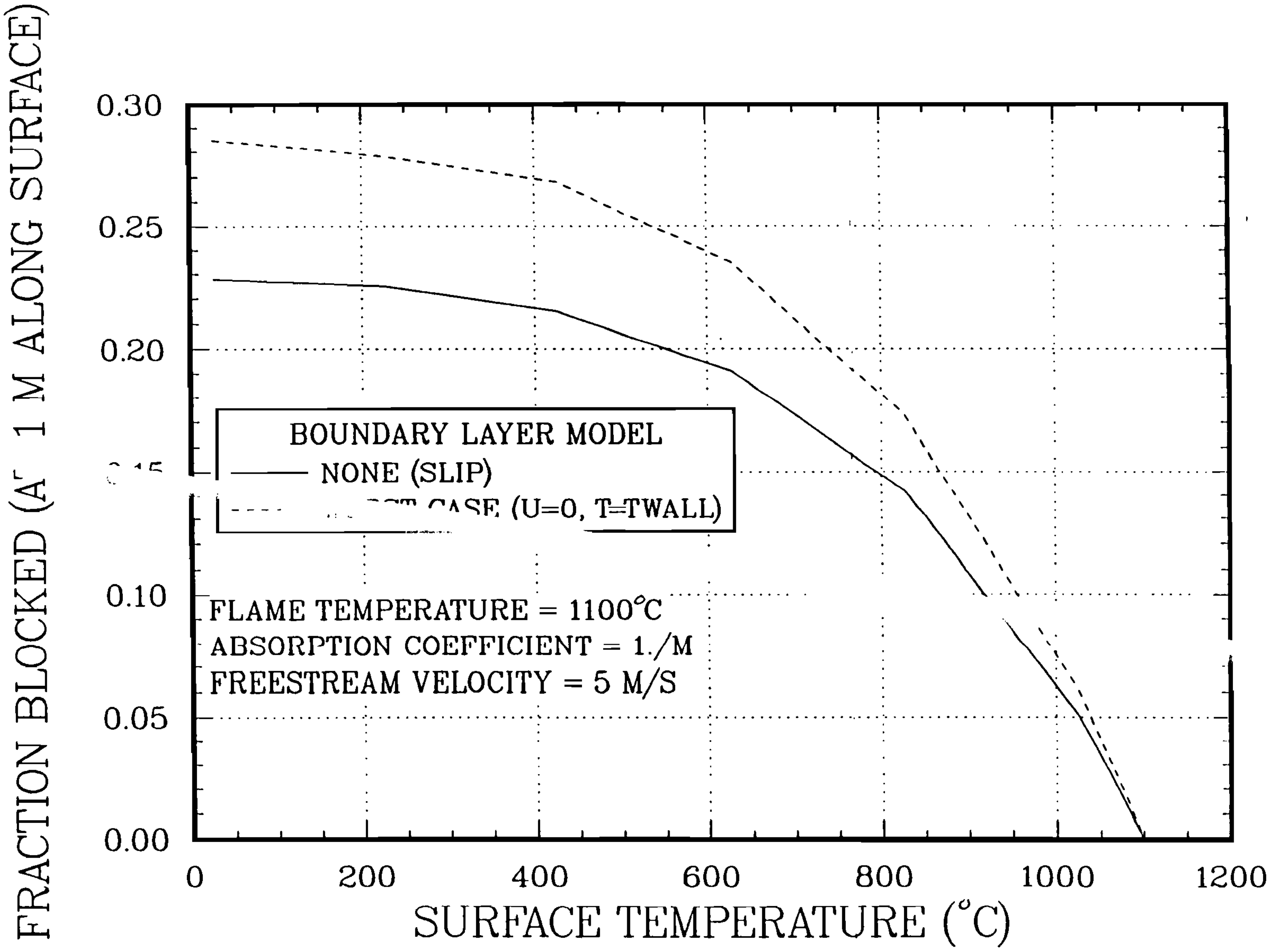

Figure 3.16 Worst Case Viscous Boundary Layer Effect on Fraction of Energy Blocked

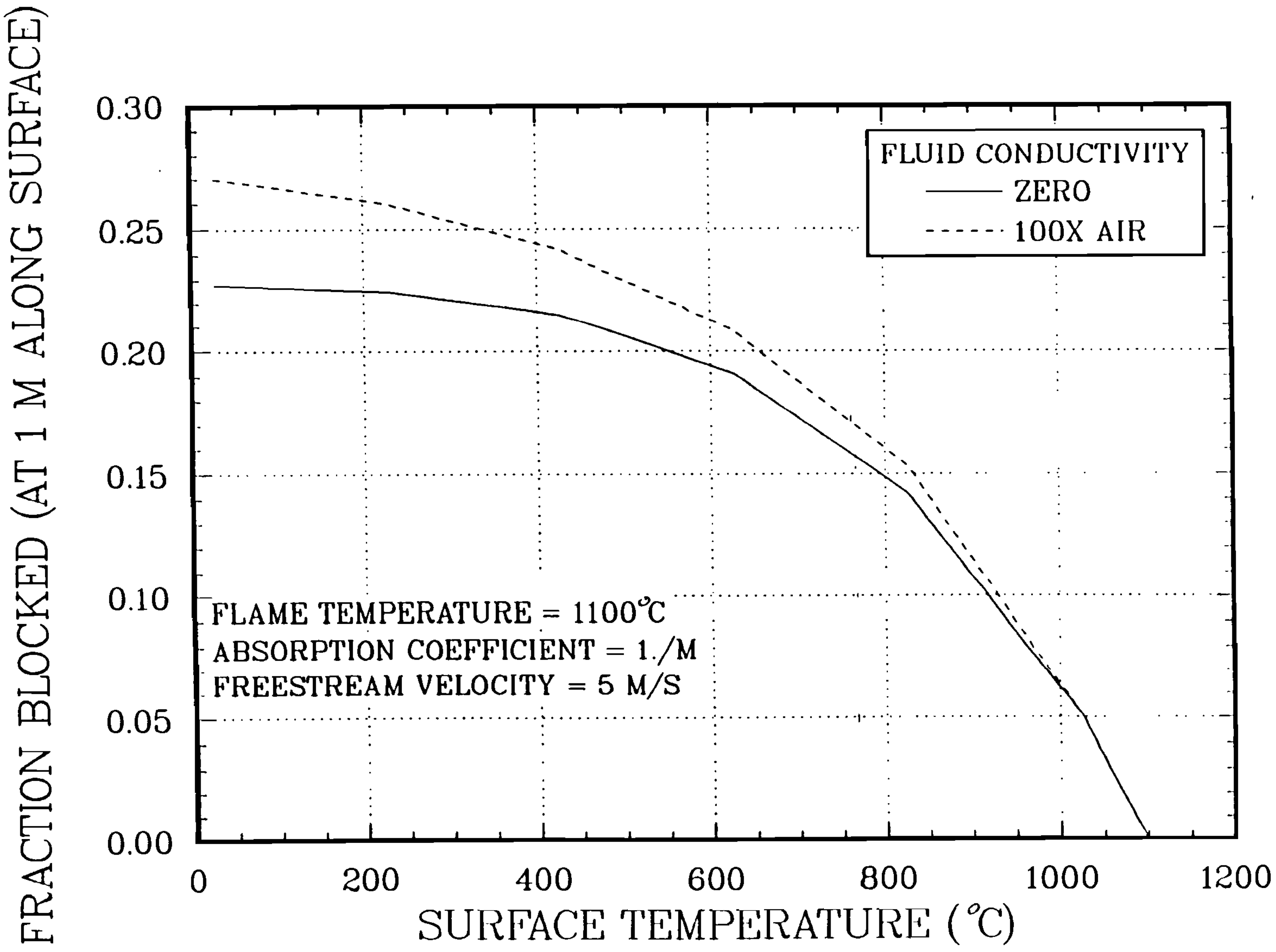

Figure 3.17 Turbulent Mixing Effect on Fraction of Energy Blocked

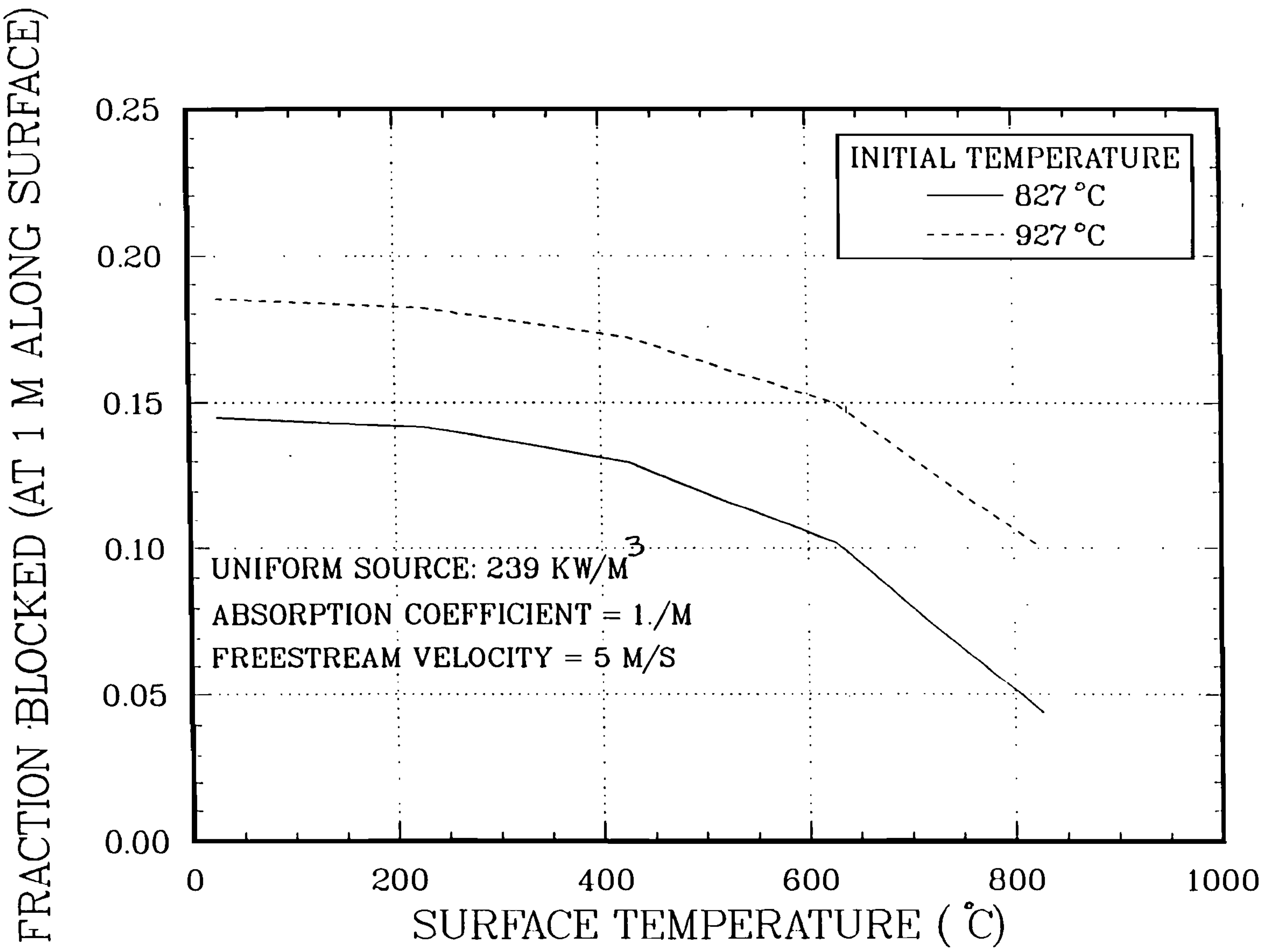

Figure 3.18 Effect of Initial Temperature Variation on Source Term Results

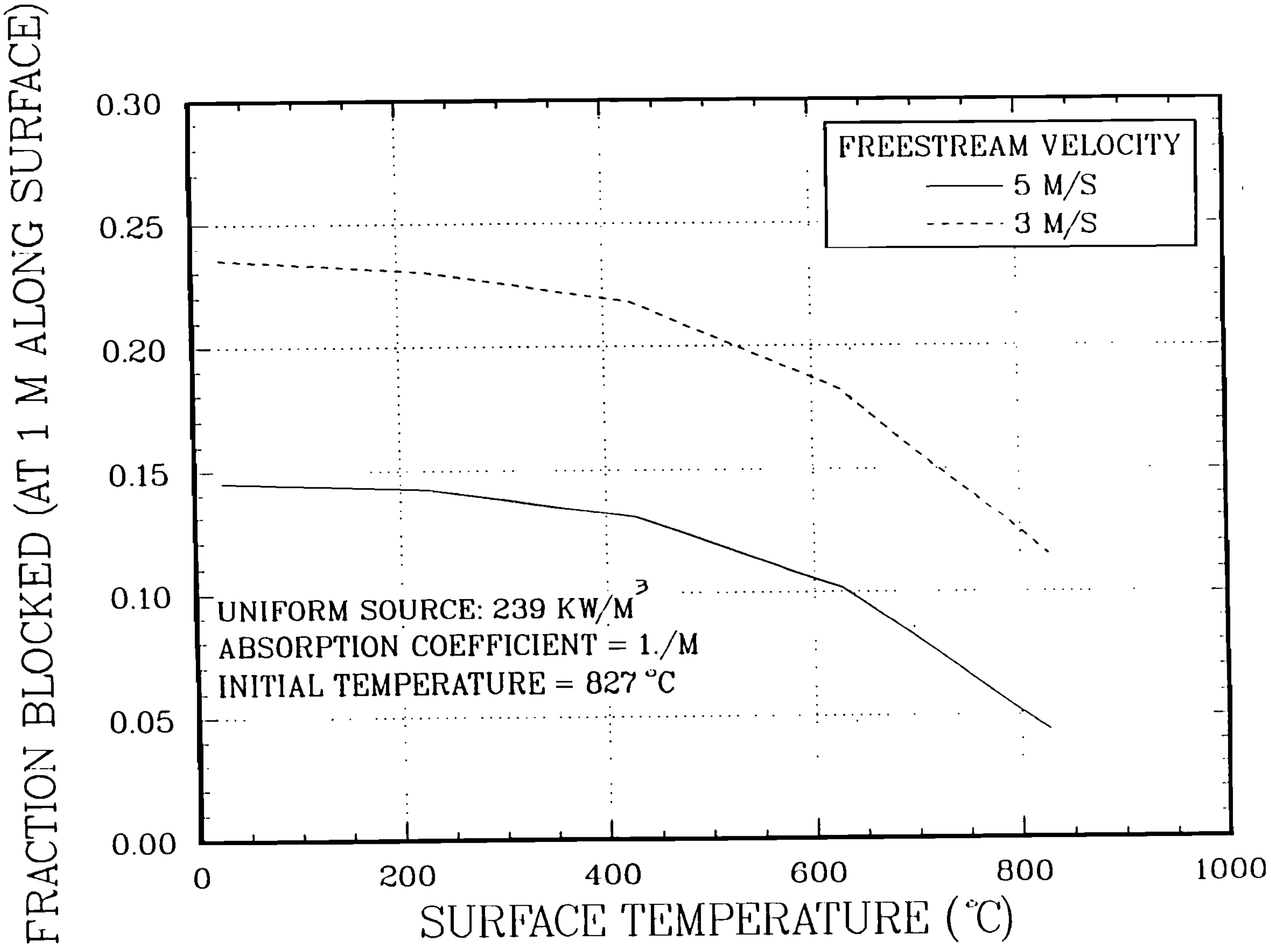

Figure 3.19 Effect of Free Stream Velocity Variation on Source Term Results

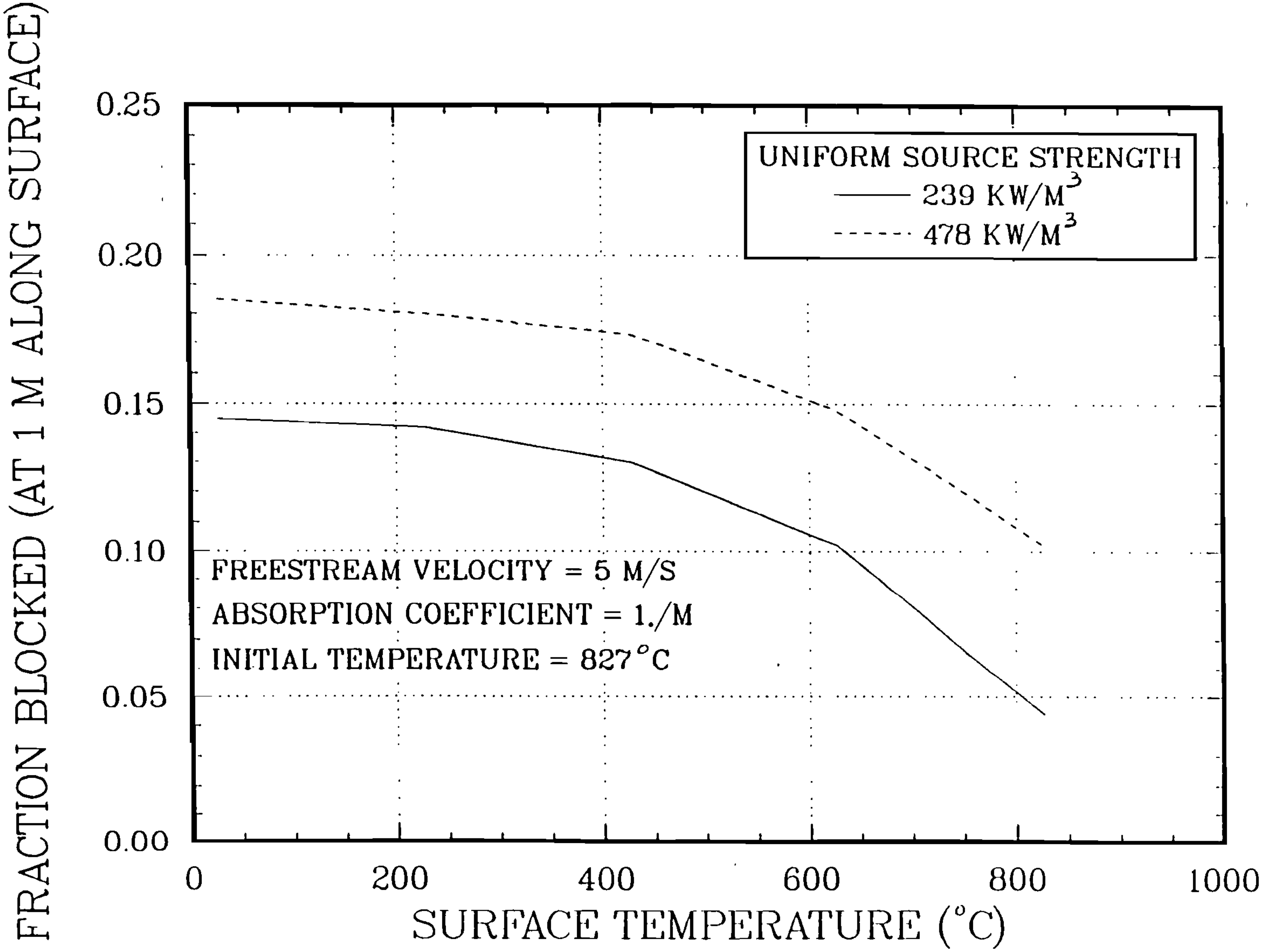

Figure 3.20 Effect of Source Strength on Source Term Results

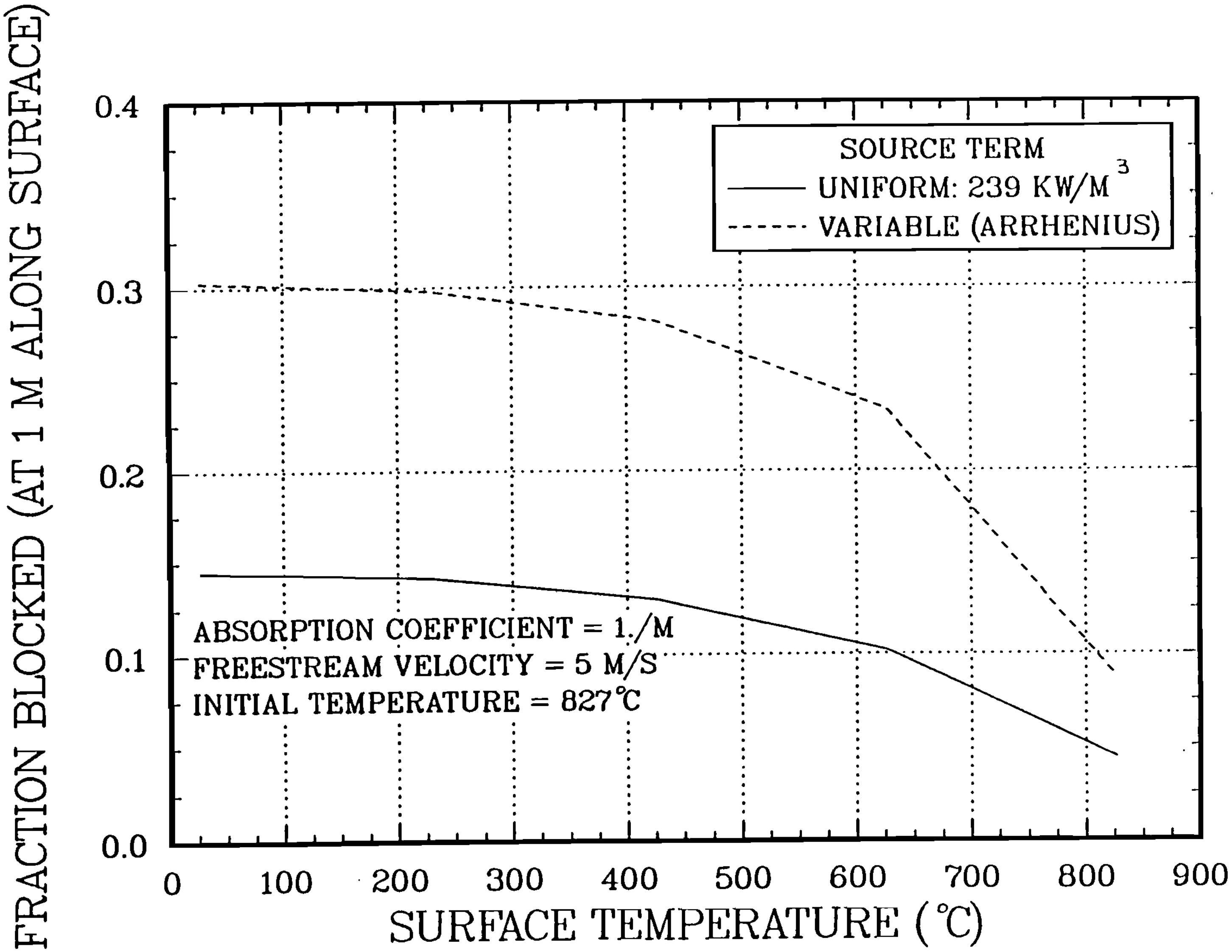

Figure 3.21 Results with Arrhenius-Type Source Term

between the data and the model results is not possible because of the difference in geometries. However, the model results show the same trends and are of the same magnitude as the experimentally measured phenomena, indicating that the model successfully captures the important physics of the problem.

4.0 CONCLUSIONS

The work discussed in this report was intended to develop boundary conditions for use in predicting the response of objects engulfed in a fire. The behavior of fires is difficult to predict owing to the influence of ambient conditions, such as winds, and the object's presence in the fire. This study helped to identify those characteristics of fire that are not well understood and forms the basis for work currently under way in the area of pool fire characterization. This report presents a significant accumulation of fire test data; details a comparison of furnace, pool fire, and simulated fire tests; describes an interpretative model developed to explain the observed heat flux mapping on thermally massive objects; and examines the effects of two different regulations designed for different applications and purposes. The report should not be considered an end point on the subject but rather as a compilation of work completed thus far and of knowledge gained from these efforts.

4.1 Conclusions from Recent Fire Test Data Analyses

Section 2.2 provides an assessment of data from recent fire tests that included several experiments designed to study heat transfer in fires and evaluate the adequacy of instrumentation. The following conclusions can be drawn from these data:

1. The cold wall heat flux to both sides of the plate calorimeter rose from the bottom of the plate calorimeter to an elevation of about 3.6 m above the pool floor, then began to drop with increasing height. The location of maximum heat flux on the plate calorimeter was higher than the location of the maximum flame temperature in the fire. The maximum flame temperature average occurred at about 2.2 to 2.3 m above the floor. This behavior was observed only for the vertical plate calorimeter and may not appear with other geometries. The differing heights measured for the maximum flame temperature location and the maximum heat flux may be related to participating medium effects discussed Section 3.2.

2. The cold wall heat flux to the 1.4-m-diameter cylindrical calorimeter was slightly lower (10%) on the bottom compared to the top, in contrast to earlier work, in which the bottom received a higher flux than the top. The west side of the calorimeter received about the same flux as the top. Possible explanations for these contradictory results are the different locations of the calorimeters in the pool and different wind conditions, but the results indicate the variability of actual fire environments.

3. Transpiration radiometer data proved to be useful measurements. With these measurements, incident radiative heat flux to the plates could be accurately determined and flame emissivity estimated. With the flame emissivity values, the total, radiative, and convective heat flux contributions with time could be calculated. This information showed that overall, the convective part of the total heat flux in pool fire tests is typically about 10 to 20% but could be a significant part, up to 50%, during the early stages of the fire.

4. Front face temperature measurements are not necessary if back face temperature measurements are available, because the SODDIT inverse heat conduction code can be used to calculate the front face values. The agreement between the calculated values from SODDIT and the measured values from both sheathed thermocouples and pencil-probe eroding thermocouples is very good. This implies that high-frequency changes in the fire environment are probably not important for massive casks, since this information does not propagate through the cask wall.

4.2 Conclusions from the Analyses of the DOT/NRC Environmental Comparison Test Series

A series of tests was conducted to compare the 10 CFR 71 and 49 CFR 179 regulatory thermal environments. The 10 CFR 71 regulation provides specifications for the analytic demonstration that a Type B radioactive material transport cask is likely to survive a severe fire accident without release of contents through any pathway. These analytic specifications are intended to ensure that the cargo within the Type B cask is protected and remains isolated from the environment. The 49 CFR 179 regulation provides performance criteria for the thermal protection system for tank railcars designed for the transport of flammable and/or toxic hazardous gases and liquids. The criteria state that tank cars shall be equipped with a thermal protection system that prevents release of any of the car's contents, except through safety relief valves, when subjected to a pool fire for 100 min and a torch fire for 30 min. With rail shipments, larger quantities (in tank-car-size loads ranging from 9,500 to 35,000 gallons) of flammable materials are potentially available in adjacent tank cars, much larger than could occur in truck transportation. This potential has apparently driven the FRA to consider a 100-min pool fire duration in 49 CFR 179, rather than the 30-min duration specified in 10 CFR 71. Justification of the fire times requires investigation of various accident scenarios with the tools of risk assessment, and lies beyond the scope of this report. Clarke et al. (1987) discuss the duration and intensity of fires for both truck and rail transport. The same report concludes that only a small percentage of transportation accidents involve fire. Fortunately, the thermal boundary conditions for fully engulfing fires reported herein are equally applicable for all modes of transportation and fire duration.

The following points can be made on analysis of the comparison tests.

1. The hot wall heat flux curve for the thick wall calorimeter fire test in the SWISH facility has a different shape from that of the other curves for the same calorimeter in the radiant heat facility. This difference may be due to the larger portion of the total incident heat flux that convection contributed for the SWISH test compared to the radiant heat tests done with electric lamps (Nakos and Keltner, 1989). Convection is expected to be less than 5% of the total flux in the radiant heat tests.

2. For both fire tests in the SWISH facility, the radiative portion of the flux is smaller than would be expected in a fully engulfing fire with an optically thick flame. Convection is unaffected by flame thickness. Convection, which is driven by the difference in temperature between the surface of the test unit and the surrounding gas, is more important when the surface is cold relative to the gas and becomes less important as the test unit surface temperature approaches that of the gas.

3. In the thin-wall calorimeter SWISH fire test, the surface temperature of the calorimeter rose very quickly. The radiation shield was 670°C within 3.5 min of the start of the test. For the thin-wall calorimeter, the convective component of the total heat flux becomes small very quickly. Because the surface of the thick-wall calorimeter heats much more slowly, the convective component remains significant for a longer time during the test.

4. These tests cannot be used to determine the effect of the test unit and fire environment interaction because the differing amount of air supplied to the fire for each test adds an uncontrolled variable in the SWISH facility tests. This effect will be controlled when the Smoke Minimization Experiment Research Facility (SMERF) with variable speed fans becomes operational.

4.3 Conclusions from the Comparison of Predicted Versus Actual Calorimeter Thermal Data

In Section 3.0 the measured responses of the plate and cylindrical calorimeters with analytic predictions were compared. These comparisons were used to assess the adequacy of the analytic models available for these types of thermal environments.

1. SODDIT is an inverse conduction code that can be used to predict surface temperatures when the back face temperature and applied heat flux are known. To compute the convective contribution to the applied heat flux, the free stream gas temperature must be known. Good agreement between measured and predicted surface temperature was found when the measured flame temperature was used as the free stream gas temperature. This result is significant since a universally accepted location where the free stream temperature is to be measured has not been defined.

2. When the TRUPACT II tests were used as a comparison, the actual convective heat transfer coefficient could be estimated by adjusting it to obtain better agreement with measured responses. If the flame emissivity is assumed to be 0.82, a convective coefficient of 57 W/m^2-°C during the fire and 11 W/m^2-°C after the fire generated good agreement. This approach to characterizing the response of a cask during a fire is not predictive since test article and fire environment specific measured data were required to identify the convective coefficients. The study demonstrated that if data on convective coefficients from an independent source are available, a good prediction of the response can be made.

4.4 Conclusions on the Influences of Cold Surfaces on a Fire Environment

The results of large pool fire tests indicate that calorimeters of different size and thermal mass will measure significantly different incident heat fluxes in the same fire. In this part of the report an analytic, one-dimensional, gray gas radiation heat transfer model was developed that can be used to interpret pool fire measurements and explain observed temperature and heat flux distributions. The following conclusions can be drawn from this model:

1. The results of modeling the radiation in the vicinity of a vertical plate indicate that cold surfaces influence the surrounding flame environment to an appreciable extent, reducing radiative heat transfer from the flames. The reduced radiative heat transfer is a function of local surface temperature, flame temperature or source strength, free stream velocity, characteristic length of the test fire article, and the volumetric absorption coefficient. The analytic model shows that thermally massive objects cool the gas region adjacent to the surface, reducing the volumetric emission from the flame. This behavior is transient and diminishes as surface temperature increases. Because the model is interpretive, it cannot be used to predict the behavior of a cask in a fire, but it does explain the behavior observed with thermally massive objects in pool fires. Development of predictive models for pool fire analyses is currently under way.

2. The characteristics of the cask, fire, and surrounding gas affect the temperature field of the fire and the heat flux from the fire to the cask. Since these variables must enter into proposed models or correlations of experimental data, it appears that in general a simple flame temperature or heat flux boundary condition will not provide a correct condition for predicting transport cask response to a fire environment. Work continues in the area of fire characterization to develop models that can provide a reasonable analysis tool for predicting the response of casks engulfed in fires.

4.5 Overall Conclusions

Test object response characteristics and several fire variables including fire size, height and orientation of the object's surface above the pool, and wind effects led to the wide range of thermal boundary conditions documented in this report. This wide variation in fire boundary conditions has led regulators to base regulations principally on empirical test results and experience.

Direct comparison of 49 CFR 179 and 10 CFR 71 regulations is difficult because they are aimed at different purposes and based on different experience. The 10 CFR 71 regulation implicitly specifies the detailed surface temperature vs. heat flux requirements for the test of an entire shipping container, while 49 CFR 179 provides rules that implicitly fix the heat flux emitted from a test torch. The torch is then used to test a section of a railroad tank car thermal protection system. The fact that the fire environments for NRC and DOT regulations are different in both duration, intensity, and allowed release is a reflection of differing regulatory history and industry practice, and should not be a cause for concern. The true test of these requirements is the fact that both regulations have been successful in achieving safe transportation of the affected hazardous materials.

Also note that "actual" fires during transportation accidents differ in duration, size, geometry, and intensity. To achieve the level of conservatism that designers and regulators will accept, a boundary condition that represents conditions that are typical of severe accident conditions is needed. Fully engulfing fires, those that are so large that any surface of an object "sees" only smoke and combustion gases at fire temperature, not cooler materials outside the fire, is one part of the specification of such a boundary condition. Also note that this is an extremely demanding boundary condition for an object as large as a railcar and is unlikely to be achieved in most fires, although it has occurred in accidents without radioactive materials in the train consist. Estimated duration of fires is discussed elsewhere in this report; for example, results from the Clarke et al. report support the current maximum 30-min test fire duration typically used for truck cargoes, and the 100-min maximum fire duration used for testing of thermal protection systems for railcars with flammable or certain hazardous materials.

The possibility of a 100-min fire duration in rail accidents exists as reported by Clarke et al. Since the purpose of this report is to relate results from pool fire experiments and summarize the thermal conditions measured in the fires, no evaluation of the frequency of the 100-min fire is provided. With the results of this report and other information, a risk assessment should be performed quantifying the potential usefulness of safety improvements such as train consists that exclude bulk quantities of flammable and/or oxidizing materials. Comparison of those risks with other acceptable risks could indicate the need for revision of regulations covering shipment of high-level radioactive materials by rail.

In the case of 10 CFR 71, designers of packages that are to be tested in large pool fires must be aware of the variability of thermal boundary conditions reported for large fires and must design accordingly. Total heat absorbed and fire temperatures may be similar for both calculations based on the regulatory simulation and in actual fires, but the possible local variability of heat fluxes must also be considered during design. The data in Tables 2.5 and 2.6 are useful in assessing the magnitude of such local variations.

The results reported in Section 2 of this report may be used as a starting point for estimating thermal boundary conditions for container designs. For example, Figure 4.1 shows average cold wall heat flux values for large and small calorimeters in large fires from Tables 2.5 and 2.6. The figure also shows peak heat fluxes from SWISH experiments from Figures 2.25 and 2.26. The calorimeter results on the right side of the figure illustrate the differing object response for large and small calorimeters. Small calorimeters typically receive higher initial heat fluxes than the larger calorimeters. Causes for these differences are related to the effects that cold walls have on

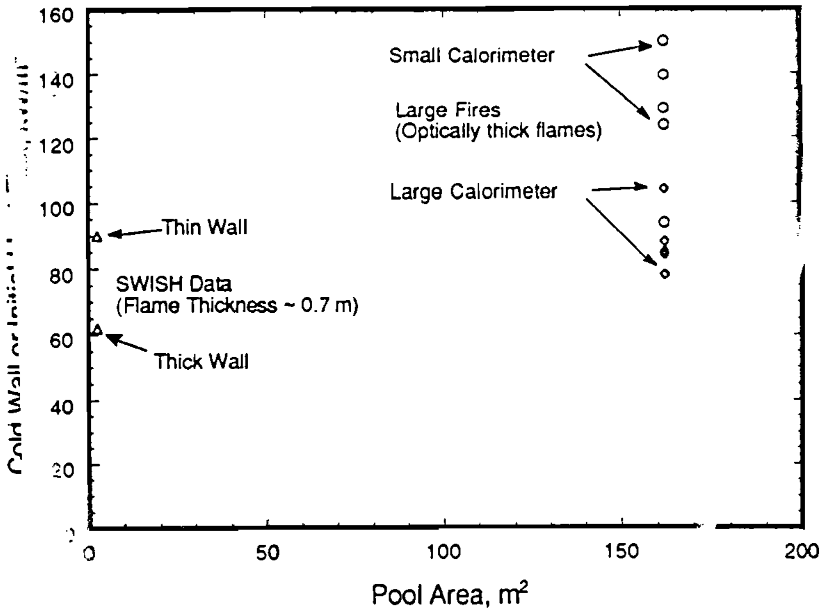

Figure 4. S mary of Cold Wall and Initial Heat Fluxes fr m Tables 2.5 and 2.6, and Fi es 2.25 and 2.26

radiation in participati edia as discussed in Section 3.0. For t e SWISH tests, the flames are less optically thick, ag esulting in a lower overall heat flux lev l.

Initially, the concept of wall heat flux was introduced into t s report as an aid to unifying data from both large and sm st objects in different fires. The col wall heat flux was also intended to be used as the initial heat fl or thermal boundary conditions. Data analysis has shown that even with this unifying concept, a variation in thermal boundary conditions is still observed. To aid in understanding this variab , radiation heat transfer concepts involving a participating medium such as a gray gas were introduce n Section 3.0. These concepts point the way toward better simplified models of the large fire e ronment, and active research in this area is being pursued.

The report results indicate at in deciding the thermal boundary conditions to be applied to a package design, the size of e fire and the object must both be considered. The cold wall heat flux values shown in Figure 4.1 ay be considered to be a starting point in deciding typical conditions. For example, for a large, m sive container, an initial heat flux in the range of 80 to 100 kW/m^2 appears appropriate. This h t flux would decrease as the object surface temperature increased. For a first approximation, a ^{4} radiative flux combined with convection could be used to estimate the heat flux, q'', with an eq ation of the form

$$q'' = F_{1-2}\varepsilon_s\varepsilon_f\sigma(T_f^4 - T_s^4) + h_s(T_a - T_s) \qquad (4.1)$$

where F_{1-2} is the appropriate adiation view factor from the surface to the fire environment (usually unity for convex surf ces in a fully engulfing fire), ε_s is the surface emissivity of the container, ε_f is an effective fl me emissivity that may be used to adjust the initial heat flux into the range desired for analysis, σ the Stefan-Boltzman constant, T_f is the effective flame temperature, and T_s is the obje t wall temperature. The last term is the convective term where h_s is the convective film coefficient and T_a is the ambient gas temperature, usually taken to be equal to the effective flame temperature. Flame temperatures, T_f , may also be estimated from data presented in Section 2.0 and summarized in Figure 4.2. For test articles that typically have surfaces located 1 to 2 m above the pool fire, local flame temperatures in the 900 to 1000°C range were measured. Approximate values for convective film coefficient, h_s, could be taken from the discussion in Section 3.1, or from standard convective correlations.

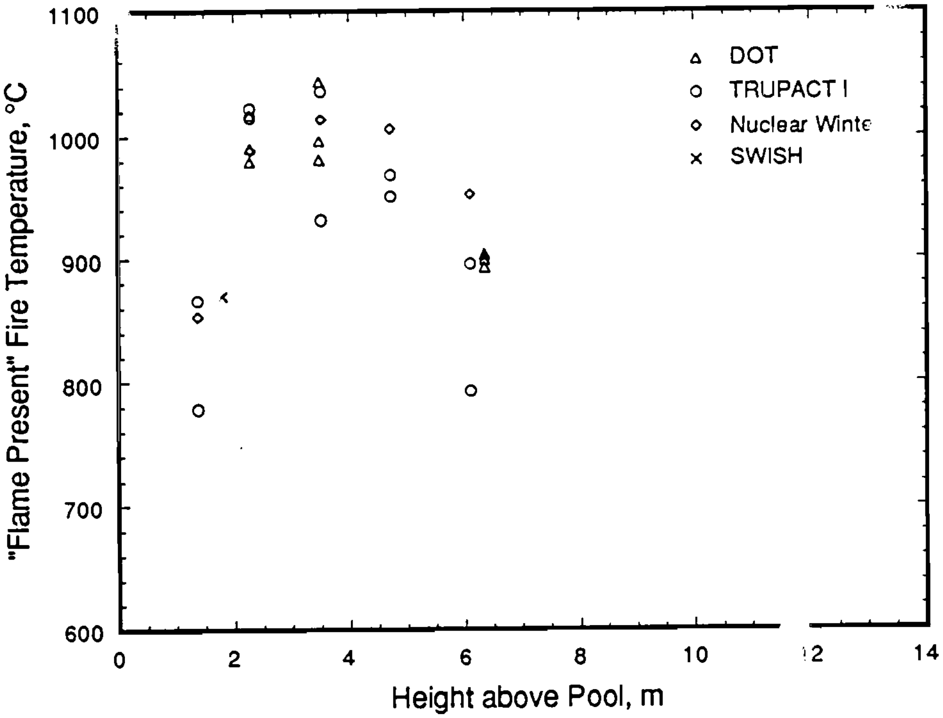

Figure 4.2 "Flame Present" Temperature Data From Table 2.3. SWISH data is from Section 2.3.4 and represents temperatures controlled by varying inlet air quantities.

5.0 REFERENCES

Birk, A. M., and P. H. Oosthuizen, "Model for the Prediction of Radiant Heat Transfer to a Horizontal Cylinder Engulfed in Flames," ASME paper 82-WA/HT-52, 1982.

Blackwell, B. F., R. W. Douglass, and H. Wolf, "A User's Manual for the Sandia One-Dimensional Direct and Inverse Thermal (SODDIT) Code," SAND85-2478, Sandia National Laboratories, Albuquerque, NM 1987.

CFR (U.S. Code of Federal Regulations), Title 49, "Transportation," Part 179, "Specifications for Tank Cars," U.S. Government Printing Office, Washington, DC, 1986.

CFR (U.S. Code of Federal Regulations), Title 10, "Energy," Part 71, "Packaging and Transportation of Radioactive Material," U.S. Government Printing Office, Washington, DC, 1984.

Clarke, R. K., J. T. Foley, W. F. Hartman, and D. W. Larson, "Severities of Transportation Accidents," SLA-74-0001, Vol. I-IV, Sandia National Laboratories, Albuquerque, NM, 1976.

Cooper, L. Y., and D. W. Stroup, "Thermal Response of Unconfined Ceilings Above Growing Fires and the Importance of Convective Heat Transfer," *Journal of Heat Transfer*, Vol. 109, No. 1, pp. 172-178, 1987.

Fry, C. J., "A Consideration of Some Simple Models for Assessing Heat Transfer to Objects Engulfed in Pool Fires," AEE Winfrith, AEEW-M 2321, Winfrith, GB, 1985.

Gregory, J. J., N. R. Keltner, and R. Mata, Jr., "Thermal Measurements in Large Pool Fires," Heat and Mass Transfer in Fires, ASME-HTD, Vol. 73, 1987a.

Gregory, J. J., R. Mata, Jr., and N. R. Keltner, "Thermal Measurements in a Series of Large Pool Fires," SAND85-0196, Sandia National Laboratories, Albuquerque, NM, 1987b.

Keltner, N. R., R. U. Acton, and W. Gill, "Evaluating the Hazards of Large Petrochemical Fires," SAND90-2593C, Sandia National Laboratories, Albuquerque, NM, 1990.

Keltner, N. R., R. Mata, Jr., J. J. Gregory, L. A. Kent, and M. E. Schneider, "Diagnostics from an Open Pool Fire Test of TRUPACT-I," Internal Memorandum, Sandia National Laboratories, Albuquerque, NM, 1987.

Keltner, N. R., K. B. Sobolik, and J. L. Moya, "Heat Transfer in Severe Accident Simulations," presented at the Ninth International Symposium on the Packaging and Transportation of Radioactive Materials, June 11-16, 1989, Washington, DC.

Kent, L. A., "Data Report on Pool Fire Tests of the DOT/FRA Calorimeters," Sandia National Laboratories, Albuquerque, NM, 1988.

Longenbaugh, R. S., and L. K. Matthews, "Experimental and Theoretical Analysis of the Radiative Transfer Within a Sooty Pool Fire," SAND86-0083, Sandia National Laboratories, Albuquerque, NM, 1988.

Mata, R., Jr., and N. R. Keltner, "Test Report on the Full-Scale Fire Test of the PNC Truck Transportation System," Test Report, Sandia National Laboratories, Albuquerque, NM, 1984.

Matthews, L., R. Longenbaugh, and R. Mata, Jr., "Transpiration Radiometer in Fire Characterization," Intech, ISA, August 1986.

Mihalovich, G. S., M. Hudson, B. J. Joseph, and L. E. Romesberg, "Data Report TRUPACT-I, Unit 0," SAND85-1695, Sandia National Laboratories, Albuquerque, NM, 1985.

Moya, J. L., and N. N. Brown, "Thermal Analyses of a Generic Rail Cask Model and Thermal Response of a Test Article Using Different High-Temperature Boundary Conditions," *Proceedings of the 9th International Symposium on the Packaging and Transportation of Radioactive Materials (PATRAM '89),* June 11 through 16, 1989, Washington, DC, CONF-890631, Oak Ridge National Laboratory, Oak Ridge, TN, p. 316.

Nakos, J. T., and N. R. Keltner, "The Radiative-Convective Partitioning of Heat Transfer to Structures in Large Pool Fires," Heat Transfer Phenomena in Radiation, Combustion, and Fires, ASME-HTD, Vol. 106, 1989, Book No. H00498.

Nelson, J. M., "Determination of Net Heat Fluxes and Assessment of Test-to-Test Thermal Input Variation for Three Large Engulfing Open Pool Fire/Calorimeter Tests," SAND85-1821, Sandia National Laboratories, Albuquerque, NM, 1986.

Russell, L. H., "Quantification of the Heat Transfer Parameters Relevant to a Cylinder Immersed in a Large Aviation Fuel Fire," M.S. thesis, University of Pittsburgh, 1970.

Russell, L. H., and J. A. Canfield, "Experimental Measurement of Heat Transfer to a Cylinder Immersed in a Large Aviation-Fuel Fire," *Journal of Heat Transfer*, Vol. 95, No. 3, pp. 397-404, 1973.

Schneider, M. E., N. R. Keltner, and L. A. Kent, "Thermal Measurements in the Nuclear Winter Fire Test," SAND88-2839, Sandia National Laboratories, Albuquerque, NM, 1988.

Siegel, R., and J. Howell, *Thermal Radiation Heat Transfer*, 2nd ed. (New York: Hemisphere Publishing Company, 1981), p. 513.

Tunc, M. M., and A. Karakas, "Three-Dimensional Formulation of the Radiant Heat Flux Variation on a Cylinder Engulfed in Flames," *Journal of Heat Transfer*, Vol. 107, No. 4, pp. 949-953, 1985.

Wong, S., and F. R. Steward, "Radiative Interchange Factors Between Flames and Tank Car Surfaces," *Journal of Hazardous Materials*, Vol. 20, pp. 137-146, 1988.

Appendix

Additional Figures

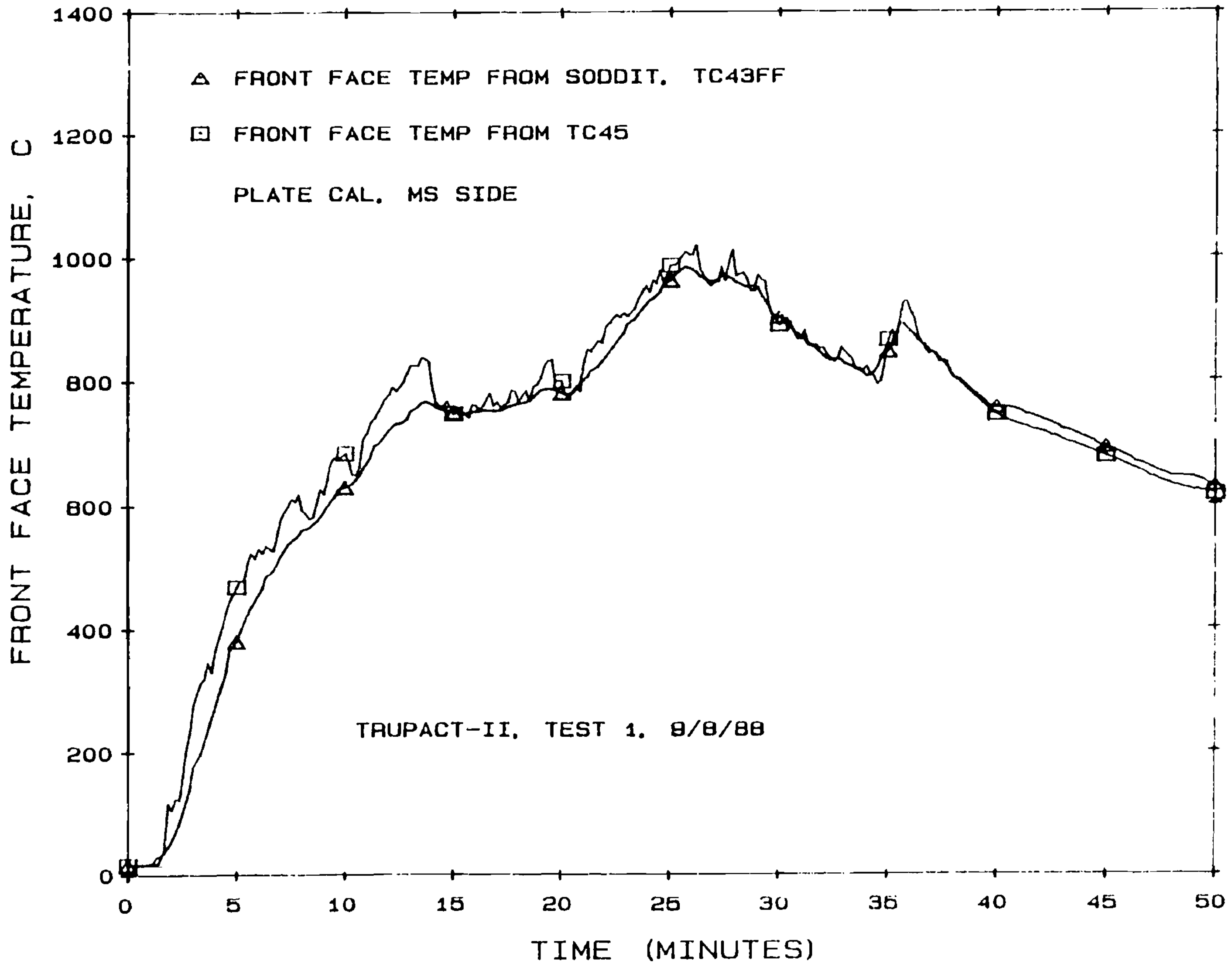

Figure A.1 Measured Versus Calculated Temperatures on the Mild Steel Side of the Plate Calorimeter

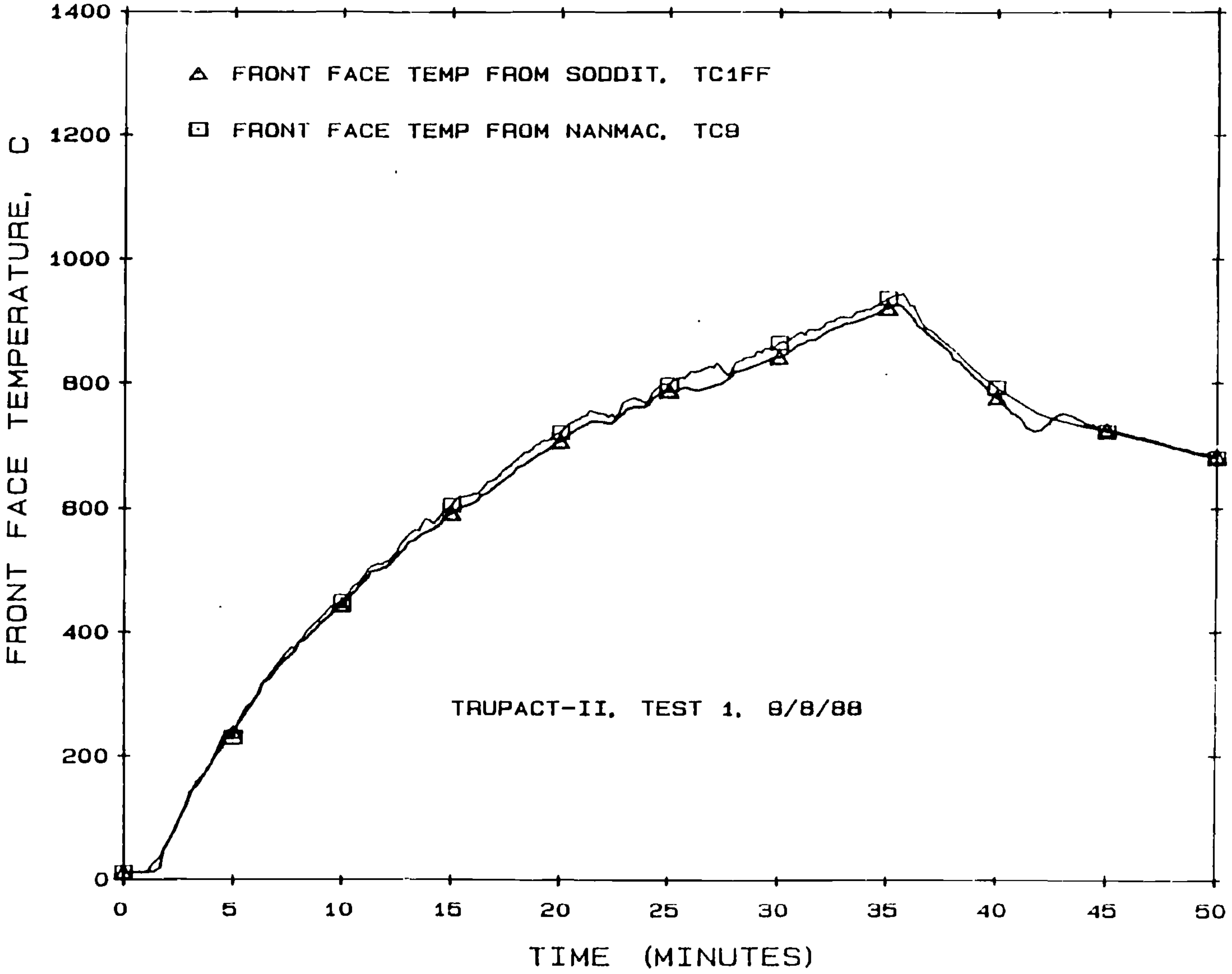

Figure A.2 Measured Versus Calculated Temperatures on the Top of the 1.4-m-Diameter Calorimeter

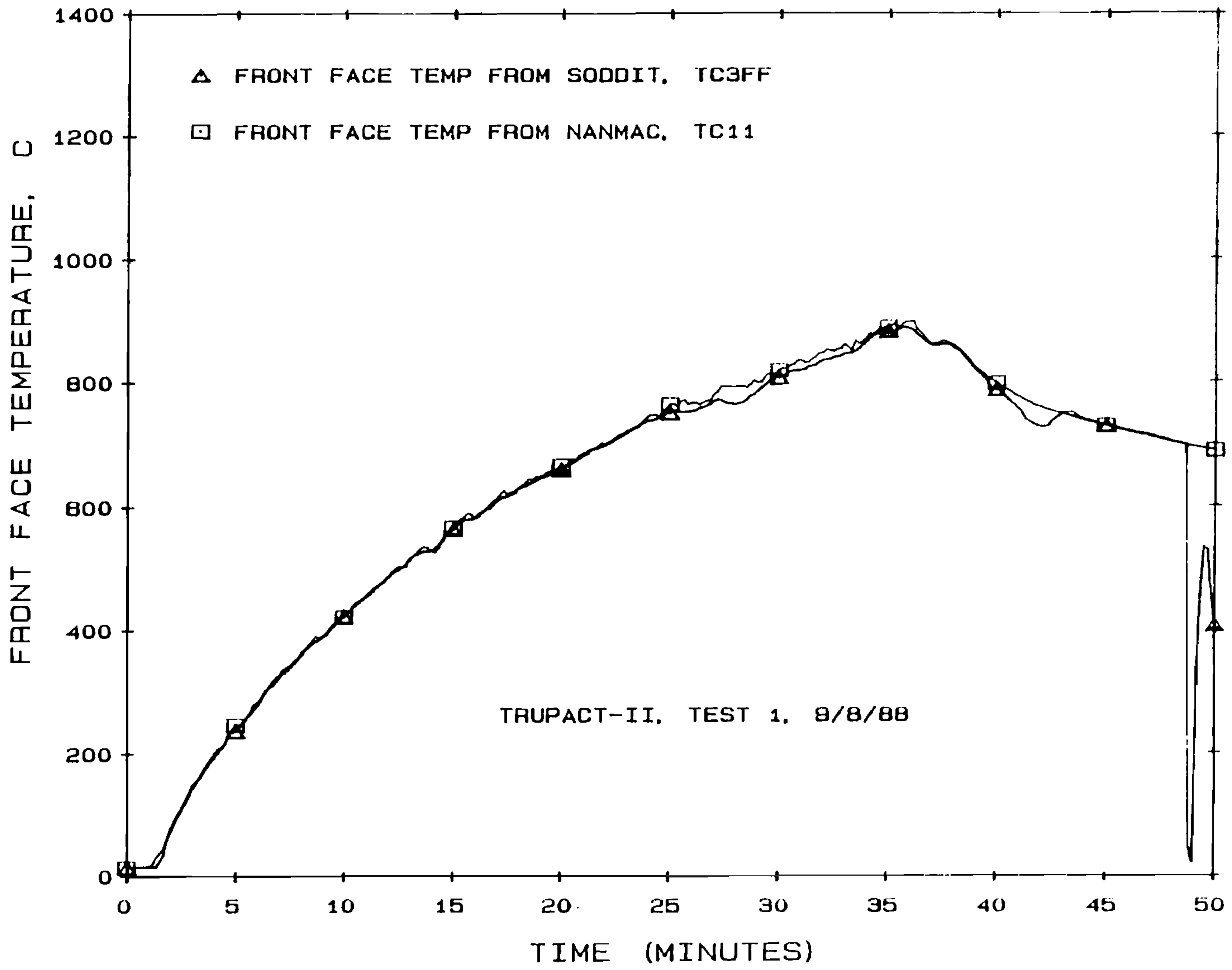

Figure A.3 Measured Versus Calculated Temperatures on the Bottom of the 1.4-m-Diameter Calorimeter

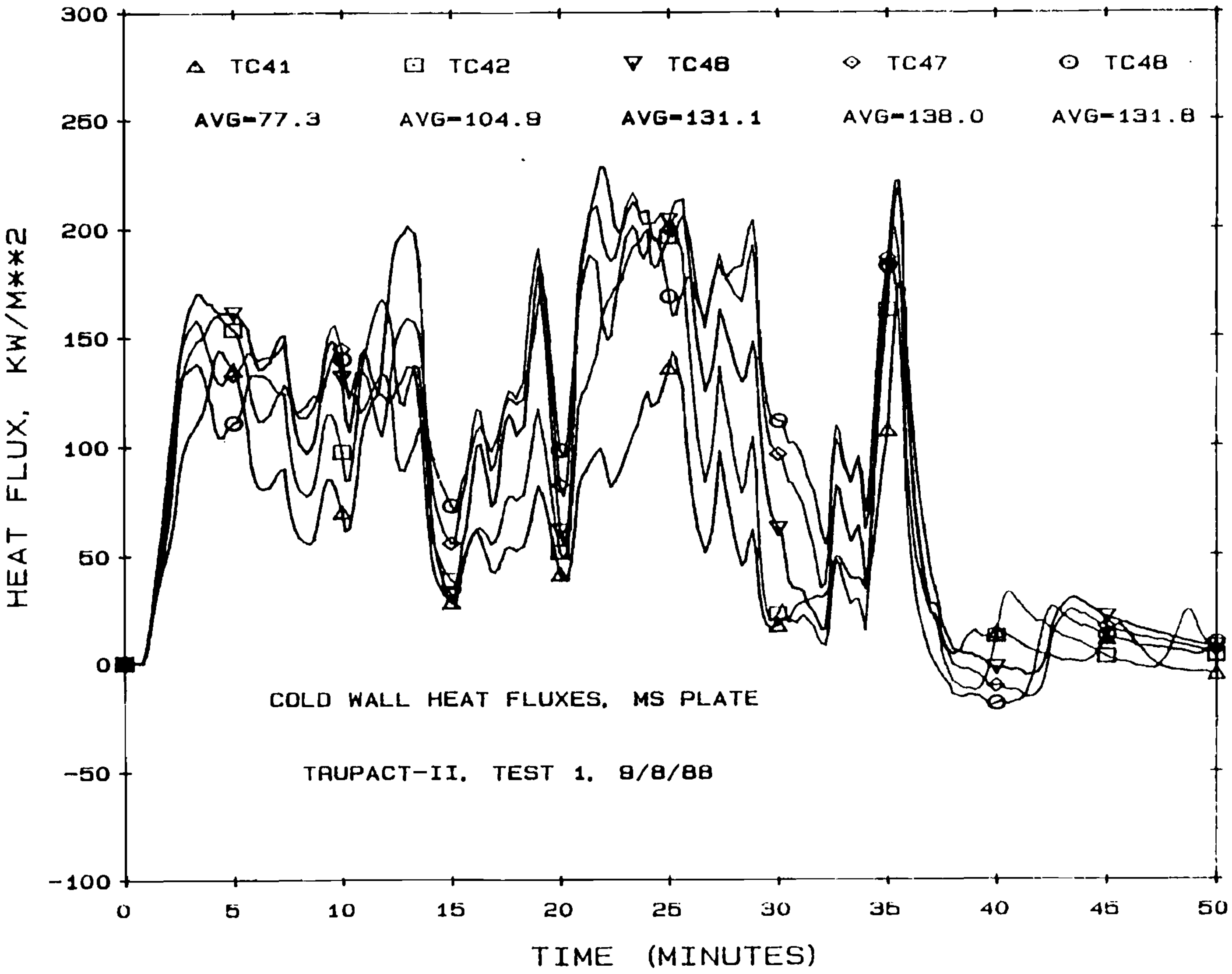

Figure A.4 Cold Wall Heat Fluxes on the Mild Steel Side of the Plate Calorimeter

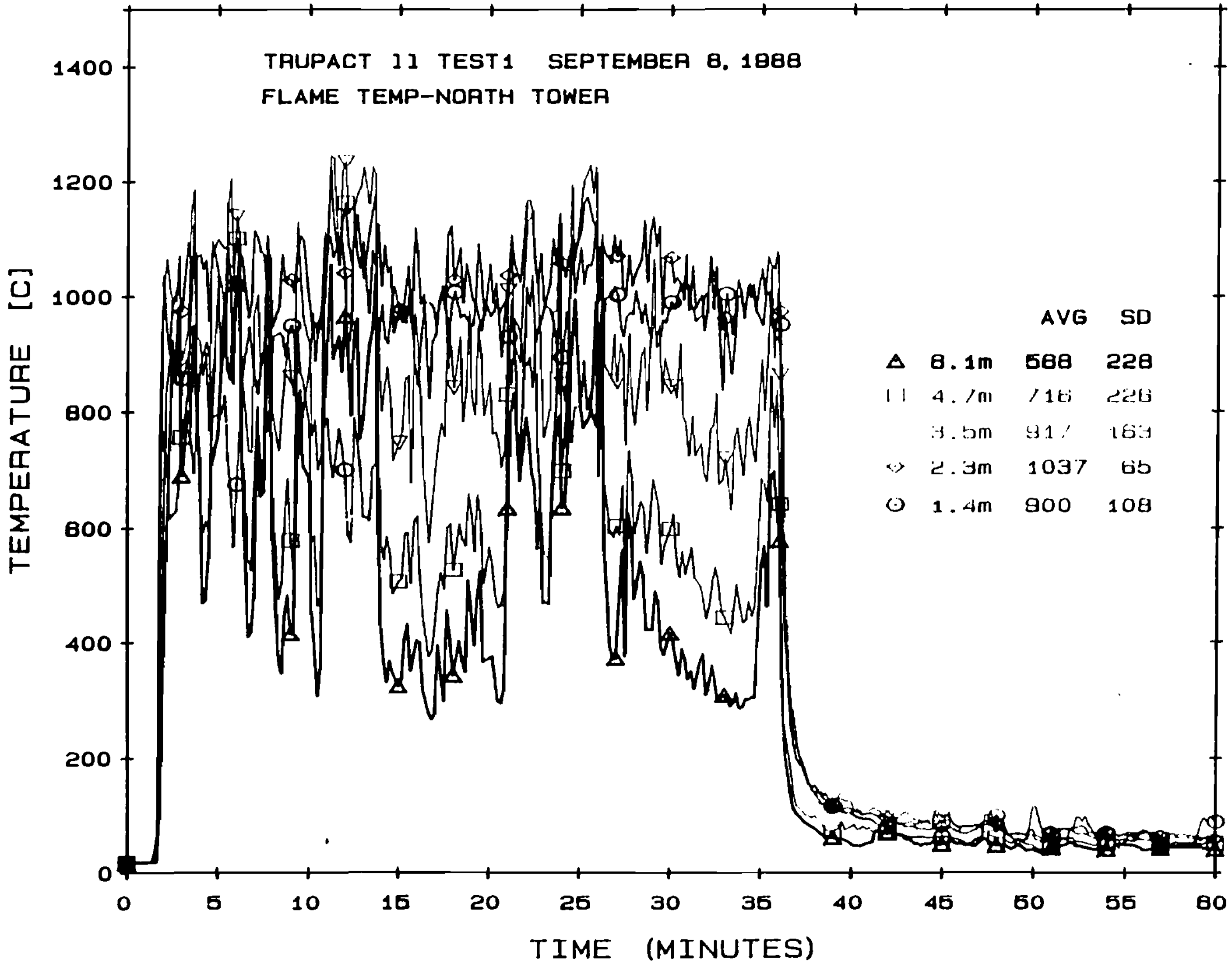

Figure A.5 Flame Temperatures on the North Tower

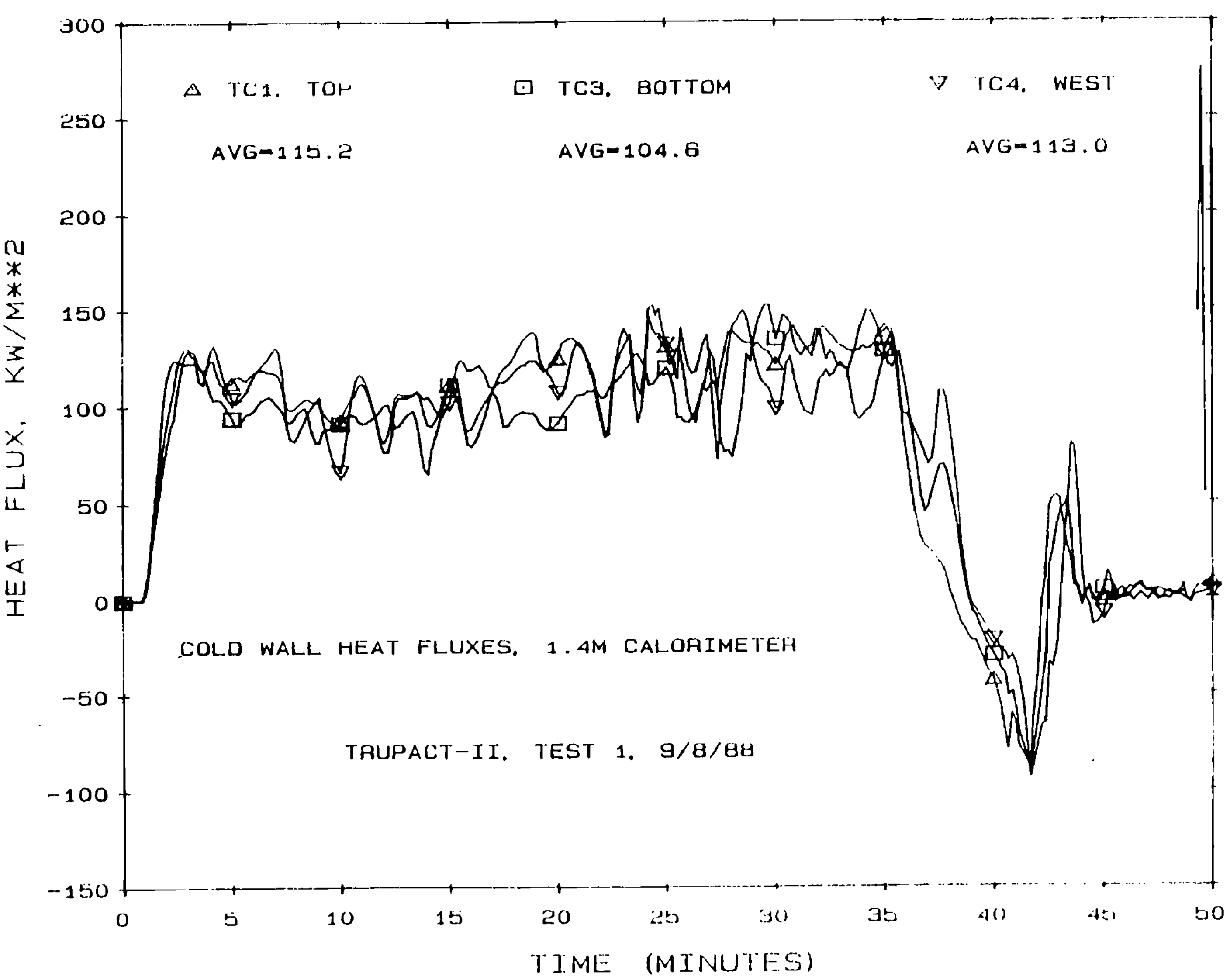

Figure A.6 Cold Wall Heat Fluxes on the 1.4-m Calorimeter

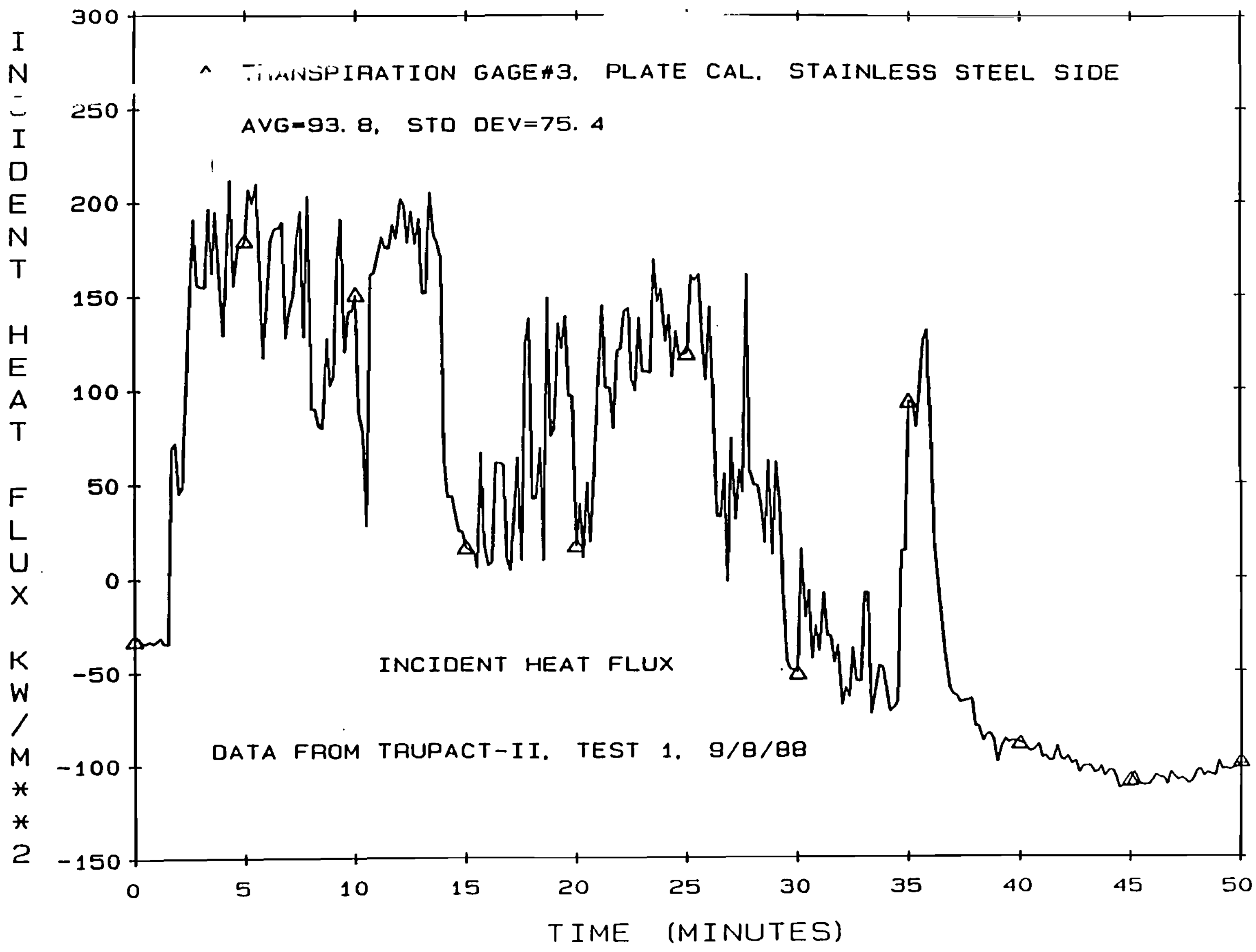

Figure A.7 Incident Heat Flux on the Stainless Steel Side of the Plate Calorimeter

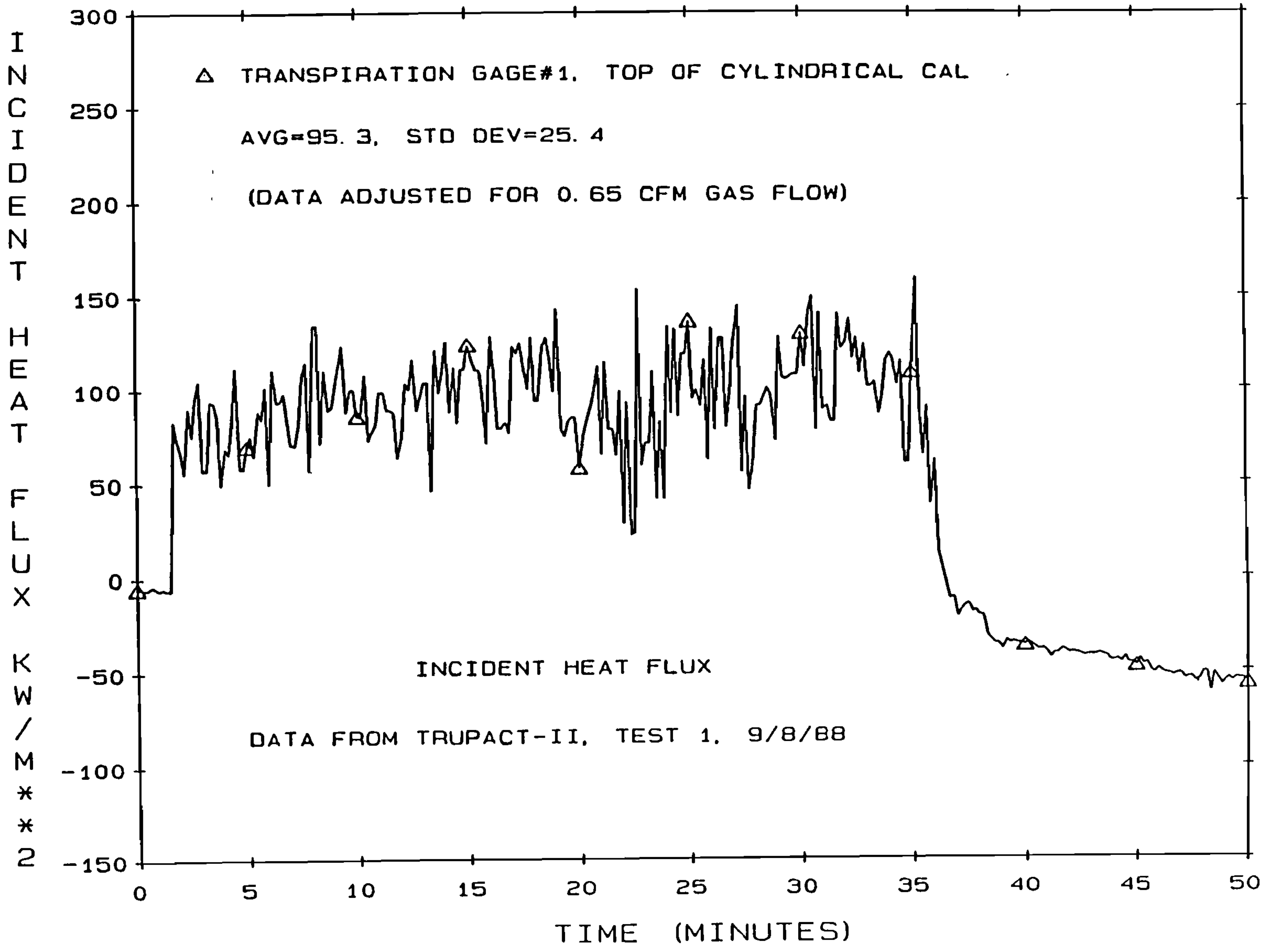

Figure A.8 Incident Heat Flux on the 1.4-m Calorimeter

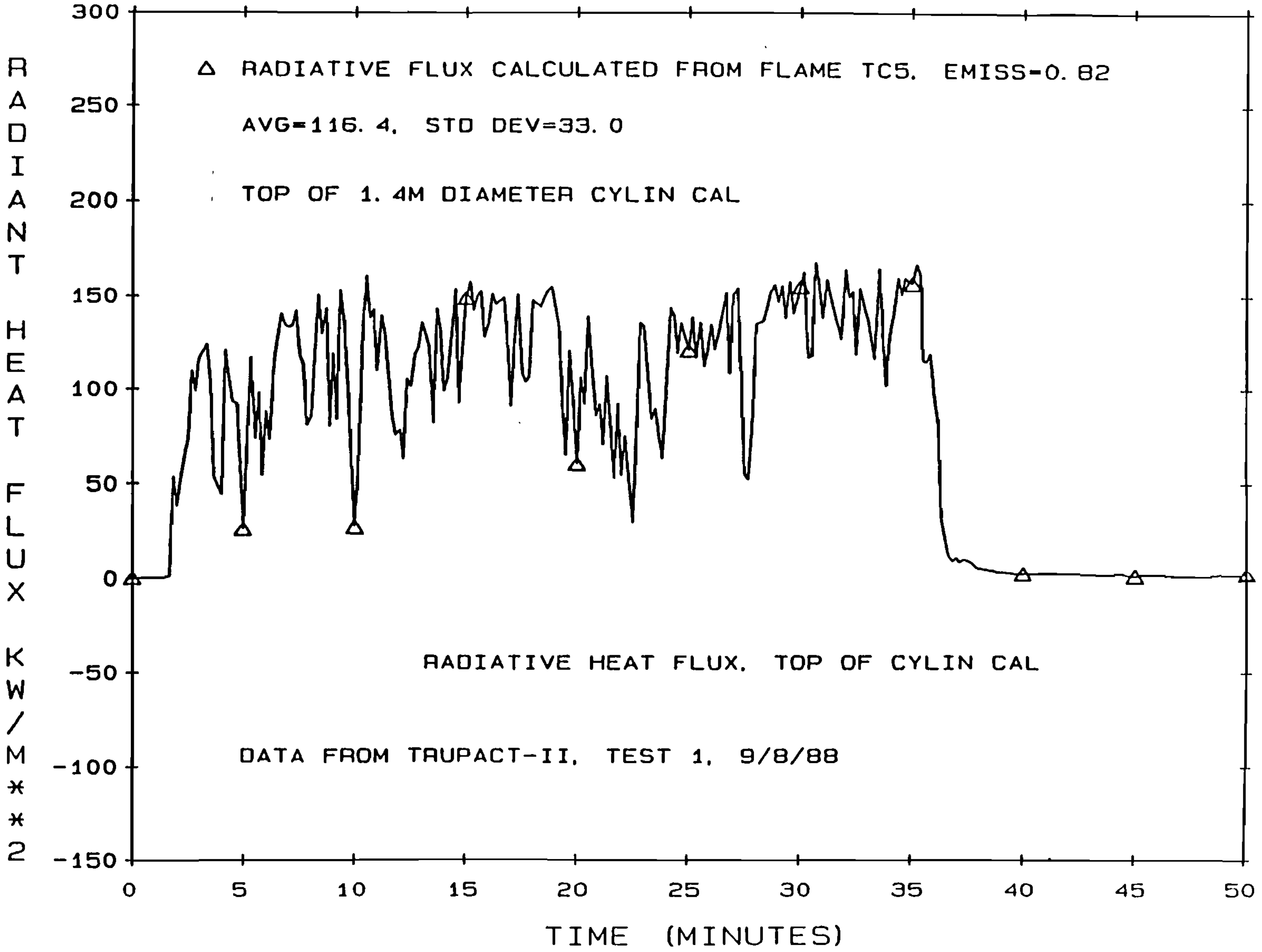

Figure A.9 Radiative Heat Flux for the 1.4-m Calorimeter

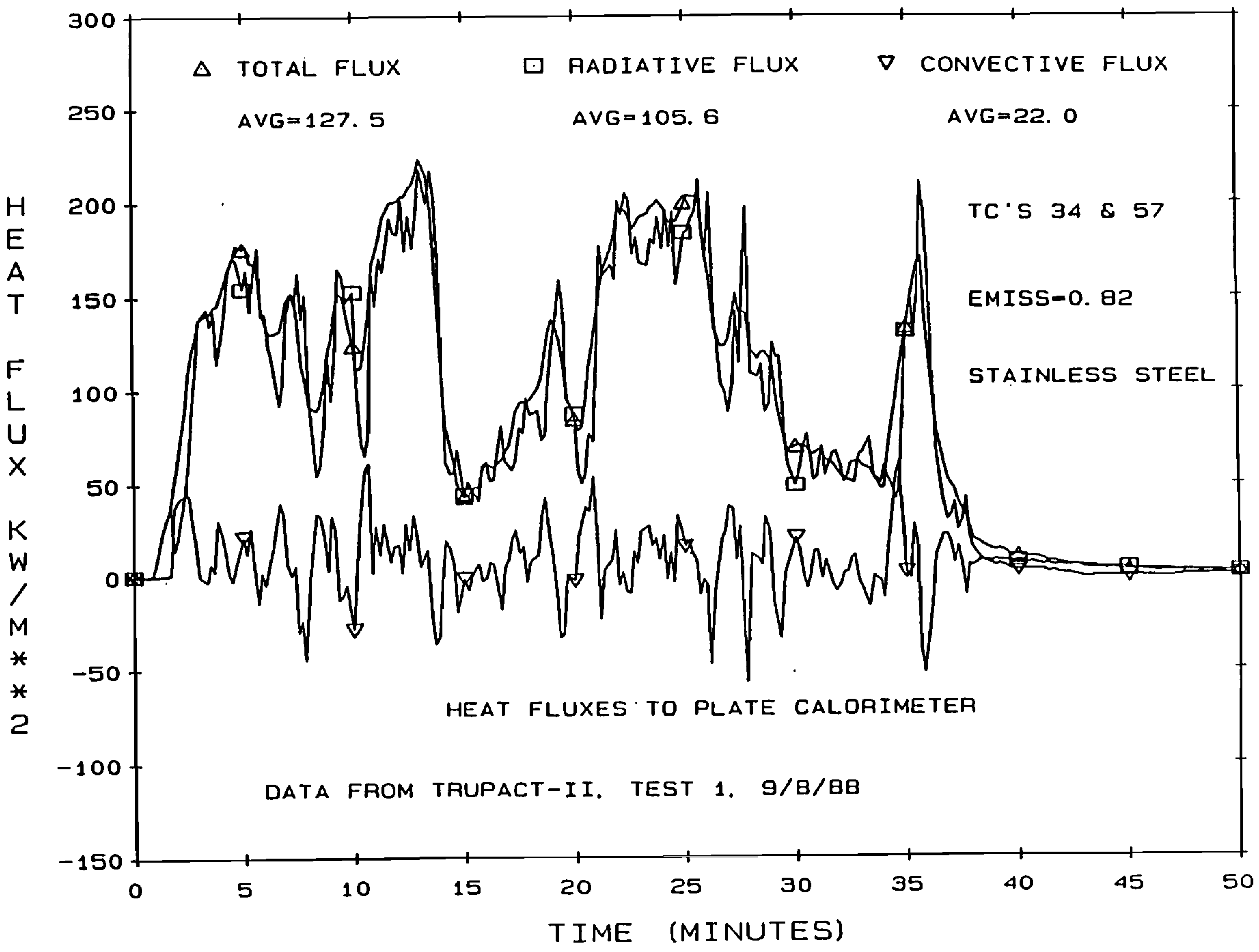

Figure A.10 Heat Fluxes to the Stainless Steel Side of the Plate Calorimeter

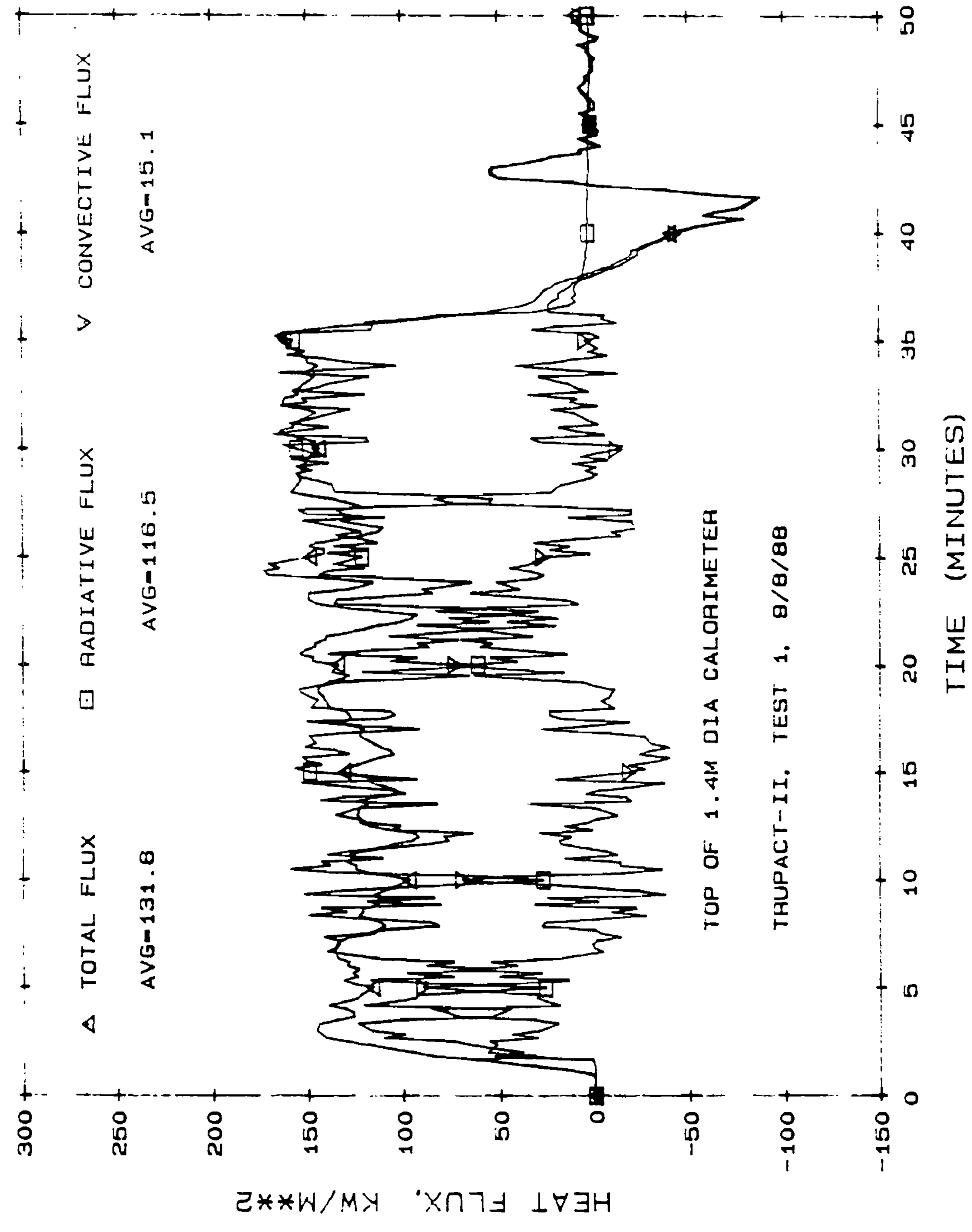

Figure A.11 Heat Fluxes to the 1.4-m Calorimeter

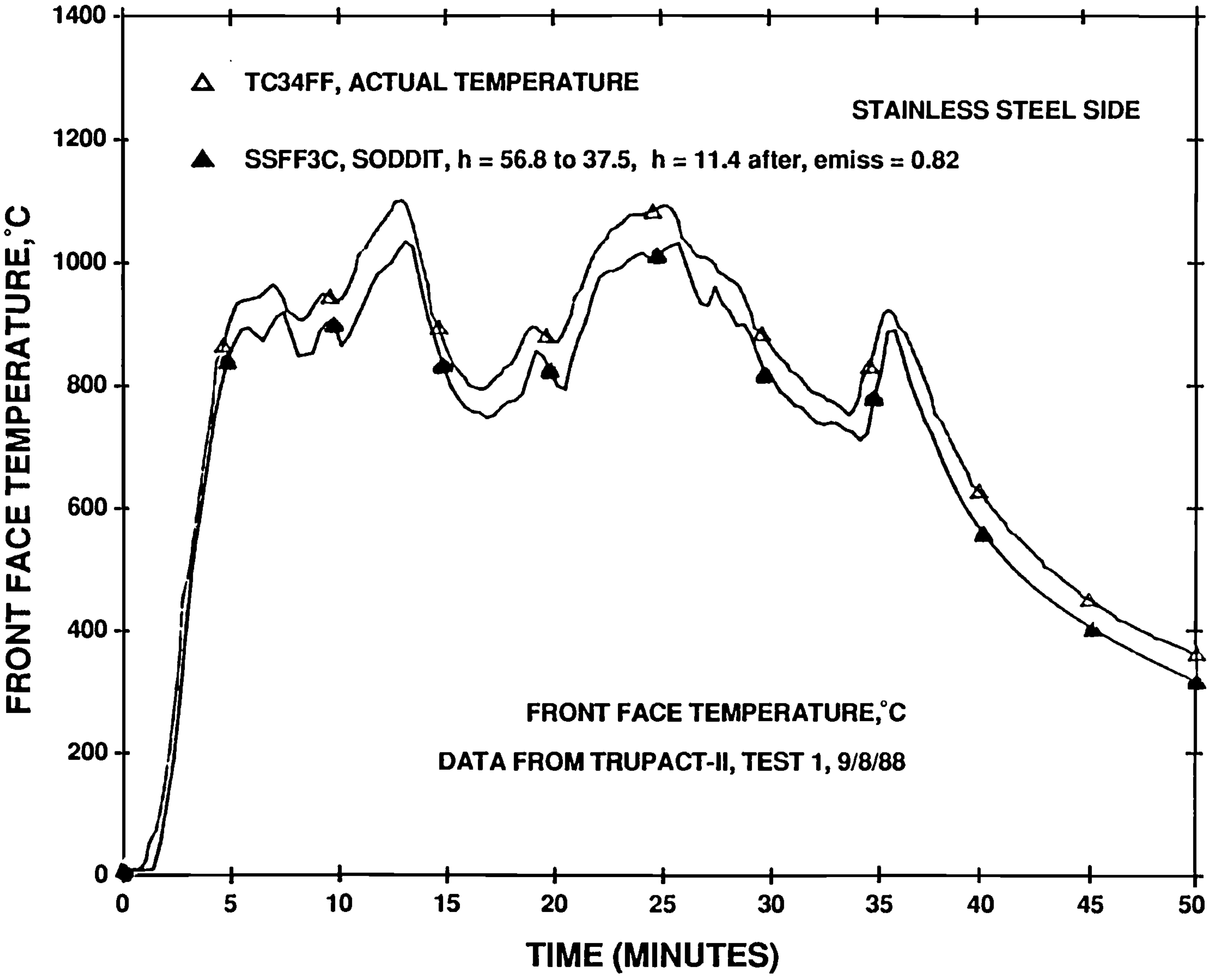

Figure A.12 Front Face Temperature With Two Convection Coefficients—Stainless Steel Side

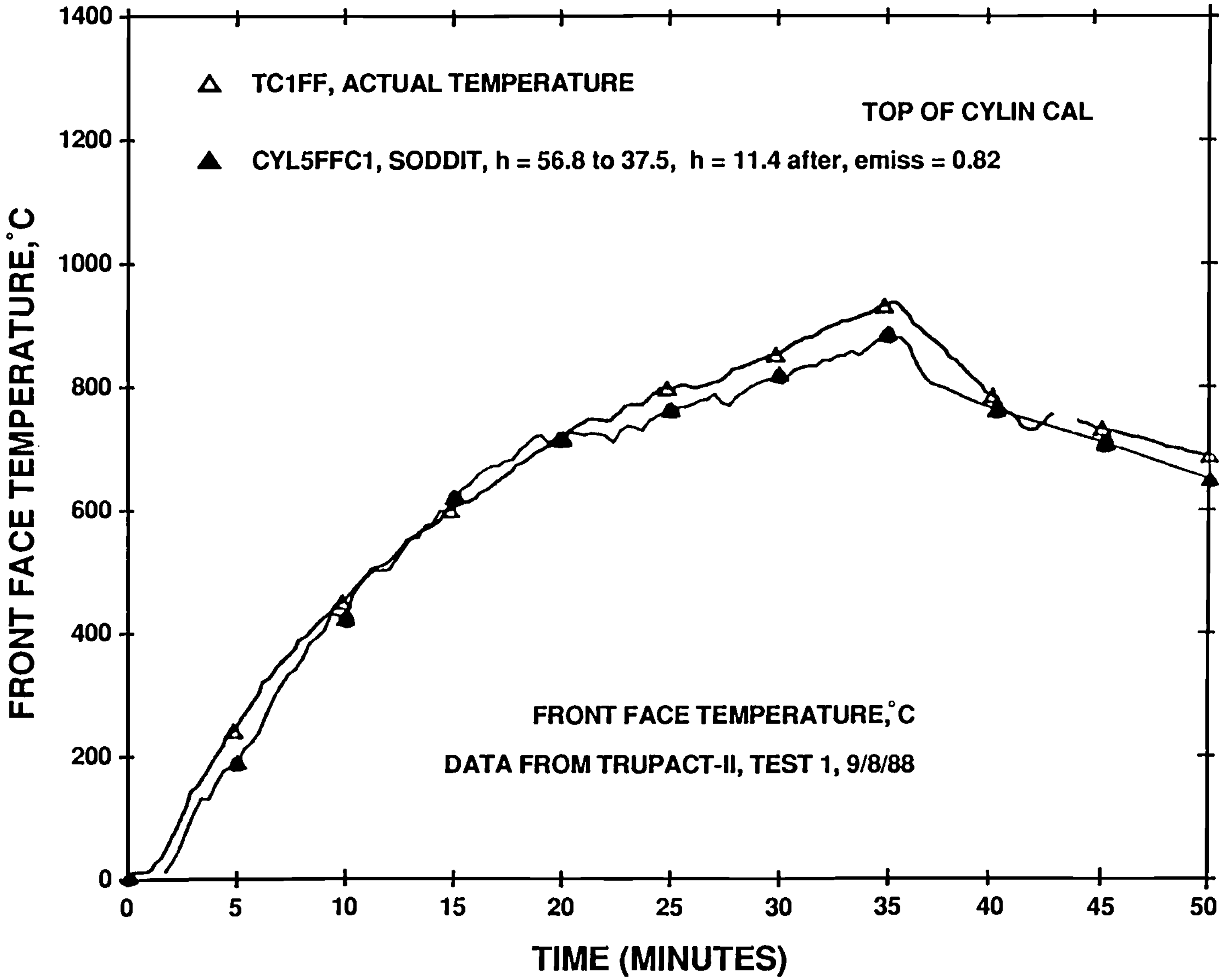

Figure A.13 Front Face Temperature on Top of the 1.4-m Calorimeter With Convection

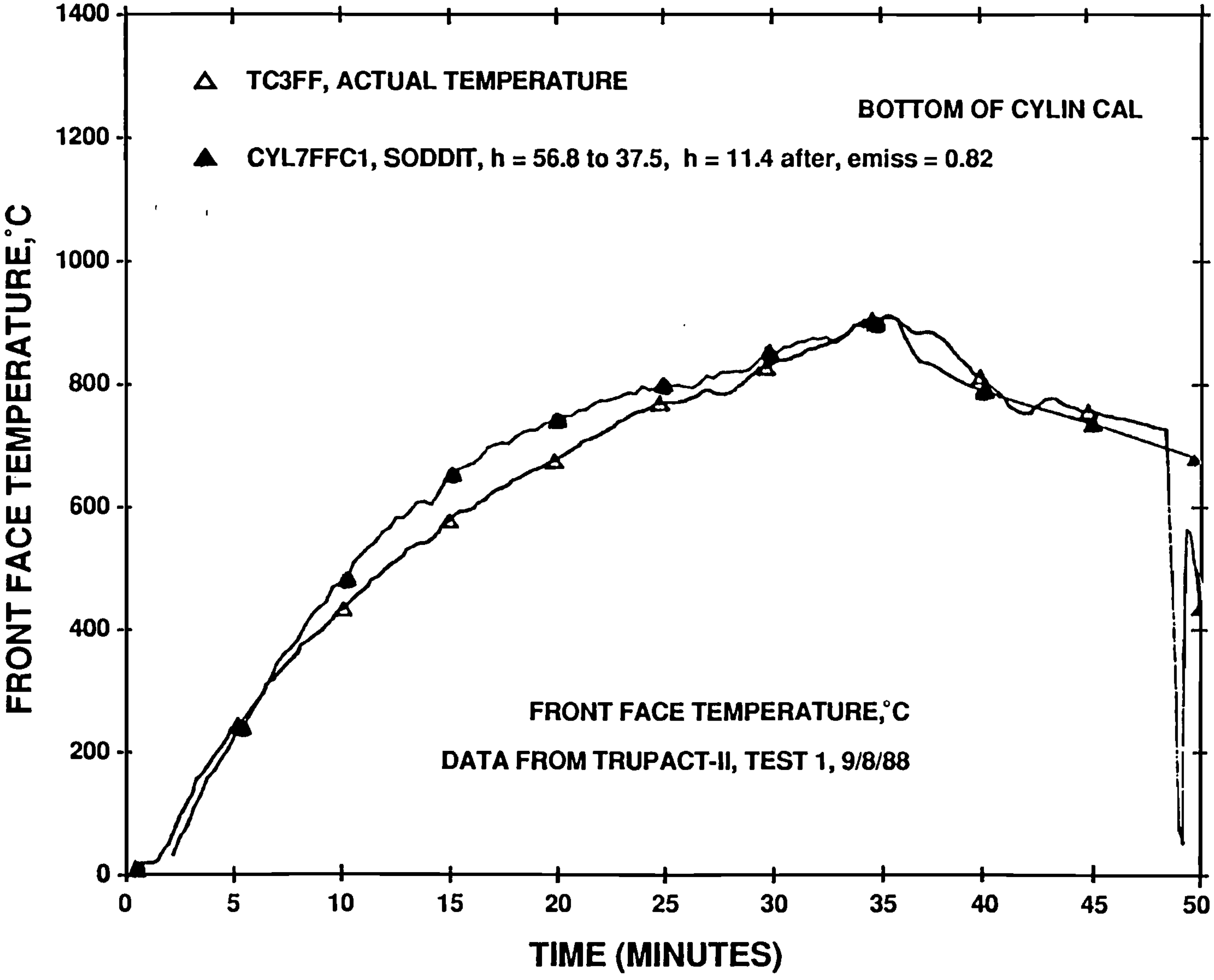

Figure A.14 Front Face Temperatures on Bottom of 1.4-m Calorimeter With Convection

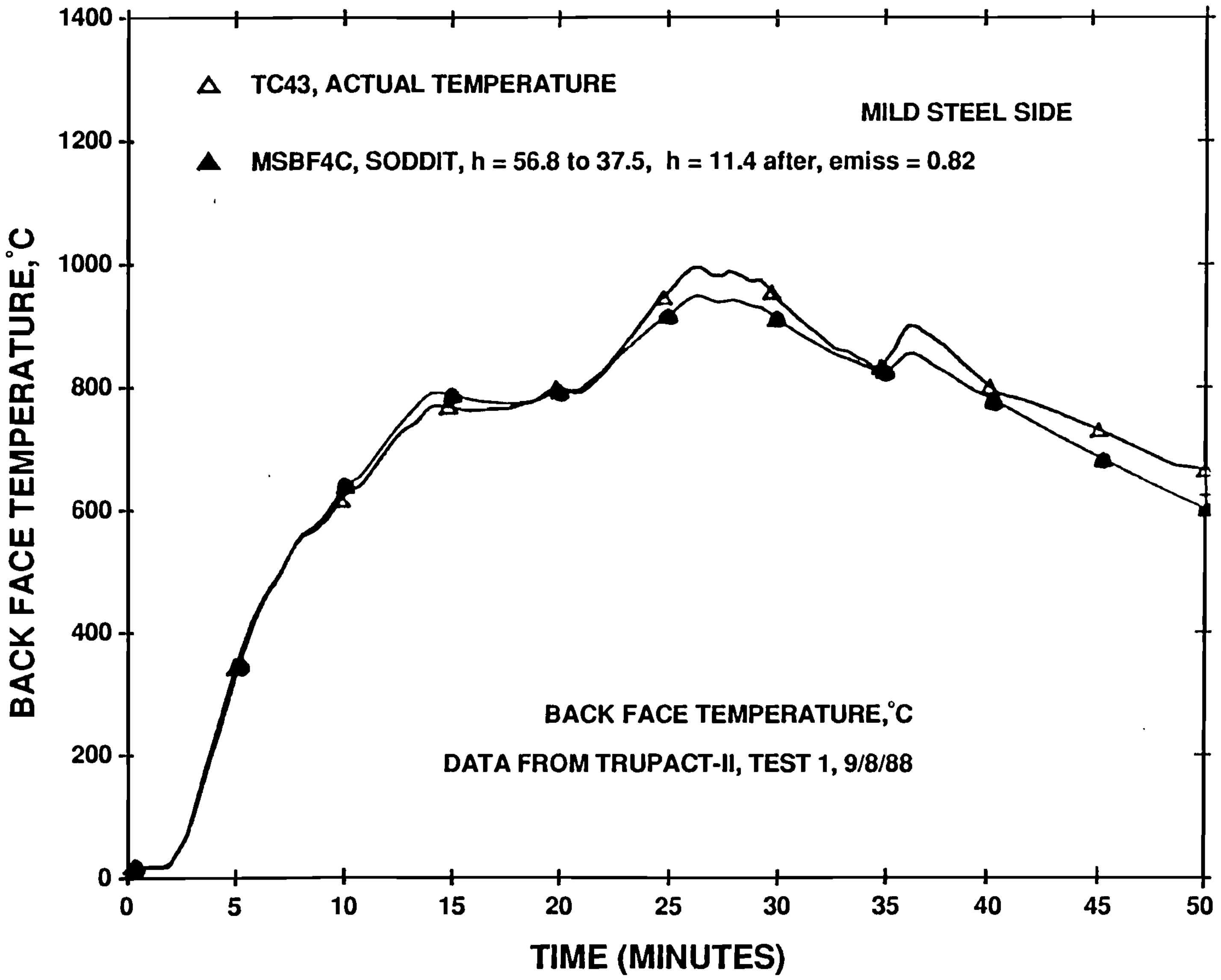

Figure A.15 Back Face Temperature Comparisons on the Mild Steel Side of the Plate Calorimeter

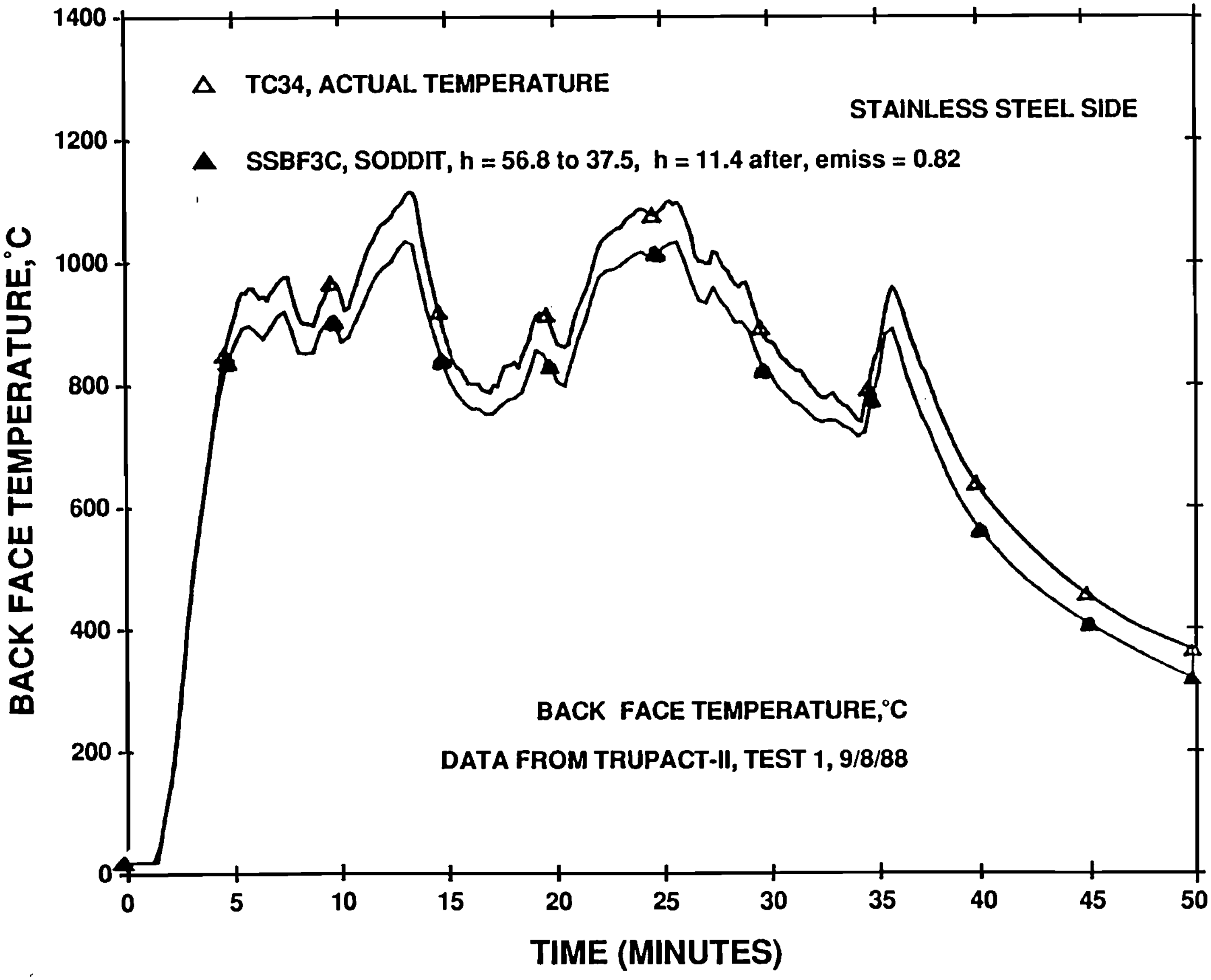

Figure A.16 Back Face Temperature Comparisons on the Stainless Steel Side of the Plate Calorimeter

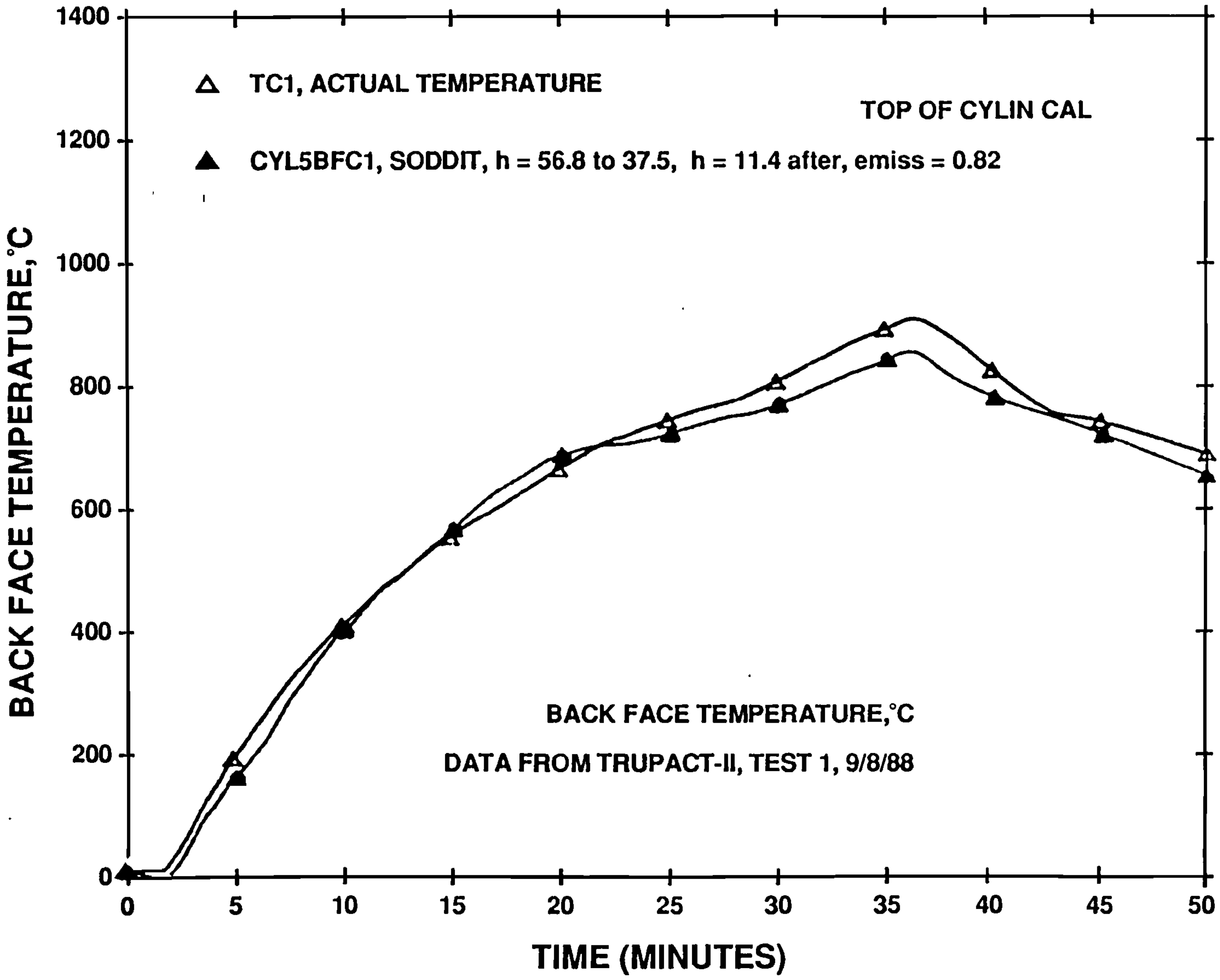

Figure A.17 Back Face Temperature Comparisons on the Top of the 1.4-m Calorimeter

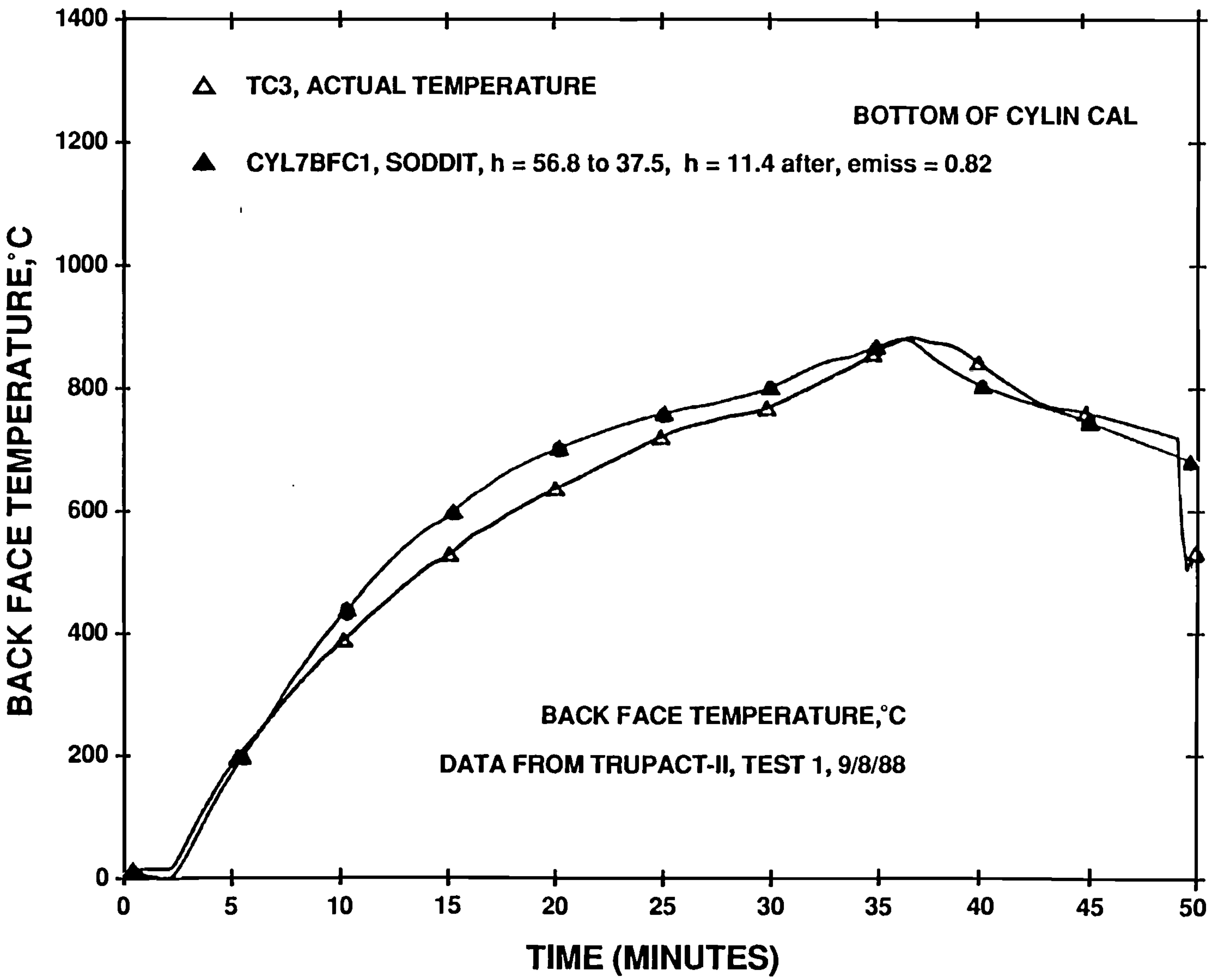

Figure A.18 Back Face Temperature Comparisons on the Bottom of the 1.4-m Calorimeter